

Review

# Recent Progress in Spinel Ferrite (MFe<sub>2</sub>O<sub>4</sub>) Chemiresistive Based Gas Sensors

Run Zhang <sup>1</sup>, Cong Qin <sup>2</sup>, Hari Bala <sup>1</sup>, Yan Wang <sup>3,4,\*</sup> and Jianliang Cao <sup>2,4,\*</sup> 

<sup>1</sup> School of Materials Science and Engineering, Henan Polytechnic University, Jiaozuo 454000, China; zhangrun0518@home.hpu.edu.cn (R.Z.); hari@hpu.edu.cn (H.B.)

<sup>2</sup> College of Chemistry and Chemical Engineering, Henan Polytechnic University, Jiaozuo 454000, China; qincong@hpu.edu.cn

<sup>3</sup> College of Safety Science and Engineering, Henan Polytechnic University, Jiaozuo 454003, China

<sup>4</sup> State Collaborative Innovation Center of Coal Work Safety and Clean-Efficiency Utilization, Henan Polytechnic University, Jiaozuo 454003, China

\* Correspondence: yanwang@hpu.edu.cn (Y.W.); caojianliang@hpu.edu.cn (J.C.)

**Abstract:** Gas-sensing technology has gained significant attention in recent years due to the increasing concern for environmental safety and human health caused by reactive gases. In particular, spinel ferrite (MFe<sub>2</sub>O<sub>4</sub>), a metal oxide semiconductor with a spinel structure, has emerged as a promising material for gas-sensing applications. This review article aims to provide an overview of the latest developments in spinel-ferrite-based gas sensors. It begins by discussing the gas-sensing mechanism of spinel ferrite sensors, which involves the interaction between the target gas molecules and the surface of the sensor material. The unique properties of spinel ferrite, such as its high surface area, tunable bandgap, and excellent stability, contribute to its gas-sensing capabilities. The article then delves into recent advancements in gas sensors based on spinel ferrite, focusing on various aspects such as microstructures, element doping, and heterostructure materials. The microstructure of spinel ferrite can be tailored to enhance the gas-sensing performance by controlling factors such as the grain size, porosity, and surface area. Element doping, such as incorporating transition metal ions, can further enhance the gas-sensing properties by modifying the electronic structure and surface chemistry of the sensor material. Additionally, the integration of spinel ferrite with other semiconductors in heterostructure configurations has shown potential for improving the selectivity and overall sensing performance. Furthermore, the article suggests that the combination of spinel ferrite and semiconductors can enhance the selectivity, stability, and sensing performance of gas sensors at room or low temperatures. This is particularly important for practical applications where real-time and accurate gas detection is crucial. In conclusion, this review highlights the potential of spinel-ferrite-based gas sensors and provides insights into the latest advancements in this field. The combination of spinel ferrite with other materials and the optimization of sensor parameters offer opportunities for the development of highly efficient and reliable gas-sensing devices for early detection and warning systems.

**Keywords:** spinel ferrite; metal oxide semiconductor; chemiresistive gas sensor; nanostructure; doping; heterostructure



**Citation:** Zhang, R.; Qin, C.; Bala, H.; Wang, Y.; Cao, J. Recent Progress in Spinel Ferrite (MFe<sub>2</sub>O<sub>4</sub>) Chemiresistive Based Gas Sensors. *Nanomaterials* **2023**, *13*, 2188. <https://doi.org/10.3390/nano13152188>

Academic Editor: Sergei A. Kulnich

Received: 28 June 2023

Revised: 17 July 2023

Accepted: 25 July 2023

Published: 27 July 2023



**Copyright:** © 2023 by the authors. Licensee MDPI, Basel, Switzerland. This article is an open access article distributed under the terms and conditions of the Creative Commons Attribution (CC BY) license (<https://creativecommons.org/licenses/by/4.0/>).

## 1. Introduction

Metal oxide semiconductor (MOS) gas sensors operate by detecting alterations in the electrical conductivity of a semiconducting metal oxide when exposed to a gas [1]. When the MOS sensor comes into contact with the target gas, the gas molecules adhere to the sensor material's surface, resulting in a modification of the sensor's electrical resistance [2]. The extent and direction of the resistance alteration correlate with the gas concentration and its chemical properties. Numerous metal oxide semiconducting materials, such as tin oxide (SnO<sub>2</sub>) [3], zinc oxide (ZnO) [4], titanium dioxide (TiO<sub>2</sub>) [5], and tungsten oxide (WO<sub>3</sub>) [6],

have been widely utilized in the production of MOS sensors. These materials exhibit diverse sensing characteristics towards various gases, and their sensitivity, selectivity, and stability can be adjusted via material doping, surface modification, and operating conditions. To enhance the performance of MOS gas sensors, novel sensing structures such as nanowires [7], nanotubes [8], and nanostructured thin films [9] have been developed, offering larger surface-to-volume ratios and improved gas adsorption capabilities. Additionally, advanced fabrication techniques such as atomic layer deposition (ALD) [10], chemical vapor deposition (CVD) [11], and spray pyrolysis [12] have been employed to achieve precise control over the sensor's morphology, composition, and functionality. In conclusion, MOS gas sensors have become indispensable tools for monitoring environmental pollution, ensuring industrial safety, and safeguarding public health [13,14]. The ongoing progress in sensor technology and its integration with information and communication systems will create novel opportunities for real-time, reliable, and intelligent gas-sensing solutions.

MOS-gas-sensitive materials can be classified into two categories based on the number of metal ions present in the single-phase metal oxide material: single metal oxides and composite metal oxides. The gas sensors based on single metal oxides exhibit excellent attributes, including easy integration, good repeatability, and effective detection of various gases [15–17]. Nonetheless, there is still room for improvement in terms of the selectivity and recovery performance of single-phase gas-sensitive materials. Researchers have explored strategies to enhance the sensing performance by incorporating precious metal catalysts or combining them with other materials to modify the morphology of single metal oxides, aiming to provide activation energy for reactions or form p–n heterojunctions.

In recent times, the distinctive magnetic properties [18], electrical properties [19], microwave absorption [20], and photocatalytic properties [21] of composite metal oxides, specifically spinel ferrites, have garnered significant attention. The primary preparation techniques for  $MFe_2O_4$ -based gas-sensitive materials include the co-precipitation method [22–25], sol–gel method [26–28], and template synthesis method [29]. These methods enable the production of spinel ferrite nanomaterials with diverse morphologies such as nanorods, nanotubes, nanofilms, and core–shell microspheres. The combination of novel synthesis approaches and the integration of new functional materials has led to the development of spinel ferrite and spinel ferrite composite materials with controllable structures and morphologies, thereby expanding their application potential. For instance, the controlled synthesis of spinel ferrite nanoparticles has exhibited promising outcomes in biomedical applications such as drug delivery and cancer therapy [30]. Furthermore, the combination of spinel ferrite with graphene oxide enhances its magnetic and electrical properties, positioning it as a potential candidate for spintronics [31] and electromagnetic shielding applications [32]. Additionally, the incorporation of metal ions or other functional materials into spinel ferrite has shown improved catalytic and photocatalytic properties, thereby finding application in areas such as wastewater treatment [33] and hydrogen production [34]. Overall, the advancement of novel synthesis methods and the integration of functional materials have broadened the scope of zinc ferrite materials and opened up avenues for future research.

As a semiconducting, magnetic oxide material, spinel ferrite has excellent chemical stability, enabling the effective adsorption of various gases [35]. Its inherent catalytic properties stimulate chemisorption processes that result in changes in its electrical resistance when exposed to different gases [36]. This allows for accurate gas detection and measurement. Additionally, spinel ferrite can operate at lower temperatures compared with other gas sensors, which leads to increased energy efficiency [37]. Its high sensitivity [38] and selectivity [39] towards particular gases, coupled with its capacity for miniaturization, make spinel ferrite an optimal material for building reliable, efficient, and compact gas sensors.

This review article is organized as follows: Section 2 presents an introduction to the gas-sensing mechanism of spinel ferrite. Sections 3–5 present a detailed review of the recent advancements in spinel-ferrite-based gas-sensing materials for the detection of reducing

gases, categorized based on the types of gas-sensing enhancement mechanisms. Finally, in Section 6, a summary and outlook for this review are provided, emphasizing the potential future directions for spinel-ferrite-based gas-sensing materials and their applications.

## 2. Gas-Sensing Mechanism

With its spinel crystal structure, spinel ferrite emerges as a promising sensing material possessing exceptional properties. Figure 1 illustrates the crystal structure of zinc ferrite, where the face-centered cube of  $O^{2-}$  accumulates within its crystal lattice, while the metal ions  $M^{2+}$  and  $Fe^{3+}$  are embedded in the tetrahedral and octahedral gaps formed by  $O^{2-}$ . This structure readily facilitates the formation of defects, including oxygen vacancies, both internally and on the surface, making it highly advantageous for gas-sensitive materials. The unique crystal structure, specifically the insertion of the transition metal cation  $Zn^{2+}$  into the  $Fe^{2+}Fe^{3+}O_4$  structure, plays a crucial role in the effective detection of reducing gases.

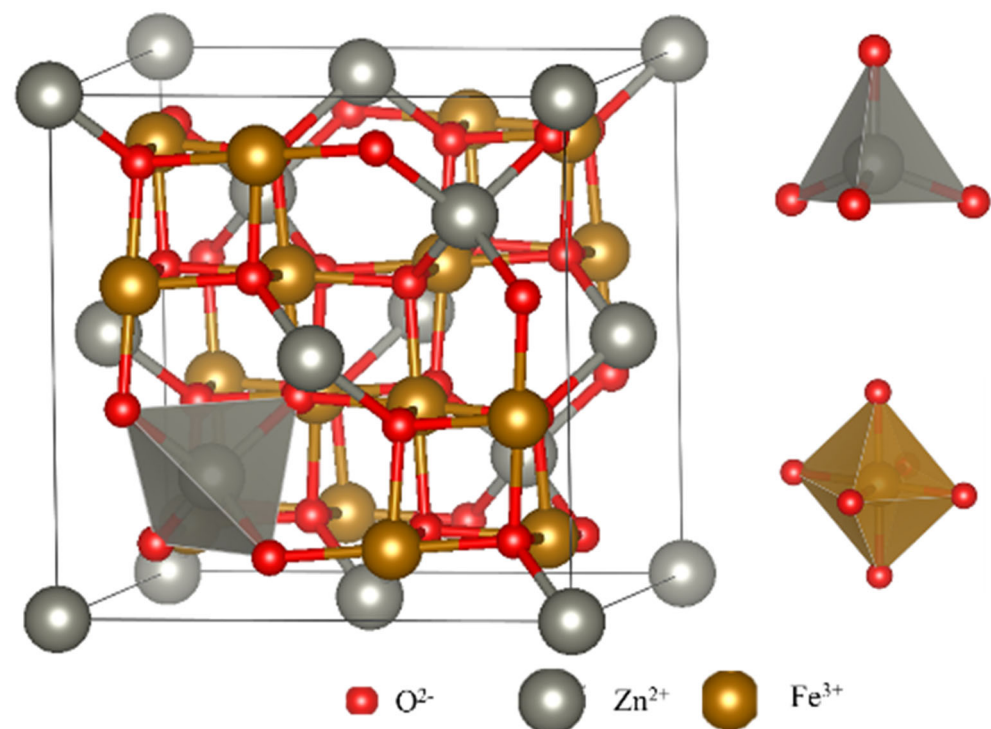
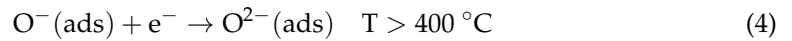
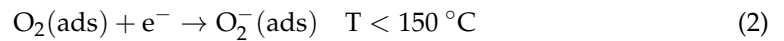


**Figure 1.** The crystal structure of  $ZnFe_2O_4$ , with  $Zn^{2+}$  in the tetrahedron gap and  $Fe^{3+}$  in the octahedron gap.

The gas-sensing response of spinel ferrite is determined by the complex interaction that occurs at the interface between the gas and solid material. However, a unified definition of gas sensor mechanisms is lacking. A commonly proposed sensing mechanism for spinel ferrite sensors is as follows: when a spinel-ferrite-based sensor is exposed to air, oxygen molecules adsorb onto its surface, capturing free electrons from the conduction band and forming oxygen anions. The specific form of these oxygen anions depends on the operating temperature. The loss of electrons generates an electron depletion layer (n-type) on the semiconductor surface, resulting in an increase in resistance. In a reducing gas atmosphere, Equation (6) occurs, leading to a reduction in the resistance of the electron depletion region and sensor. It is worth noting that the reaction described in Equation (6) may vary depending on the operating temperature or target gas.





The unique microstructure and high specific surface area of pure  $\text{MFe}_2\text{O}_4$  nanomaterials offer numerous adsorption sites, leading to an enhancement in gas-sensing performance. The addition of metal ions through doping reduces the barrier height of grain boundaries, facilitating improved carrier diffusion and transfer rates; heterostructures [40], on the other hand, allow for the modulation of the electron depletion region and potential barrier at the interface by leveraging the interaction between Fermi energy levels and energy bands [41]. These mechanisms collectively contribute to the enhancement of gas sensitivity in the respective materials. More detailed explanations of the gas-sensitive mechanisms specific to these new materials can be found in Section 3 (Nanostructures), Section 4 (Doping), and Section 5 (Heterostructures).

### 3. Nanostructure

The gas-sensing application has significantly benefited from the use of nanostructured materials, primarily due to their high surface-to-volume ratio, which allows for better interaction with the gas molecules. In particular, zinc ferrite, a type of spinel ferrite, has been widely used due to its specific surface area, contact area, porosity, grain size, and grain stacking order. These factors all contribute to its gas-sensing properties. The operating temperature, humidity, and gas concentration are several external factors that can influence the performance of zinc ferrite-based gas sensors. For instance, at higher operating temperatures, the sensor's sensitivity can increase due to the enhanced surface reaction rates [42]. On the other hand, excessive humidity may cause the surface of the sensor to become water-saturated, which could inhibit its response to target gases [35]. Apart from these external factors, the morphology-related characteristics of spinel ferrite also play a significant role in its gas-sensing properties. The development of unique morphologies and structures in spinel ferrite is considered a promising approach to enhance its gas-sensing performance. For example, porous spinel ferrite with large specific surface areas can provide more active sites for gas molecule adsorption, facilitating improved surface effects, electronic transfer efficiency, and ultimately a better gas-sensing performance. Various synthesis methods can be employed to create spinel ferrite materials with different morphologies. These include sol-gel, hydrothermal, and co-precipitation methods, among others. Each method offers unique advantages in terms of controlling the size, shape, and distribution of the nanoparticles, thereby allowing for the optimization of the sensor's performance. In the subsequent sections, we will delve deeper into these topics, providing a comprehensive review of the latest research findings on ferrite sensors with diverse nanostructures. We will also discuss the special properties of these sensors as documented in existing literature (Tables 1–4). We believe that this review will provide valuable insights into the ongoing advancements in the field of spinel-ferrite-based gas sensors and highlight potential avenues for future research.

**Table 1.** Summary of the reported spinel ferrite nanoparticles-based gas sensors.

Materials	Synthesis	Morphology	Gas	O.T. (°C)	Conc. (ppm)	Response	$t_{res}/t_{rec}$	LOD	Refs.
CdFe <sub>2</sub> O <sub>4</sub>	Co-precipitating	Nanoparticles	Ethanol	300	1000	48 a	-	-	[43]
CdFe <sub>2</sub> O <sub>4</sub>	Co-precipitating	Nanoparticles	CH <sub>3</sub> SH	300	0.01	2 a	600 s/-	-	[44]
CoFe <sub>2</sub> O <sub>4</sub>	Citrate process	Nanoparticles	H <sub>2</sub> S	225	-	0.6 c	-	-	[45]
CoFe <sub>2</sub> O <sub>4</sub>	Hydrothermal	Nanoparticles	TEA	190	50	4.5 a	100 s/120 s	-	[46]
CoFe <sub>2</sub> O <sub>4</sub>	Hydrothermal	Nanoparticles	Ethanol	150	50	6 a	50 s/60 s	-	[46]
CoFe <sub>2</sub> O <sub>4</sub>	Co-precipitation	Nanoparticles (12 nm)	LPG	RT	5 vol.%	2700 c	30 s/60 s	-	[22]
CoFe <sub>2</sub> O <sub>4</sub>	Sol-gel auto-combustion	Nanoparticles	NH <sub>3</sub>	RT	100	0.7 c	118 s/145 s	-	[47]
CoFe <sub>2</sub> O <sub>4</sub>	Sol-gel method	Nanoparticles (~50 nm)	Ethanol	300	150	0.72 c	75 s/110 s	-	[48]
CoFe <sub>2</sub> O <sub>4</sub>	Microwave-assisted	Nanoparticles	SO <sub>2</sub>	120	3.5	3.50 d	10 s/20 s	250 ppb	[49]
CoFe <sub>2</sub> O <sub>4</sub>	Hydrothermal	Nanoparticles	Ethanol	200	100	110 a	15 s/18 s	-	[35]
CoFe <sub>2</sub> O <sub>4</sub>	Solution phase reaction	hexagonally nanoparticle	CO	400	100	3 a	-	-	[50]
CoFe <sub>2</sub> O <sub>4</sub>	Spray pyrolysis	Nanoparticles (54 nm)	LPG	250	5	0.2 c	-	-	[51]
CoFe <sub>2</sub> O <sub>4</sub>	Uniaxial press	Nanoparticles (5.8 nm)	LPG	250	200	0.72 c	3.8 s/43.2 s	-	[52]
CoFe <sub>2</sub> O <sub>4</sub>	Solvothermal	Nanoparticles (10 nm)	Acetone	220	100	17.3 a	27 s/7 s	-	[53]
CoFe <sub>2</sub> O <sub>4</sub>	Hydrothermal	Nanoparticles	CH <sub>3</sub> OH	90	100	0.42 c	-	-	[54]
CoFe <sub>2</sub> O <sub>4</sub>	Hydrothermal	Porous nanoparticles	CH <sub>3</sub> OH	RT	100	0.20 c	-	-	[54]
CuFe <sub>2</sub> O <sub>4</sub>	Citrate process	Nanoparticles	CO	200	-	0.4 c	-	-	[45]
CuFe <sub>2</sub> O <sub>4</sub>	Solid-state reaction	Nanoparticles (70–150 nm)	Ethanol	332	1000	7.5 a	10 s/15 s	-	[55]
CuFe <sub>2</sub> O <sub>4</sub>	Sol-gel	Nanoparticles	LPG	300	150	0.45 c	180 s/240 s	-	[56]
CuFe <sub>2</sub> O <sub>4</sub>	Co-precipitation	Nanoparticles	LPG	RT	1 vol.%	2.6 c	30 s/200 s	-	[57]
CuFe <sub>2</sub> O <sub>4</sub>	Sol-gel technique	Nanoparticles (35.8 ± 5.3 nm)	H <sub>2</sub> S	80	25	0.15 c	51.5 s/-	-	[58]
CuFe <sub>2</sub> O <sub>4</sub>	Co-precipitation	Nanoparticle (7 ± 2.1 nm)	H <sub>2</sub> S	80	300	0.39 d	21.9 s/-	-	[25]
CuFe <sub>2</sub> O <sub>4</sub>	Sputtering	Nanoparticles	H <sub>2</sub>	50	1 vol.%	0.15 c	48 ± 11 s/-	-	[59]
CuFe <sub>2</sub> O <sub>4</sub>	Co-precipitation and annealed	Nanoparticles (22 ± 3 nm)	H <sub>2</sub> S	140	300	0.3 d	32 ± 10 s/-	-	[60]
CuFe <sub>2</sub> O <sub>4</sub>	Co-precipitation	Nanoparticles (6.4 nm)	NH <sub>3</sub>	RT	20	0.6 c	8 s/300 s	-	[37]
MgFe <sub>2</sub> O <sub>4</sub>	Solid-state reaction	Nanoparticles	H <sub>2</sub> S	160	2	13 b	-	-	[61]
MgFe <sub>2</sub> O <sub>4</sub>	Solid-state reaction	Nanoparticles (15–30 nm)	Ethanol	350	50	13 b	-	-	[61]
MgFe <sub>2</sub> O <sub>4</sub>	Co-precipitation method	Particle (1 μm)	LPG	250	3	3 a	-	-	[62]
MgFe <sub>2</sub> O <sub>4</sub>	Wet chemical	Nanoparticles (84 nm)	H <sub>2</sub>	315	1000	0.53 c	-	-	[63]
MgFe <sub>2</sub> O <sub>4</sub>	Wet chemical	Nanoparticles	H <sub>2</sub>	250	1660	1.02 c	-	-	[64]
MgFe <sub>2</sub> O <sub>4</sub>	Sol-gel	Nanoparticles (38 nm)	LPG	325	2000	0.71 c	-	-	[65]
MgFe <sub>2</sub> O <sub>4</sub>	Citrate gel combustion	Nanoparticles (37 nm)	LPG	400	100	0.22 c	34 s/67 s	-	[66]
MgFe <sub>2</sub> O <sub>4</sub>	Auto-combustion	Spherical particles (15–20 nm)	Ethanol	275	5	0.73 c	-	-	[67]

Table 1. Cont.

Materials	Synthesis	Morphology	Gas	O.T. (°C)	Conc. (ppm)	Response	$t_{res}/t_{rec}$	LOD	Refs.
MgFe <sub>2</sub> O <sub>4</sub>	Spray pyrolysis	Nanoparticles (25–45 nm)	Acetone	323 k	75	193% c	-	-	[68]
MgFe <sub>2</sub> O <sub>4</sub>	Co-precipitation	0.9 ± 0.2 μm	CO <sub>2</sub>	300	5000	0.36 c	120 s/240 s	-	[69]
MgFe <sub>2</sub> O <sub>4</sub>	Sol-gel combustion	0.18 ± 0.06 μm	CO <sub>2</sub>	300	5000	0.24 c	300 s/300 s	-	[69]
MgFe <sub>2</sub> O <sub>4</sub>	Sol-gel synthesis	Nanoparticles	LPG	RT	4 vol%	27.9% c	158 s/152 s	-	[70]
MgFe <sub>2</sub> O <sub>4</sub>	Polymerization method	Nanoparticles (120 nm)	NO <sub>2</sub>	300	10	39.5 a	-	-	[71]
MgFe <sub>2</sub> O <sub>4</sub>	Reverse coprecipitation	Nanoparticles (132 nm)	NO <sub>2</sub>	300	10	15 a	-	-	[71]
MgFe <sub>2</sub> O <sub>4</sub>	Auto-combustion	Nanoparticles (41 nm)	LPG	250	5	0.3 c	-	-	[72]
NiFe <sub>2</sub> O <sub>4</sub>	Citrate process	Nanoparticles	Cl <sub>2</sub>	300	-	0.75 c	-	-	[45]
NiFe <sub>2</sub> O <sub>4</sub>	Reverse micelle	Nanoparticles	LPG	380	100	0.18 c	-	-	[73]
NiFe <sub>2</sub> O <sub>4</sub>	Hydrothermal	Nanoparticles	LPG	200	100	0.4 c	-	-	[73]
NiFe <sub>2</sub> O <sub>4</sub>	Pulsed wire discharge	Nanoparticles (18–45 nm)	Cl <sub>2</sub>	350	500	0.39 c	-	-	[74]
NiFe <sub>2</sub> O <sub>4</sub>	Ion beam sputtering	Nanoparticles (35 nm)	CH <sub>4</sub>	130	20,000	1.12 a	-	-	[75]
NiFe <sub>2</sub> O <sub>4</sub>	Sol-gel auto combustion	Nanoparticles	Acetone	275	500	4.65 c	170 s/600 s	-	[76]
NiFe <sub>2</sub> O <sub>4</sub>	Glycine combustion	Nanoparticles (38 nm)	LPG	350	2000	375% a	40 s/140 s	-	[77]
NiFe <sub>2</sub> O <sub>4</sub>	Sol-gel self-combustion	Nanoparticles (5.35 nm)	H <sub>2</sub> S	150	200	0.75 c	60 s/300 s	-	[78]
NiFe <sub>2</sub> O <sub>4</sub>	Sol-gel method	Nanoparticles (23 nm)	LPG	RT	2000	2.1 a	72 s/183 s	-	[79]
NiFe <sub>2</sub> O <sub>4</sub>	Sol-gel method	Nanoparticles (23 nm)	CO <sub>2</sub>	RT	2000	1.3 b	100 s/400 s	-	[79]
NiFe <sub>2</sub> O <sub>4</sub>	Co-precipitation	Nanoparticles (15 nm)	LPG	RT	4 vol.%	62.3 b	200 s/250 s	-	[23]
NiFe <sub>2</sub> O <sub>4</sub>	Auto-combustion	Nanoparticles (17 nm)	NH <sub>3</sub>	400	250	23% c	100 s/119 s	-	[80]
NiFe <sub>2</sub> O <sub>4</sub>	Ligand-assisted self-assembly	Nanoparticles (20–40 nm)	Acetone	210	200	57 a	44 s/24 s	-	[81]
NiFe <sub>2</sub> O <sub>4</sub>	Combustion	Nanoparticles (16 nm)	LPG	300	3000	35.62% c	-	-	[82]
NiFe <sub>2</sub> O <sub>4</sub>	Auto-combustion	Nanoparticles	NH <sub>3</sub>	410K	1000	65.29% c	-	-	[83]
NiFe <sub>2</sub> O <sub>4</sub>	Hydrothermal	Nanoparticles	Acetone	190	100	120% c	70 s/130 s	-	[84]
ZnFe <sub>2</sub> O <sub>4</sub>	Citrate process	Nanoparticles	H <sub>2</sub> S	200	-	0.65 c	-	-	[45]
ZnFe <sub>2</sub> O <sub>4</sub>	W/O microemulsion	Nanoparticles	Cl <sub>2</sub>	270	50	83.6 a	4 s/30 s	-	[85]
ZnFe <sub>2</sub> O <sub>4</sub>	Hydrothermal	Nanoparticles	Ethanol	180	100	76 a	-	-	[86]
ZnFe <sub>2</sub> O <sub>4</sub>	W/O microemulsion	Spherical particles (30 nm)	Cl <sub>2</sub>	270	50	85 a	4 s/30 s	-	[38]
ZnFe <sub>2</sub> O <sub>4</sub>	Solid-state reaction	Nanoparticles (15–20 nm)	H <sub>2</sub> S	250	200	3.25 a	20 s/90 s	-	[87]
ZnFe <sub>2</sub> O <sub>4</sub>	Co-precipitation	Nanoparticles	Acetone	300	1000	100,000 a	-	-	[88]
ZnFe <sub>2</sub> O <sub>4</sub>	Wet chemical	Nanoparticles (25–30 nm)	Ethanol	350	100	0.6 c	-	-	[26]
ZnFe <sub>2</sub> O <sub>4</sub>	Glycine combustion	Nanoparticles (25–30 nm)	Acetone	250	2000	57% c	-	-	[89]
ZnFe <sub>2</sub> O <sub>4</sub>	Co-precipitation	Nanoparticles (65 nm)	Ethanol	190	100	0.82 c	30 s/90 s	-	[90]

Table 1. Cont.

Materials	Synthesis	Morphology	Gas	O.T. (°C)	Conc. (ppm)	Response	$t_{res}/t_{rec}$	LOD	Refs.
ZnFe <sub>2</sub> O <sub>4</sub>	Co-precipitation	Nanoparticles (65 nm)	Cl <sub>2</sub>	152	500	0.75 c	20 s/50 s	-	[90]
ZnFe <sub>2</sub> O <sub>4</sub>	Auto combustion	Spherical particles (10 nm)	Ethanol	250	200	1.35 a	70 s/90 s	-	[91]
ZnFe <sub>2</sub> O <sub>4</sub>	Hydrothermal	Nanoparticles (10 nm)	Acetone	200	200	39.5 a	-	-	[92]
ZnFe <sub>2</sub> O <sub>4</sub>	Solid-state	Nanoparticles	HCHO	260	100	37.3 a	4 s/17 s	-	[93]
ZnFe <sub>2</sub> O <sub>4</sub>	Solid-state	Nanoparticles	Ethanol	300	100	29.1 a	2 s/7 s	-	[93]
ZnFe <sub>2</sub> O <sub>4</sub>	Sol-gel self-combustion	Nanoparticles (7 nm)	H <sub>2</sub> S	150	200	0.82 c	40 s/210 s	-	[94]
ZnFe <sub>2</sub> O <sub>4</sub>	Molten salt route	Nanoparticles (27 nm)	H <sub>2</sub> S	260	50	22.5 a	8 s/20 s	-	[95]
ZnFe <sub>2</sub> O <sub>4</sub>	Co-precipitation	Nanoparticles (5 ± 1.4 nm)	H <sub>2</sub> S	80	300	0.64 d	20.1 s/-	-	[25]
ZnFe <sub>2</sub> O <sub>4</sub>	Plasma spraying	Nanoparticles (30 nm)	Acetone	200	100	2.7 a	-	-	[96]
ZnFe <sub>2</sub> O <sub>4</sub>	Plasma spraying	Nanoparticles (30 nm)	Acetone	200	100	2.7 a	-	1.8 ppm	[97]
ZnFe <sub>2</sub> O <sub>4</sub>	Co-precipitation	Nanoparticles (4.8 nm)	Ethanol	300 k	40	37.1a	50 s/116 s	-	[98]
ZnFe <sub>2</sub> O <sub>4</sub>	Hydrothermal	Nanoparticles (10 nm)	NO <sub>2</sub>	125	10	247.7 b	6.5 s/11 s	-	[99]
ZnFe <sub>2</sub> O <sub>4</sub>	Self-catalyzed treatment	Nanoparticles (20 nm)	Acetone	280	100	27.6 a	6 s/4 s	-	[100]
ZnFe <sub>2</sub> O <sub>4</sub>	Ball milling and annealed	Nanoparticles (23.03 nm)	NO <sub>2</sub>	600	300	5% d	145 s/20 s	-	[42]
ZnFe <sub>2</sub> O <sub>4</sub>	Hydrothermal	Nanoparticles (23 nm)	Ethanol	220	40	202.5 a	56 s/46 s	-	[101]
ZnFe <sub>2</sub> O <sub>4</sub>	Hydrothermal	Nanoparticles	O <sub>3</sub>	200	0.03	3.7 a	-	-	[27]
ZnFe <sub>2</sub> O <sub>4</sub>	Solvothermal	Nanoparticles	H <sub>2</sub> S	250	2	498% d	48 s/74 s	-	[102]
ZnFe <sub>2</sub> O <sub>4</sub>	PLD	Nanoparticles (48 nm)	LPG	375	5000	93% c	110 s/180 s	-	[103]
ZnFe <sub>2</sub> O <sub>4</sub>	Sol-gel	Nanoparticles (100 nm)	Ethanol	350	150	0.37 c	120 s/240 s	-	[56]
ZnFe <sub>2</sub> O <sub>4</sub>	Wet chemical	-	H <sub>2</sub>	350	1000	0.47 c	33 s/199 s	-	[104]
ZnFe <sub>2</sub> O <sub>4</sub>	Solid-phase reaction	Nanoparticles	Ethanol	332	100	21.5 a	4 s/14 s	-	[104]
ZnFe <sub>2</sub> O <sub>4</sub>	Solid-phase reaction	Nanoparticles	H <sub>2</sub> S	240	100	14.8 a	7 s/25 s	-	[105]
ZnFe <sub>2</sub> O <sub>4</sub>	Solid-state reaction	Nanoparticles (37.8 nm)	Humidity	-	-	2895 a	-	-	[106]
ZnFe <sub>2</sub> O <sub>4</sub>	Sol-gel auto combustion	Nanoparticles (20 nm)	Ethanol	275	100	4.1 c	10 s/40 s	-	[107]
ZnFe <sub>2</sub> O <sub>4</sub>	Spray pyrolysis	Nanoparticles (61 nm)	LPG	300	5	0.26 c	-	-	[51]
ZnFe <sub>2</sub> O <sub>4</sub>	Screen printing	Nanoparticles (4 nm)	LPG	RT	5 vol.%	16 a	120 s/150 s	-	[108]
ZnFe <sub>2</sub> O <sub>4</sub>	Sol-gel auto-combustion	Nanoparticles	NH <sub>3</sub>	RT	100	0.81 c	381 s/333 s	-	[109]
ZnFe <sub>2</sub> O <sub>4</sub>	Solvothermal	Nanoparticles (21.6 nm)	H <sub>2</sub> S	135	5	15.1 a	30 s/120 s	-	[110]
ZnFe <sub>2</sub> O <sub>4</sub>	MOF and annealing treatment	Porous olive-shaped nanoparticles	Ethanol	120	200	223 a	10 s/184 s	-	[111]

O.T. operating temperature; Conc. concentration;  $t_{res}/t_{rec}$  response time/recovery time; LOD limit of detection. a Response is defined as  $R_a/R_g$ ; b Response is defined as  $R_g/R_a$ ; c Response is defined as  $\Delta R/R_a$ ; d Response is defined as  $\Delta R/R_g$ .  $R_a$ : resistance of the sensor in air;  $R_g$ : resistance of the sensor exposed to target gas;  $\Delta R$ : the change in resistance, which equals  $|R_a - R_g|$ .

**Table 2.** Summary of the reported spinel ferrite nanorods/nanotubes-based gas sensors.

Materials	Synthesis	Morphology	Gas	O.T. (°C)	Conc. (ppm)	Response	$t_{res}/t_{rec}$	LOD	Refs.
CoFe <sub>2</sub> O <sub>4</sub>	Electrospinning	Nanofibers	NH <sub>3</sub>	RT	900	0.42 a	-	25 ppm	[112]
CoFe <sub>2</sub> O <sub>4</sub>	Hydrothermal	Nanorods	CH <sub>3</sub> OH	90	100	13.3% c	-	-	[54]
NiFe <sub>2</sub> O <sub>4</sub>	Hydrothermal	Nanorods	NH <sub>3</sub>	150	100	5 a	-	-	[113]
NiFe <sub>2</sub> O <sub>4</sub>	Solvothermal	Nanorods	LPG	200	200	0.687 c	114/18 s	-	[114]
NiFe <sub>2</sub> O <sub>4</sub>	Annealing treatment	Nanorods	n-propanol	120	100	89.2 a	19/41 s	0.41 ppm	[115]
NiFe <sub>2</sub> O <sub>4</sub>	Hydrothermal	Nanorod	Acetone	310	100	70% c	45/75 s	-	[84]
NiFe <sub>2</sub> O <sub>4</sub>	Hydrothermal	Nanorods	TEA	175	1	7 a	12 s/-	-	[116]
NiFe <sub>2</sub> O <sub>4</sub>	Hydrothermal	Nanorods	Toluene	200	500	59.64 a	-	1 ppm	[117]
ZnFe <sub>2</sub> O <sub>4</sub>	Sol-gel template	Tubes	LPG	300	500	17.56 a	-	-	[118]
ZnFe <sub>2</sub> O <sub>4</sub>	Microemulsion and calcination	Porous nanorods	Ethanol	RT	50	14 a	-	-	[119]
ZnFe <sub>2</sub> O <sub>4</sub>	Sol-gel	Aligned nanorods	LPG	RT	5000	4.35 a	60/220 s	-	[120]
ZnFe <sub>2</sub> O <sub>4</sub>	Sol-gel spin coating	Nanorods	LPG	RT	2000	140% c	-	-	[121]
ZnFe <sub>2</sub> O <sub>4</sub>	Hydrothermal	Nanorods	Acetone	260	100	52.8 a	1 s/11 s	-	[122]
ZnFe <sub>2</sub> O <sub>4</sub>	Electrospinning	Nanofiber	H <sub>2</sub> S	350	1	102 a	-	-	[123]
ZnFe <sub>2</sub> O <sub>4</sub>	Electrospinning	Nanofibers	Acetone	190	1000 $\mu$ L/L	13.5 a	15/17 s	1 $\mu$ L/L	[124]
CuFe <sub>2</sub> O <sub>4</sub>	Co-precipitation	Nanorods	LPG	RT	5 vol.%	0.57 c	150/510 s	-	[125]

a Response is defined as  $R_a/R_g$ ; c Response is defined as  $\Delta R/R_a$ .

**Table 3.** Summary of the reported spinel ferrite nanosheets -based gas sensors.

Materials	Synthesis	Morphology	Gas	O.T. (°C)	Conc. (ppm)	Response	$t_{res}/t_{rec}$	LOD	Refs.
CuFe <sub>2</sub> O <sub>4</sub>	Sol-gel	Porous hierarchical	LPG	RT	5000	96% d	60 s/-	-	[126]
MgFe <sub>2</sub> O <sub>4</sub>	Sol-gel	Thick films	acetone	725 K	1000	80% c	13/6 s	-	[127]
ZnFe <sub>2</sub> O <sub>4</sub>	Spray pyrolysis	Thin film	ethanol	390	5	1.2 c	40/120 s	1 ppm	[128]
ZnFe <sub>2</sub> O <sub>4</sub>	hydrothermal	Porous nanosheets	H <sub>2</sub> S	85	5	123 a	39/34 s	0.5 ppm	[129]
ZnFe <sub>2</sub> O <sub>4</sub>	Sol gel	Thin films	LPG	375	900,000	79% c	110/180 s	-	[103]
ZnFe <sub>2</sub> O <sub>4</sub>	Spray pyrolysis	Thick films	SO <sub>2</sub>	150	100	25% c	-	-	[130]

a Response is defined as  $R_a/R_g$ ; c Response is defined as  $\Delta R/R_a$ ; d Response is defined as  $\Delta R/R_g$ .

### 3.1. Nanoparticles

The preparation method for spinel ferrite nanoparticles can be achieved through the following steps: First, an appropriate synthesis method, such as sol-gel [109], hydrothermal [101], or co-precipitation [90], is used to mix suitable metal salts with basic precipitants, forming a precipitate. Next, through appropriate washing, centrifugation, and drying processes, the precipitate is transformed into nanoparticle form. Finally, through heat treatment or other surface modification methods, the morphology and properties of the nanoparticles can be controlled [111]. The size of nanoparticles and nanocrystals is not primarily dependent on the synthesis method employed, but rather, it is mainly influenced by the preparation and control of the salt solution.

**Table 4.** Summary of the reported spinel ferrite nanosphere-based gas sensors.

Materials	Synthesis	Morphology	Gas	O.T. (°C)	Conc. (ppm)	Response	$t_{res}/t_{rec}$	LOD	Refs.
CoFe <sub>2</sub> O <sub>4</sub>	Solvothermal	Nanospheres	n-butanol	300	100	42.3 a	-	-	[131]
CoFe <sub>2</sub> O <sub>4</sub>	Self-templating	Double-shelled spheres	NH <sub>3</sub>	240	20	0.514 c	19.6/12.1 s	-	[132]
CuFe <sub>2</sub> O <sub>4</sub>	Solvothermal and annealing	Hollow microspheres	TEA	105	10	4 b	32 s/192 s	-	[133]
CuFe <sub>2</sub> O <sub>4</sub>	Solvothermal	Porous nanospheres	Acetone	250	100	20.1 a	3 s/185 s	-	[134]
NiFe <sub>2</sub> O <sub>4</sub>	Metal–organic framework (MOF)	Ultrathin framework	Toluene	230	1	77.3 b	-	2 ppb	[135]
NiFe <sub>2</sub> O <sub>4</sub>	Hydrothermal	Octahedral	Acetone	120	100	18.8 a	6 s/13 s	-	[136]
NiFe <sub>2</sub> O <sub>4</sub>	Solvothermal and annealing	Hollow hexagonal biyramids	n-propanol	120	200	32.19 a	-	-	[137]
NiFe <sub>2</sub> O <sub>4</sub>	Metal–organic framework	Hollow microspindles	Acetone	120	200	52.8 a	14.2 s/-	-	[138]
NiFe <sub>2</sub> O <sub>4</sub>	Hydrothermal and Co-precipitation	Core–shell nanosphere	Acetone	280	100	10.6 a	1 s/7 s	-	[139]
NiFe <sub>2</sub> O <sub>4</sub>	Solvothermal	Porous microspheres	Acetone	250	100	27.4 a	2 s/-	200 ppb	[140]
NiFe <sub>2</sub> O <sub>4</sub>	Refluxing and calcination	Hollow Nano-Octahedrons	Toluene	260	100	6.41 a	25 s/40 s	1 ppm	[141]
NiFe <sub>2</sub> O <sub>4</sub>	Hydrothermal	MOFs-derived fusiforms	Xylene	300	500	31.52 a	50.10 s/40.30 s	10 ppm	[39]
NiFe <sub>2</sub> O <sub>4</sub>	MOF	Polyhedrons	TEA	190	50	18.9 a	6s/-	-	[142]
NiFe <sub>2</sub> O <sub>4</sub>	Annealing	Assembled Fluffy Flowers	Ethanol	120	100	23.2 a	-	-	[143]
NiFe <sub>2</sub> O <sub>4</sub>	Hydrothermal	Core–shell architecture	Toluene	240	100	19.95 a	-	1 ppm	[144]
NiFe <sub>2</sub> O <sub>4</sub>	Metal–organic framework	Nanobox	Ethyl acetate	120	200	64.27 b	23 s/62 s	0.26 ppm	[145]
ZnFe <sub>2</sub> O <sub>4</sub>	Hydrothermal	Hollow spheres	Ethanol	225	1000	42.1 a	10 s/8 s	-	[146]
ZnFe <sub>2</sub> O <sub>4</sub>	Solvothermal	Porous nanospheres	Acetone	200	30	12.4 a	9 s/272 s	-	[147]
ZnFe <sub>2</sub> O <sub>4</sub>	Solvothermal	Yolk–shell microspheres	Acetone	200	50	28.3 a	-	-	[148]
ZnFe <sub>2</sub> O <sub>4</sub>	Solvothermal	Hollow microspheres	Acetone	215	20	11.3 a	10 s/200 s	1 ppm	[149]
ZnFe <sub>2</sub> O <sub>4</sub>	Hydrothermal	Nanoflowers	Acetone	300	2000	36.5 a	-	-	[150]
ZnFe <sub>2</sub> O <sub>4</sub>	Nonaqueous	Nanospheres	Toluene	300	100	9.98 a	18 s/29 s	-	[151]
ZnFe <sub>2</sub> O <sub>4</sub>	Solvothermal	Sphere-like hierarchical architectures	Ethanol	180	10	6.85 a	5.1 s/7.2 s	500 ppb	[152]
ZnFe <sub>2</sub> O <sub>4</sub>	Hydrothermal and thermal	Double-shell microspheres	Acetone	206	20	13.6 a	6 s/10 s	0.13 ppm	[153]
ZnFe <sub>2</sub> O <sub>4</sub>	Hydrothermal and calcination	Hollow spheres	Ethylene glycol	200	100	35.5 a	-	-	[154]

a Response is defined as  $R_a/R_g$ ; b Response is defined as  $R_g/R_a$ ; c Response is defined as  $\Delta R/R_a$ .

By dispersing pure CdSO<sub>4</sub>·8/3H<sub>2</sub>O and Fe(NO<sub>3</sub>)<sub>3</sub>·9H<sub>2</sub>O in ultra-pure water, Liu et al. [43] prepared mixed salt solutions with different Cd/Fe molar ratios, combined with co-precipitation and calcination at different temperatures to prepare CdO-Fe<sub>2</sub>O<sub>3</sub> composite oxide particles. According to XRD verification, the sample with a Cd/Fe ratio of 1/2 was identified as a spinel phase CdFe<sub>2</sub>O<sub>4</sub>, which exhibited the highest sensitivity (48) towards ethanol at 300 °C (Figure 2a). The study conducted by Rao et al. [51] focused on the utilization of the spray pyrolysis deposition technique to fabricate nanocrystalline (Co, Cu, Ni, and Zn) ferrite thin film sensors. The XRD patterns (Figure 2c) show the single cubic spinel phase of the (Co, Cu, Ni, and Zn) ferrite. From Figure 2d, the sensing characteristics of these sensors indicate that the ZnFe<sub>2</sub>O<sub>4</sub> nanocrystalline is more suitable as a sensor at lower temperatures and concentrations. On the other hand, the NiFe<sub>2</sub>O<sub>4</sub> nanocrystalline demonstrates an outstanding LPG sensing ability at higher temperatures.

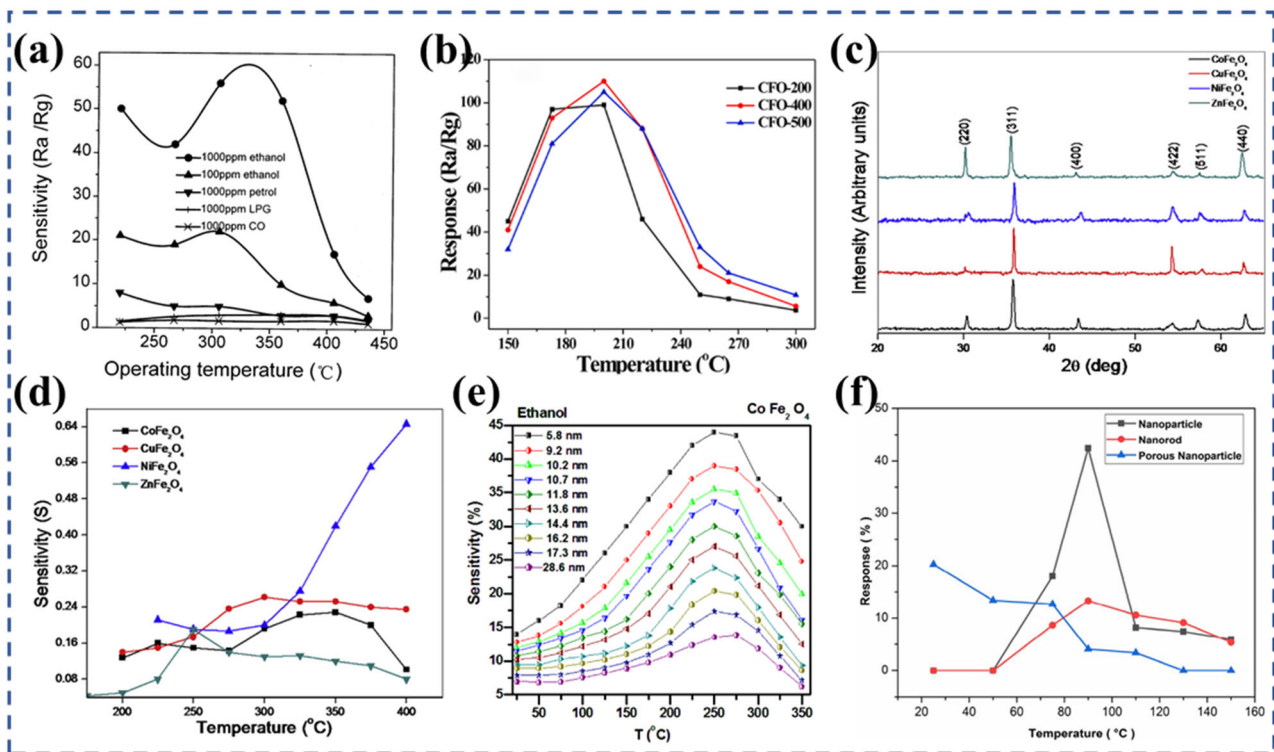


**Figure 2.** (a) The effect of operating temperature of the  $\text{CdFe}_2\text{O}_4$  sensor on the various gas responses. (b) Response of the sensors to 100 ppm ethanol at different operating temperatures. (c) XRD pattern of (Co, Cu, Ni, and Zn) ferrite thin films. (d) Response value of (Co, Cu, Ni, and Zn) ferrite thin films to 5 ppm LPG at different operating temperatures. (e) Size of  $\text{CoFe}_2\text{O}_4$  nanoparticles dependent on response value (%) with varying temperatures for 200 ppm ethanol. (f) The sensitivity of individual  $\text{CoFe}_2\text{O}_4$  sensors to 100 ppm methanol across varying temperature conditions. (a) Reproduced with permission [43], copyright 1998, Elsevier B.V. (b) Reproduced with permission [35], copyright 2022, Elsevier B.V. (c,d) Reproduced with permission [51], copyright 2015, Elsevier B.V. (e) Reproduced with permission [52], copyright 2015, IEEE Xplore. (f) Reproduced with permission [54], copyright 2020, IEEE Xplore.

As discussed earlier, optimizing the grain size and specific surface area of spinel ferrite can significantly enhance the performance of gas sensors. Wei et al. [35] prepared  $\text{CoFe}_2\text{O}_4$  nanoparticles via a hydrothermal method. The CFO-400 sensor, which is calcined at  $400^\circ\text{C}$ , shows promising results with its response value of 110 to 100 ppm ethanol gas at  $200^\circ\text{C}$  (Figure 2b). This not only indicates its high sensitivity, but also showcases its good repeatability and stability, which are crucial characteristics for sensor materials. Rathore et al. [52] prepared  $\text{CoFe}_2\text{O}_4$  nanoparticles with varying particle sizes through the uniaxial press method. The objective of the research was to examine how the sensing performance of the nanoparticles is influenced by factors such as particle size, temperature, and gas flow. The results of the study demonstrated that  $\text{CoFe}_2\text{O}_4$  nanoparticles have good gas sensitivity, and the maximum response value increases with the decrease in particle size. Among them, the response value of 5.8 nm  $\text{CoFe}_2\text{O}_4$  nanoparticles to 5 ppm LPG at  $250^\circ\text{C}$  is the highest, reaching 0.72 (Figure 2e), and its response time and recovery time are 3 s and 48 s, respectively. Halvae et al. [54] employed a hydrothermal synthesis technique to fabricate three distinct nanostructures of  $\text{CoFe}_2\text{O}_4$ , namely nanoparticles, nanorods, and porous nanoparticles. The structures and properties of these nanostructures were analyzed. A cost-effective gas sensor, constructed using a printed circuit board, was utilized to measure methanol gas and assess its performance at different temperatures (Figure 2f). The optimal operating temperatures for the three sensors were found to be  $90^\circ\text{C}$  and room temperature, respectively. At  $90^\circ\text{C}$ , the  $\text{CoFe}_2\text{O}_4$  nanoparticles exhibited a

maximum response value of 42.4%, while the  $\text{CoFe}_2\text{O}_4$  porous nanoparticles demonstrated a maximum response value of 20.26% at room temperature. The  $\text{CoFe}_2\text{O}_4$  nanorods, on the other hand, displayed a maximum response value of 13.3% at 90 °C. In the porous nanoparticle sensor, the optimal temperature was reduced to room temperature due to the high surface volume ratio of the structure.

Sumangala et al. [69] synthesized the  $\text{MgFe}_2\text{O}_4$  nanoparticles employing both the co-precipitation and sol-gel methods. The XRD patterns presented in Figure 3a demonstrate the similarity in the structural characteristics of both samples. The co-precipitation sample exhibited a smaller particle size and twice the BET surface area compared with the sol-gel combustion sample. The electrical properties and  $\text{CO}_2$  sensing capabilities of these two  $\text{MgFe}_2\text{O}_4$  nanoparticles were investigated (Figure 3b). Notably, the co-precipitated sample demonstrated a higher sensing response of 36%, whereas the sol-gel combusted sample achieved a sensing response of 24%. Ghosh et al. [78] reported nanocrystalline  $\text{NiFe}_2\text{O}_4$  (Figure 3c) through the sol-gel auto-combustion method. Ball milling was performed at room temperature and particle size was controlled to optimize the sensitivity of  $\text{H}_2$  and  $\text{H}_2\text{S}$ . The experimental results show that there was a notable enhancement in the gas response when the particle size was reduced or the specific surface area was increased (Figure 3d). Compared with the other test gases,  $\text{NiFe}_2\text{O}_4$  nanocrystals with a particle size of  $\sim 5.35$  nm had a response value of  $\sim 58\%$  to 200 ppm  $\text{H}_2$  at 100 °C and  $\sim 75\%$  to 200 ppm  $\text{H}_2\text{S}$  at 150 °C.

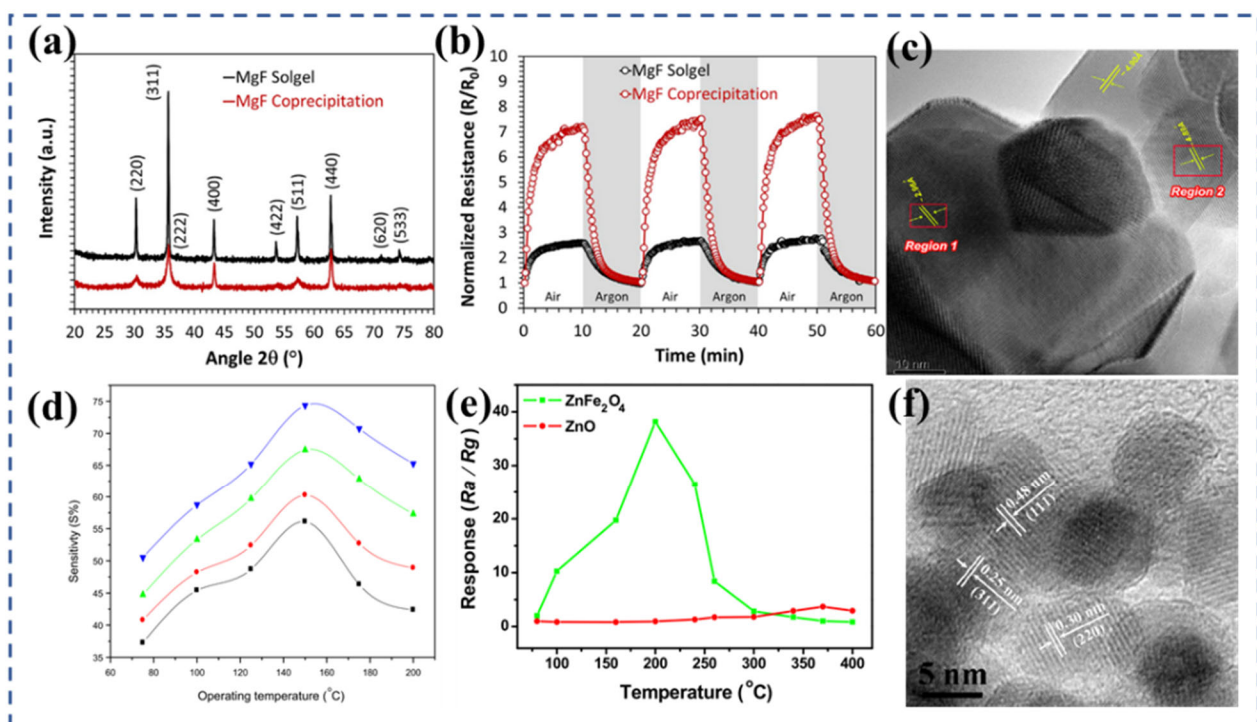


**Figure 3.** (a) XRD of the synthesized  $\text{MgFe}_2\text{O}_4$  samples. (b) Variation in the response of  $\text{MgFe}_2\text{O}_4$  samples at 300 °C. (c) HRTEM image showing cubic  $\text{NiFe}_2\text{O}_4$ . (d)  $\text{H}_2\text{S}$  sensitivity of  $\text{NiFe}_2\text{O}_4$  with various milled times at operating temperatures. (e) Responses of sensors to 500 ppm acetone at various temperatures. (f) TEM images of the synthesized  $\text{ZnFe}_2\text{O}_4$  nanoparticles. (a,b) Reproduced with permission [69], copyright 2018, Elsevier B.V. (c,d) Reproduced with permission [78], copyright 2015, Elsevier B.V. (e,f) Reproduced with permission [92], copyright 2015, Elsevier B.V.

In a study conducted by Karpova et al. [88],  $\text{ZnO}$ ,  $\text{Fe}_2\text{O}_3$ , and zinc ferrite  $\text{ZnFe}_2\text{O}_4$  nanopowders were prepared using the co-precipitation method. The gas-sensitive results proved that the sensitivity of  $\text{ZnFe}_2\text{O}_4$  towards ethanol and acetone was significantly higher compared with the simple oxides, with values ranging from one to two orders of magnitude greater, respectively. This enhanced gas sensitivity of  $\text{ZnFe}_2\text{O}_4$  can be

attributed to the presence of a high concentration of acidic Bronsted centers that contain active protons. These centers facilitate participation in REDOX reactions and selectively adsorb ethanol based on the acid–base mechanism. Using the hydrothermal method, Zhang et al. [92] successfully synthesized ZnFe<sub>2</sub>O<sub>4</sub> nanoparticles (about 10 nm) (Figure 3f). The phase and morphology of the prepared products were strongly influenced by the reaction conditions, including the reaction time, temperature, and the molar ratio of raw materials. The experimental findings (Figure 3e) revealed that the prepared ZnFe<sub>2</sub>O<sub>4</sub> nanoparticles exhibited a significantly higher response value of 39.5 to 200 ppm acetone compared with the precursor ZnO, which only had a response value of 4.2, at 200 °C.

Cao et al. [93] employed a solid-state chemical reaction to synthesize various MFe<sub>2</sub>O<sub>4</sub> (M = Fe, Co, Ni, Mg, Cd, and Zn) ferrite materials with distinct morphologies. Compared with traditional semiconductor oxides, these prepared ferrites exhibited enhanced gas sensitivity at lower operating temperatures and demonstrated rapid response and recovery characteristics. At 260 °C, ZnFe<sub>2</sub>O<sub>4</sub> displayed a response value of 37.3 towards 100 ppm methanol (Figure 4a), which was the highest gas response among the different ferrites. It exhibited a response value of 29.1 towards 100 ppm ethanol (Figure 4b) with fast response and recovery times of 5 s and 26 s, respectively. Li et al. [99] successfully synthesized ultra-small ZnFe<sub>2</sub>O<sub>4</sub> nanoparticles (Figure 4c) using the hydrothermal synthesis method. These nanoparticles exhibited excellent selectivity towards NO<sub>2</sub> molecules. The ZnFe<sub>2</sub>O<sub>4</sub>-based sensor showed an impressive response with a gas-to-air ratio ( $R_{\text{gas}}/R_{\text{air}}$ ) of 247.7 toward 10 ppm NO<sub>2</sub> at 125 °C (Figure 4d), which is a relative low temperature. It also demonstrated a fast response and recovery characteristic (6.5 s/11 s). Li et al. [94] further investigated the mechanism behind the superior selectivity and sensing performance of ZnFe<sub>2</sub>O<sub>4</sub> towards NO<sub>2</sub> compared with other gases. Through non-in situ photoluminescence (PL) characterization and density functional theory (DFT) calculations, they found that the gas-sensitive mechanism of ZnFe<sub>2</sub>O<sub>4</sub> towards NO<sub>2</sub> is based on surface charge transfer. The presence of oxygen vacancies in the material also enhanced the adsorption energy and charge transfer between ZnFe<sub>2</sub>O<sub>4</sub> and NO<sub>2</sub> molecules on the surface.

Zhang et al. [110] synthesized ZnFe<sub>2</sub>O<sub>4</sub> nanoparticles using a solvothermal method with zinc acetylacetonate and iron acetylacetonate as the precursors. By carrying out the synthesis at 150 °C, ZnFe<sub>2</sub>O<sub>4</sub> nanoparticles (Figure 4e) with a diameter of approximately 20 nm were obtained. These ZnFe<sub>2</sub>O<sub>4</sub> nanoparticles exhibited excellent gas-sensing capabilities, particularly for H<sub>2</sub>S gas. The sensor was able to detect H<sub>2</sub>S gas as low as 1 ppm at a temperature of 135 °C, with a sensor response reaching 15.1 for 5 ppm H<sub>2</sub>S gas at the same temperature (Figure 4f). These results suggest that nano-ZnFe<sub>2</sub>O<sub>4</sub> holds great promise for the development of H<sub>2</sub>S gas sensors. The group of Jha et al. [102] conducted a study on a selective hydrogen H<sub>2</sub>S gas sensor based on a zinc ferrite film (Figure 4g). The film was prepared using microwave-assisted solvent-thermal deposition. The sensor exhibited an excellent performance at an operating temperature of 250 °C. The response range of the sensor was found to be 1872–90% for H<sub>2</sub>S gas concentrations ranging from 5.6 ppm to 0.3 ppm. Through density functional theory calculations, the researchers concluded that the rapid rise and fall times of H<sub>2</sub>S (approximately 40 s and 70 s, respectively) and the complete recovery of the device were attributed to the physical adsorption of H<sub>2</sub>S molecules on the partially reversed ZnFe<sub>2</sub>O<sub>4</sub> surface. Figure 4h shows the total density of states (TDOS) of the ZnFe<sub>2</sub>O<sub>4</sub>. In the experiment, a double-difference subtraction automatic balance interface circuit was utilized to drive the sensor, and the noise signal was accurately processed and compensated through the differential output.

### 3.2. Nanorods/Nanotubes

The synthesis methods for spinel ferrite nanorods, nanotubes, and nanowires primarily include hydrothermal [113] and electrospinning [123] techniques. Nanofibers constructed via electrospinning exhibit uniformity and smoothness, thus making the technique widely utilized in the preparation of one-dimensional materials.

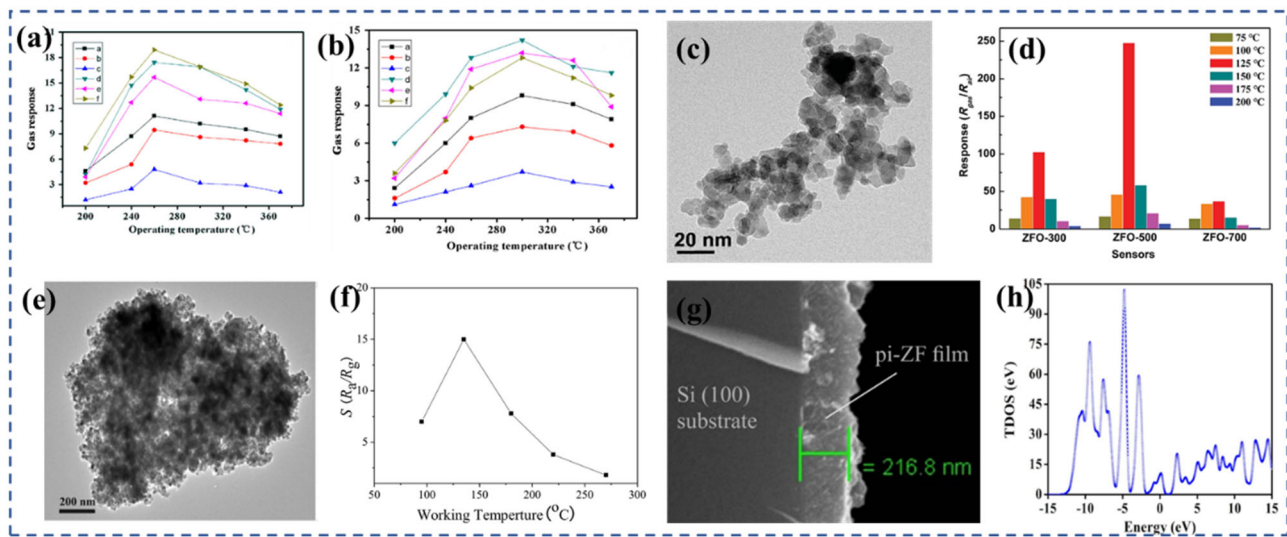


**Figure 4.** (a) The sensitivity–temperature characteristics of various  $MFe_2O_4$  sensors in detecting formaldehyde. (b) The sensitivity–temperature characteristics of various  $MFe_2O_4$  sensors in detecting formaldehyde ethanol: (a)  $Fe_3O_4$ , (b)  $CoFe_2O_4$ , (c)  $NiFe_2O_4$ , (d)  $MgFe_2O_4$ , (e)  $CdFe_2O_4$ , (f)  $ZnFe_2O_4$ . (c) TEM image of the  $ZnFe_2O_4$  nanoparticles. (d) Comparative analysis of the  $NO_2$  response among sensors based on ZFO-300, ZFO-500, and ZFO-700 materials when exposed to 10 ppm  $NO_2$  at varying operating temperatures. (e) The TEM image of  $ZnFe_2O_4$  nanoparticles at low magnification. (f) The response values of sensors based on  $ZnFe_2O_4$  nanoparticles to 5 ppm  $H_2S$  gas at different working temperatures. (g) Cross-sectional FESEM image of the  $ZnFe_2O_4$  film. (h) Total density of states (TDOS) of the  $ZnFe_2O_4$ . (a,b) Reproduced with permission [93], copyright 2016, Elsevier B.V. (c,d) Reproduced with permission [99], copyright 2019, Royal Society of Chemistry. (e,f) Reproduced with permission [110], copyright 2018, Elsevier B.V. (g,h) Reproduced with permission [102], copyright 2022, IEEE Xplore.

In the field of gas sensing, there is a growing interest in one-dimensional (1D) nanostructures such as nanorods, nanotubes, and nanowires, as they are gaining more attention compared with nanoparticles. The reasons for this are manifold. (1) One-dimensional nanostructures often have more active sites compared with nanoparticles. These active sites are the locations where the gas molecules can interact with the material, thereby inducing a detectable change (such as a change in resistance). Therefore, having more active sites means the material can interact with more gas molecules simultaneously, enhancing the sensitivity of the sensor [111]. (2) One-dimensional nanostructures such as nanotubes have unique gas diffusion characteristics. Their channel-like structure allows gas molecules to easily diffuse and permeate through the material. This not only increases the interaction between the gas and the material, but also improves the speed of detection, making the sensor more responsive [119]. (3) Nanotubes and similar structures typically have a relatively high specific surface area [114]. A higher surface area means more space for gas molecules to interact with the material, which further improves the sensitivity of the sensor. One-dimensional nanostructures are known for their favorable electronic characteristics. For instance, nanowires can efficiently transport carriers, which is crucial in transducing the interaction between the gas and the material into a detectable electrical signal. In summary, because of their unique structural and electronic properties, materials with 1D nanostructures such as nanorods, nanotubes, and nanowires offer significant advantages in gas sensing and are being actively explored as potential gas-sensing materials.

To investigate the impact of structure on the gas-sensing performance of a sensor, Zhang et al. [113] utilized a high-efficiency anodic alumina template method and a hydrothermal method to prepare  $NiFe_2O_4$  hollow nanotubes with a length of 1  $\mu m$  and a diameter of 100 nm, as well as  $NiFe_2O_4$  nanoparticles, respectively. In comparison with the  $NiFe_2O_4$  nanoparticles sensor, the  $NiFe_2O_4$  nanotube sensor possessed a porous structure

with overlapping nanotubes, which facilitated improved gas sensitivity. During testing with different  $\text{NH}_3$  gas concentrations, the  $\text{NiFe}_2\text{O}_4$  nanotubes sensor exhibited a higher response compared with the  $\text{NiFe}_2\text{O}_4$  nanoparticles sensor, albeit with a slower recovery speed. The high specific surface area of the nanotubes played a crucial role in the ability of the  $\text{NiFe}_2\text{O}_4$  nanotubes sensor to detect  $\text{NH}_3$  gas. Wang et al. [115] developed a novel gas-sensing material,  $\text{NiFe}_2\text{O}_4$  porous nanorods (Figure 5a,b), which exhibited improved sensitivity and selectivity for detecting the harmful gas n-propanol. These porous javelin-such as nanorods were synthesized using Ni/Fe bimetallic metal–organic frameworks as templates. As a gas-sensing material, ferrite demonstrated n-type gas-sensing behavior with reduced resistance in a reducing gas atmosphere. The  $\text{NiFe}_2\text{O}_4$  nanorods exhibited an outstanding sensing performance for n-propanol (Figure 5c), with an extremely low detection limit of 0.41 ppm at 120 °C. At the same time, the sensor had a good selectivity to n-propanol, good cycle stability, and long-term stability. The exceptional performance of  $\text{NiFe}_2\text{O}_4$  nanorods can be attributed to their distinctive morphology and porous structure. The large number of reaction sites offered by the porous structure facilitated the accelerated diffusion of n-propanol gas, allowing the sensor to quickly and accurately detect the presence of the gas. Chu et al. [116] conducted a study where they prepared  $\text{NiFe}_2\text{O}_4$  nanorods (Figure 5d) and nanocubes using the hydrothermal method. The nanorods had a length of approximately 1  $\mu\text{m}$  and a diameter of about 30 nm, while the nanocubes had a side length of around 60–100 nm. The results of the study showed that the sensor based on  $\text{NiFe}_2\text{O}_4$  nanorods exhibited high sensitivity and selectivity towards triethylamine. Specifically, it achieved a sensitivity of 7 when detecting 1 ppm of triethylamine at 175 °C. However, the  $\text{NiFe}_2\text{O}_4$  nanocube-based sensor demonstrated a unique conductivity response in the  $\text{NH}_3$  environment, showing a significant increase. Specifically, when exposed to 500 ppm triethylamine, the sensor exhibited a response of 0.033. In contrast, the sensors based on  $\text{NiFe}_2\text{O}_4$  nanocubes exhibited a different behavior. In a reducing gas atmosphere, the conductivity of the sensor increased. The shape of the crystal, whether nanorods or nanocubes, significantly influenced not only the response value of the gas, but also the type of semiconductor behavior observed.

Nguyen et al. [123] demonstrated the sensitivity of  $\text{ZnFe}_2\text{O}_4$  nanofiber (Figure 5e) sensors to  $\text{H}_2\text{S}$ , achieving a response of 102 to 1 ppm  $\text{H}_2\text{S}$ , along with excellent resistance to humidity and a short response time of 12 s. Zhu et al. [119] synthesized porous  $\text{ZnFe}_2\text{O}_4$  nanorods using a microemulsion system with calcination at 500 °C. The resulting  $\text{ZnFe}_2\text{O}_4$  nanorods had a diameter of approximately 50 nm, composed of  $\text{ZnFe}_2\text{O}_4$  nanocrystals (with a diameter of 5–10 nm) arranged linearly. Compared with  $\text{ZnFe}_2\text{O}_4$  nanoparticles, porous  $\text{ZnFe}_2\text{O}_4$  nanorods exhibited superior gas-sensing properties to ethanol at room temperature. The enhanced sensing performance can be ascribed to the random arrangement of the porous nanorods and the existence of interconnected porous channels. These factors significantly augmented the specific surface area of the nanorods, facilitating effective diffusion of the target gas for detection. Additionally, the smaller grain size of  $\text{ZnFe}_2\text{O}_4$  offered a greater number of active sites, matching the thickness of the electron-depleted region, thereby amplifying the response. Li et al. [122] conducted a study where  $\text{ZnFe}_2\text{O}_4$  nanorods (Figure 5f) with a porous structure were synthesized using the hydrothermal method, with  $\text{ZnFe}_2(\text{C}_2\text{O}_4)_3$  serving as the template. These nanorods were composed of small nanoparticles and exhibited a significant number of surface pores. The porous  $\text{ZnFe}_2\text{O}_4$  nanorods sensor demonstrated a rapid response to acetone, with a response of 52.8 and response/recovery times of 1/11 s at 260 °C for 100 ppm acetone. The exceptional response observed in the porous  $\text{ZnFe}_2\text{O}_4$  nanorods sensor can be attributed to several factors, including the fine nanoparticle size, suitable pore size, and reticular pore structure. These characteristics contribute to enhanced gas adsorption and diffusion, allowing for a rapid response to acetone. However, it is important to note that when the concentration of acetone exceeded 100 ppm, the desorption capacity of the sensing material became insufficient compared with its adsorption capacity. As a result, the sensor exhibited a stable response instead of a further increase in signal intensity.

### 3.3. Nanosheets

The preparation methods for spinel ferrite nanosheets primarily include template hydrothermal [129], sol–gel [127], and spray pyrolysis techniques [128]. The template hydrothermal method can prepare nanosheets with specific pore structures and morphologies, but the demolding step may limit the sample’s morphology and structure [129]. The sol–gel method can prepare spinel ferrite nanosheets with specific compositions and structures, but it tends to introduce impurities [127]. Spray pyrolysis can produce thinner nanosheet films with good lattice matching and crystallinity, but the equipment cost is high and the operation is relatively complex [128].

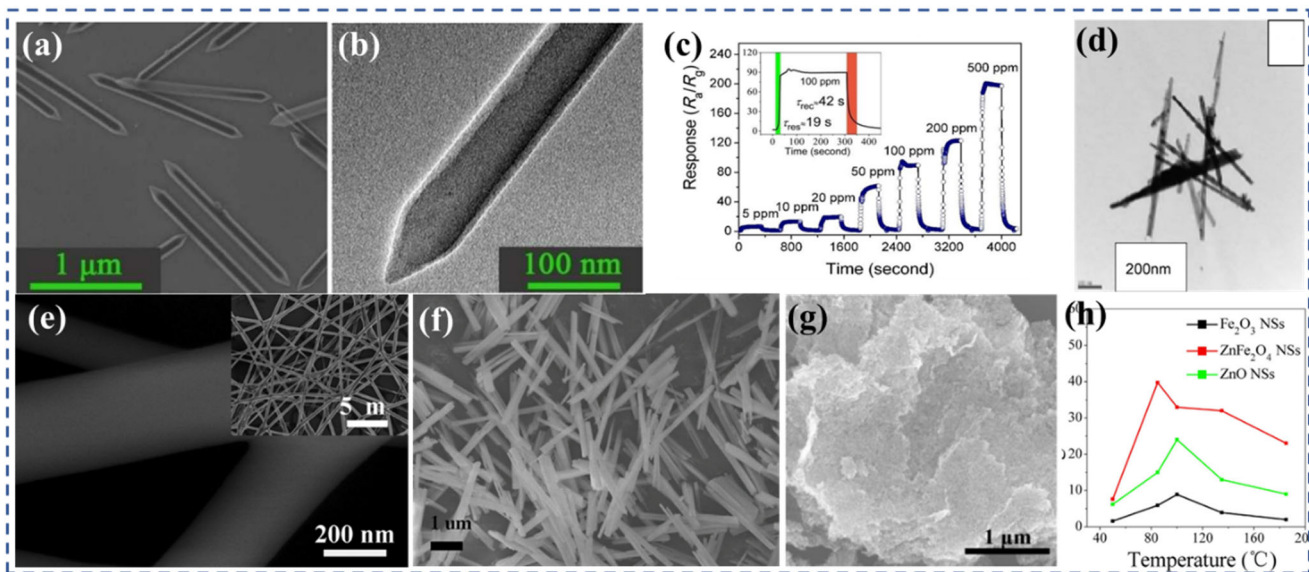


**Figure 5.** (a) SEM image and (b) TEM image of as-prepared  $\text{NiFe}_2\text{O}_4$  nanorods. (c) The dynamic response–recovery characteristics of  $\text{NiFe}_2\text{O}_4$  nanorods to n-propanol at different concentrations. Insert: response and recovery curve of the sensor to 100 ppm n-propanol. (d) TEM image of  $\text{NiFe}_2\text{O}_4$  nanorods. (e) SEM images of  $\text{ZnFe}_2\text{O}_4$  nanofiber. (f) SEM images of porous  $\text{ZnFe}_2\text{O}_4$  nanorods. (g) SEM images of  $\text{ZnFe}_2\text{O}_4$  nanosheets. (h) The response values of the sensors to 1 ppm  $\text{H}_2\text{S}$  at various operating temperatures. (a–c) Reproduced with permission [115], copyright 2018, Wiley-VCH. (d) Reproduced with permission [116], copyright 2007, Elsevier B.V. (e) Reproduced with permission [123], copyright 2018, Elsevier B.V. (f) Reproduced with permission [122], copyright 2017, Elsevier B.V. (g,h) Reproduced with permission [129], copyright 2017, Elsevier B.V.

Nanosheets are a type of two-dimensional nanomaterial characterized by their flat, sheet-like structure. Due to their unique morphology, nanosheets possess a large surface area-to-volume ratio, providing an abundance of reaction sites and diffusion paths for gases to interact with. This increased surface area and availability of reaction sites contribute to improved gas-sensing properties, such as enhanced sensitivity and selectivity. The highly exposed surface of nanosheets allows for efficient gas adsorption and interaction, making them promising candidates for gas-sensing applications.

Singh et al. [126] prepared high-porous  $\text{CuFe}_2\text{O}_4$  cascade nanostructures by sol–gel method. It has a porous structure  $\text{CuFe}_2\text{O}_4$  with pore size between 10–15 nm. The results of the sensing experiments demonstrate that the porous  $\text{CuFe}_2\text{O}_4$  layered structure exhibits a high sensing response of 96% when exposed to LPG at a temperature of 25 °C. Moreover, it demonstrates excellent repeatability and rapid response recovery characteristics. Gao et al. [129] successfully synthesized porous  $\text{ZnFe}_2\text{O}_4$  nanosheets (Figure 5g) by utilizing graphene sheets as a rigid template. The resulting  $\text{ZnFe}_2\text{O}_4$  nanosheets had pores with a size range of 5–50 nm and were composed of nanoparticles with a diameter of approximately 10–20 nm. In comparison to  $\text{Fe}_2\text{O}_3$  nanoparticles,  $\text{ZnO}$  nanoparticles, and  $\text{ZnFe}_2\text{O}_4$  nanoparticles, the sensor based on  $\text{ZnFe}_2\text{O}_4$  nanosheets exhibited faster

response and recovery times (39 s/43 s), higher response ( $R_a/R_g = 123$ ) and excellent selectivity. The sensor also demonstrated good repeatability and stability. Moreover, the unique mesoporous  $ZnFe_2O_4$  nanosheets enabled the detection of  $H_2S$  gases as low as 500 ppb at  $85\text{ }^\circ\text{C}$  (Figure 5h). The enhanced performance of the  $ZnFe_2O_4$  nanosheets can be ascribed to their high specific surface area and porous characteristics. The increased specific surface area provides more active sites for gas molecule adsorption and reaction, enhancing the gas-sensing response. The porous structure of the nanosheets allows for the diffusion of target gas molecules, facilitating their interaction with the sensing material. Additionally, the two-dimensional structure of the nanosheets prevents the aggregation of nanoparticles, ensuring a larger effective surface area for gas sensing and maintaining the structural integrity of the material. Overall, the combination of high specific surface area, porous features, and two-dimensional structure contributes to the enhanced gas-sensing performance of  $ZnFe_2O_4$ .

### 3.4. Nanospheres

Spinel ferrite nanospheres can be classified into solid spheres [147], hollow spheres [149], core–shell spheres [139], and double-shell (or triple-shell) spheres [153]. They are mainly prepared using solvent thermal methods or metal–organic framework (MOF) [142] methods. In recent years, the template-free solvent thermal method has become the mainstream approach for synthesizing three-dimensional spinel ferrite materials.

Nanospheres typically consist of solid spheres or hollow spheres that can evolve from the core–shell structure. They are characterized by their low density, high specific surface area, pronounced surface activity, and notable stability [148]. Previous research suggests that to achieve a larger specific surface area, it is essential to decrease the size of the nanoparticles. Assembling nanoparticles into nanospheres allows for better control over the size, resulting in larger specific surface areas and higher sensitivity. The enhanced reactivity and gas-sensing performance of nanospheres can be attributed to their increased surface area-to-volume ratio.

Zhai et al. [142] conducted a study where they synthesized  $NiFe_2O_4$  polyhedron structures (Figure 6a) derived from metal–organic frameworks (MOF) using solvothermal synthesis. By altering the solvent composition, they were able to synthesize large  $NiFe_2O_4$  polyhedra with a more stable morphology and structure. These large polyhedra exhibited excellent gas-sensing properties for TEA. Notably, they demonstrated a fast response time of 6 s to 50 ppm TEA, an enhanced response value of 18.9 to 50 ppm TEA (Figure 6b), and showed good selectivity and repeatability at relatively low operating temperatures of  $190\text{ }^\circ\text{C}$ . The fast response rate of the sample can be attributed to its unique dense hollow structure. The hollow structure enables the REDOX reaction between TEA molecules and the material to occur predominantly at the surface/interface, while the interior of the material remains inactive. This reduces the electron conduction path, leading to the observed fast response time. Qu et al. [153] conducted research on the synthesis of  $ZnFe_2O_4$  double-shell microspheres using a hydrothermal method and thermal treatment. Figure 6e is the XRD pattern of the yolk–shell, double-shell hollow spheres, and solid microspheres. Compared with the yolk–shell and solid microspheres, the  $ZnFe_2O_4$  double-shell hollow spheres not only reduced the operating temperature of the sensor, but also enhanced its acetone sensitivity because of the improved crystallinity and larger specific surface area. The sensor displayed a response of 2.6 to 5 ppm acetone at  $206\text{ }^\circ\text{C}$  (Figure 6f), with a response time of 6 s and a recovery time of 10 s. Furthermore, it is noteworthy that the detection limit for acetone achieved by the sensor was reported to be 0.13 ppm. This value is significantly below the established risk level for life and health, which is 20,000 ppm. Additionally, it is well below the diagnostic threshold for diabetes, which is set at 0.8 ppm. This indicates the high sensitivity and potential of the sensor in accurately detecting and monitoring acetone levels in various applications.

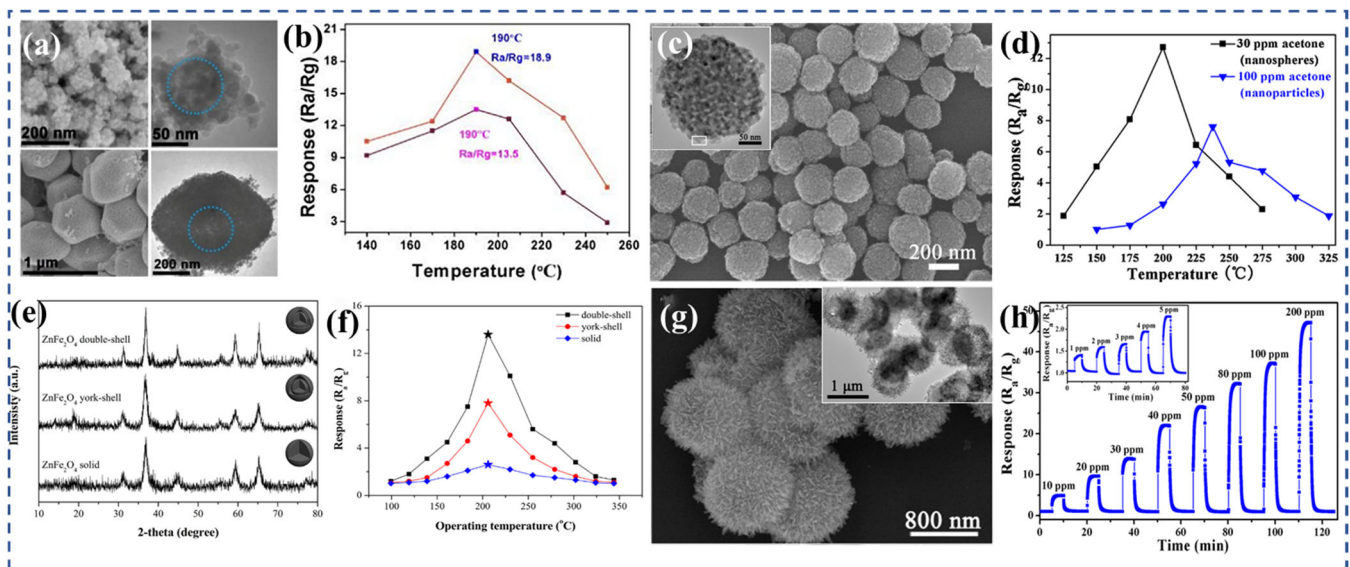


**Figure 6.** (a) SEM and TEM images of the  $\text{NiFe}_2\text{O}_4$  polyhedron. (b) The response comparison of sensors to 50 ppm TEA at various temperatures. (c) SEM image and TEM image (inset) of the  $\text{ZnFe}_2\text{O}_4$  sphere. (d) Comparative analysis of the 30 ppm acetone response of porous  $\text{ZnFe}_2\text{O}_4$  nanospheres and the 100 ppm acetone response of  $\text{ZnFe}_2\text{O}_4$  nanoparticles at varying operating temperatures. (e) XRD patterns of  $\text{ZnFe}_2\text{O}_4$  double-shell, yolk-shell, and solid microspheres. (f) The sensitivity–temperature characteristics of the  $\text{ZnFe}_2\text{O}_4$  double-shell, yolk-shell, and solid microsphere-based sensors in detecting 20 ppm acetone. (g) SEM image and TEM image (inset) of the hierarchical  $\text{ZnFe}_2\text{O}_4$  microspheres. (h) Dynamic curve of the gas sensor to acetone with different concentrations at 215 °C. (a,b) Reproduced with permission [142], copyright 2020, Royal Society of Chemistry. (c,d) Reproduced with permission [147], copyright 2015, Elsevier B.V. (e,f) Reproduced with permission [153], copyright 2018, Elsevier B.V. (g,h) Reproduced with permission [149], copyright 2015, American Chemical Society.

Zhou et al. [147] successfully synthesized porous  $\text{ZnFe}_2\text{O}_4$  nanospheres (Figure 6c) using a template-free solvothermal method, followed by annealing at 400 °C. These nanospheres consisted of numerous nanoparticles and possessed a pore size ranging from 10 to 20 nm. The distinctive porous spherical structure greatly improved the sensor's acetone sensing performance. The response value for 30 ppm acetone reached 11.8, which is 2.5 times higher compared with that for the  $\text{ZnFe}_2\text{O}_4$  nanoparticles (Figure 6d). A swift response time of 9 s showcased its ability to promptly detect and react to variations in the target gas. However, the recovery time was relatively longer, taking 272 s. Subsequently, Zhou et al. [149] employed a template-free solvent-heat treatment followed by heat treatment at 400 °C for 2 h to fabricate  $\text{ZnFe}_2\text{O}_4$  hollow microspheres assembled with nanosheets (Figure 6g). The nanosheets within the microspheres had an average thickness of 20 nm, while the hollow microspheres themselves had diameters ranging from 0.9 to 1.1  $\mu\text{m}$ . The hollow flower-like structure offered multitudes of adsorption/reaction sites, and the presence of diffusion channels, primarily distributed in the aperture range of 2 to 50 nm, facilitated the diffusion of target gases. At an operating temperature of 215 °C, the sensor exhibited a response value of 37.3 to 100 ppm acetone (Figure 6h) and demonstrated good long-term stability. However, under the same conditions, the response to ethanol was also high, measuring at 27.0. The presence of layered hollow structures in semiconductor oxides can enhance the diffusion of target gases, making them advantageous for gas-sensor applications.

## 4. Doping

Element doping is indeed a powerful strategy to enhance the structure and performance of spinel ferrite materials, and there has been a growing interest in this research area recently. While earlier studies on spinel ferrite doping mostly concentrated on applications such as electrodes and magnetism, recent advancements have shed light on the importance of doping for optimizing gas-sensing properties. However, not all metallic elements are suitable for doping in spinel ferrite materials. Preferably, elements with donor characteristics (high valence elements that can donate electrons) or acceptor characteristics (low valence elements that can accept electrons) are used for modification. Doping in spinel ferrite materials can occur in two forms. The first form of doping involves displacement, where the  $M^{2+}$  (A site) and  $Fe^{3+}$  (B site) ions in the spinel ferrite are replaced by the doping elements. This changes the composition of the spinel ferrite and can affect its properties, such as A-site doping [155], B-site doping [156], and AB-site doping [157]. The second involves the incorporation of doping elements into the tetrahedral and octahedral interstices of  $MFe_2O_4$  crystals. This results in a solid solution structure, where the doping elements are homogeneously dispersed within the host material [158]. Doping can significantly alter the composition and microstructure of spinel ferrite materials, influencing characteristics such as crystallinity [159]. These changes can, in turn, affect the reference resistance [160] and gas-sensing performance [161] of the ferrite-based gas sensors. For instance, doping can enhance the sensitivity [162], selectivity [163], response speed [28], and stability [164] of the sensors. In this section, we will review the latest research progress on element doping in spinel ferrite materials and its influence on their gas-sensing properties (Tables 5–9). The focus will be on how different doping elements can affect the sensor's performance, the optimal doping concentrations, and the underlying mechanisms behind these effects. This review will provide valuable insights for the design and fabrication of high-performance ferrite-based gas sensors.

### 4.1. A Site Doping

Compounds of the  $MFe_2O_4$  type, where M represents elements such as Mg, Cu, Zn, Ni, and Co, are widely utilized in the field of sensors due to their favorable surface activity. The study conducted by Mukherjee et al. [155] presents an interesting perspective on how the morphology and structure of ferrite-based materials can influence their gas-sensing properties. In their research, they synthesized one-dimensional  $Mg_{0.5}Zn_{0.5}Fe_2O_4$  hollow tubes using a wet chemical process assisted by an alumina template. They evaluated the gas-sensitive properties of two versions of these nanotubes: one version was embedded in a porous alumina template (Figure 7a) and the other was isolated and coated on a quartz substrate (Figure 7e). The nanotubes exhibited good responsiveness to  $H_2$ , CO, and  $N_2O$  gases in both configurations. Interestingly, they observed a difference in the behavior of the nanotubes based on their configuration. Regardless of the type of test gas, the concentration of the test gas, or the operating temperature, the embedded nanotubes consistently behaved as N-type semiconductors. N-type semiconductors are characterized by an excess of electrons (Figure 7b,c). On the other hand, the isolated nanotubes behaved as P-type semiconductors (Figure 7f,g), which are characterized by a deficiency of electrons or an excess of "holes" for the electrons. This inversion from N-type to P-type dominance of carriers, when going from embedded to isolated nanotubes, is a significant finding. It suggests that the electronic properties of ferrites can be customized by changing their surface-to-volume ratio. In other words, by altering the physical configuration of the ferrites (from embedded to isolated), it is possible to control their semiconductor behavior. This finding opens up new possibilities for the design and fabrication of ferrite-based gas sensors, as it introduces an additional degree of tunability in their properties.

**Table 5.** Summary of the reported spinel ferrite A-site doping-based gas sensors.

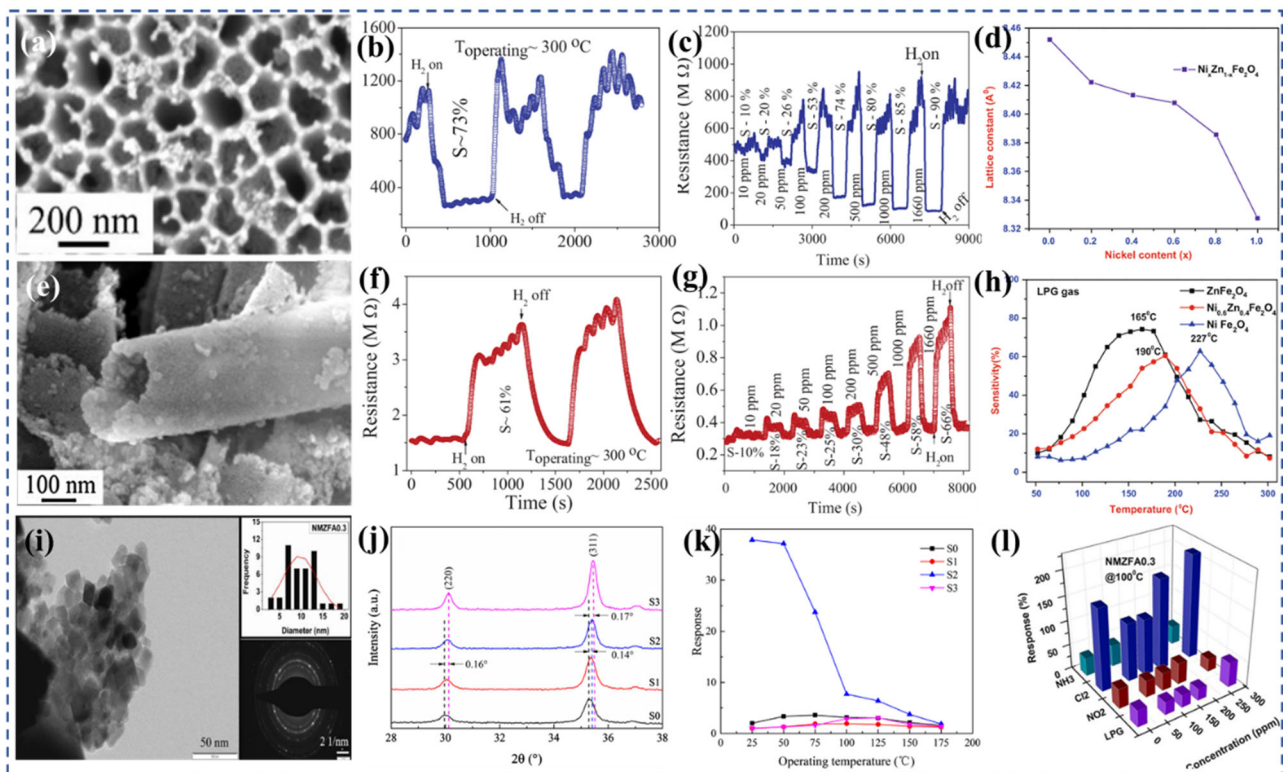
Materials	Synthesis	Morphology	Gas	O.T. (°C)	Conc. (ppm)	Response	t <sub>res</sub> /t <sub>rec</sub>	LOD	Refs.
Mg <sub>0.9</sub> Sn <sub>0.1</sub> Fe <sub>2</sub> O <sub>4</sub>	Auto-combustion	Nanoparticle (100 nm)	acetone	380	-	0.83 c	3 min/-	-	[165]
Zn <sub>0.6</sub> Mn <sub>0.4</sub> Fe <sub>2</sub> O <sub>4</sub>	Sol-gel citrate	Nanoparticle (30–35 nm)	ethanol	300	200	0.78 c	-	-	[166]
Ni <sub>0.6</sub> Zn <sub>0.4</sub> Fe <sub>2</sub> O <sub>4</sub>	Sol-gel	Nanoparticle (28–42 nm)	H <sub>2</sub> S	225	50	0.65 c	-	-	[167]
Ni <sub>0.4</sub> Zn <sub>0.6</sub> Fe <sub>2</sub> O <sub>4</sub>	Aerosol pyrolysis	Spherical shape (250–600 nm)	NH <sub>3</sub>	350	12.5	0.55 c	-	-	[168]
Cu <sub>0.5</sub> Co <sub>0.5</sub> Fe <sub>2</sub> O <sub>4</sub>	Auto-combustion	Nanoparticle (23–43 nm)	H <sub>2</sub> O	RT	80%	11.7	-	-	[169]
10 wt% Ni and 0.2 wt% Sm doped CoFe <sub>2</sub> O <sub>4</sub>	Sol-gel citrate	Nanoparticle (40 nm)	H <sub>2</sub> S	200	1000	0.78 c	5 s/20 s	-	[162]
Ni <sub>0.3</sub> Zn <sub>0.7</sub> Fe <sub>2</sub> O <sub>4</sub>	Sol-gel auto combustion	Nanoparticles	Acetone	275	500	2 c	120 s /300 s	-	[160]
Co <sub>0.8</sub> Ni <sub>0.2</sub> Fe <sub>2</sub> O <sub>4</sub>	Solvothermal	Nanoparticles (40–90 nm)	NH <sub>3</sub>	-	4000	2.8 a	-	-	[170]
Mn <sub>0.2</sub> Ni <sub>0.8</sub> Fe <sub>2</sub> O <sub>4</sub>	Hydrothermal	Nanoparticle (<100 nm)	H <sub>2</sub> O	RT	1000	0.56 c	110 s /160 s	-	[171]
Mg <sub>0.5</sub> Zn <sub>0.5</sub> Fe <sub>2</sub> O <sub>4</sub>	Sol Pechini	Embedded nano-tubes	H <sub>2</sub>	350	1660	0.9 c	-	-	[155]
Mg <sub>0.5</sub> Zn <sub>0.5</sub> Fe <sub>2</sub> O <sub>4</sub>	Sol Pechini	Isolated nano-tube	H <sub>2</sub>	350	1660	0.66 d	-	-	[24]
Ni <sub>0.5</sub> Zn <sub>0.5</sub> Fe <sub>2</sub> O <sub>4</sub>	Co-precipitation	Nanoparticles	NH <sub>3</sub>	305	200	0.7 c	-	-	[24]
Mg <sub>0.5</sub> Zn <sub>0.5</sub> Fe <sub>2</sub> O <sub>4</sub>	Sol-gel auto combustion	Nanoparticles (58 nm)	acetone	325	20	0.32 c	137 s /247 s	-	[172]
Mn-CuFe <sub>2</sub> O <sub>4</sub>	Auto-combustion	Nanoparticles (9–45 nm)	LPG	300	1000	0.27 c	-	-	[173]
Mn-CuFe <sub>2</sub> O <sub>4</sub>	Evaporation	Nanoparticles	LPG	250	1000	0.25 c	40 s/40 s	-	[174]
Zn <sub>0.8</sub> Cu <sub>0.2</sub> Fe <sub>2</sub> O <sub>4</sub>	Sol-gel	Nanoparticles (10.4 nm)	LPG	RT	2000	2.5 b	60 s /300 s	-	[161]
Ni <sub>0.6</sub> Zn <sub>0.4</sub> Fe <sub>2</sub> O <sub>4</sub>	Co-precipitation	Nanoparticles (55 nm)	Cl <sub>2</sub>	177	500	0.66 c	30 s/60 s	-	[90]
Ni <sub>0.6</sub> Zn <sub>0.4</sub> Fe <sub>2</sub> O <sub>4</sub>	Microwave	Nanoparticles (25 nm)	Acetone	250	1000	0.72 c	90 s /720 s	-	[175]
Co <sub>0.5</sub> Ni <sub>0.5</sub> Fe <sub>2</sub> O <sub>4</sub>	Co-precipitation	Nanoparticles	CO	350	1000	0.25 c	-	-	[176]
Mn-CoFe <sub>2</sub> O <sub>4</sub>	Auto combustion	Nanoparticles (3 nm)	LPG	300	1000	0.19 c	40 s/50 s	-	[177]
1 wt% Cu:NiFe <sub>2</sub> O <sub>4</sub>	Spray pyrolysis deposition	Nanoparticles (40–46 nm)	Ethanol	325	5	3.2 c	-	-	[178]
BaCa <sub>2</sub> Fe <sub>16</sub> O <sub>27</sub>	Sol-gel	Nanoparticles	Ethanol	300	100	0.53 c	-	-	[179]
Mn-CuFe <sub>2</sub> O <sub>4</sub>	Auto-combustion	Nanoparticles (9 nm)	LPG	300	1000	0.28 c	10–20 s/-	-	[180]
Ni-CdFe <sub>2</sub> O <sub>4</sub>	Sol-gel auto combustion	Grain size (300 nm)	H <sub>2</sub> O	RT	-	0.99 c	30 s/45 s	-	[28]
Ni <sub>0.8</sub> Co <sub>0.2</sub> Fe <sub>2</sub> O <sub>4</sub>	Evaporation	Nanoparticles (10 nm)	LPG	250	1000	0.7 d	40 s/60 s	-	[181]
Sn <sub>0.2</sub> Ni <sub>0.8</sub> Fe <sub>2</sub> O <sub>4</sub>	Co-precipitation	Nanoparticles (35 nm)	SF <sub>6</sub>	RT	80	0.68 c	-	-	[182]
Li-CuFe <sub>2</sub> O <sub>4</sub>	Co-precipitation	Nanoparticle (<100 nm)	LPG	RT	4 vol%	1.82 b	-	-	[183]
In-CuFe <sub>2</sub> O <sub>4</sub>	Co-precipitation	Nanoparticles	LPG	RT	4 vol%	0.37 c	229 s/-	-	[184]
Ni <sub>0.1</sub> Co <sub>0.9</sub> Fe <sub>2</sub> O <sub>4</sub>	Sol-gel auto combustion	Microcubes	Acetone	240	200	1.67 b	-	-	[164]
CoNiFe <sub>2</sub> O <sub>4</sub>	Co-precipitation	Nanoparticles (28 nm)	LPG	50	500	0.66 c	-	-	[185]
Bi-CoFe <sub>2</sub> O <sub>4</sub>	Sol-gel	Nanoparticles (5–90 nm)	NO <sub>2</sub>	230	100	0.19 c	31 s/29 s	25 ppm	[186]
Cu-ZnFe <sub>2</sub> O <sub>4</sub>	Hydrothermal	Spherical nanoparticles (50 nm)	H <sub>2</sub> S	RT	5	37.9 a	10 s /210 s	-	[187]
Ni <sub>0.33</sub> Co <sub>0.67</sub> Fe <sub>2</sub> O <sub>4</sub>	Solvothermal	Mesoporous microspheres	Toluene	300	10	35 a	10 s/51 s	-	[188]
Zn <sub>0.5</sub> Cu <sub>0.5</sub> Fe <sub>2</sub> O <sub>4</sub>	Sol-gel auto-combustion	Nanoparticles (30–70 nm)	H <sub>2</sub> S	80	1000	0.71 c	170 s/-	-	[189]

Table 5. Cont.

Materials	Synthesis	Morphology	Gas	O.T. (°C)	Conc. (ppm)	Response	$t_{res}/t_{rec}$	LOD	Refs.
$Mn_{0.7}Zn_{0.3}Fe_2O_4$	Co-precipitation	Nanoparticles (5.5–10.5 nm)	LPG	250	1000	1.88 a	40 s/20 s	-	[190]
$Sn_{0.2}Cu_{0.8}Fe_2O_4$	Co-precipitation	Nanoparticles (37 nm)	LPG	RT	2 vol%	0.78 c	32 s/111 s	-	[191]
$Co_{0.25}Ba_{0.75}Fe_2O_4$	Co-precipitation	Nanoparticles (16.5 nm)	$NO_2$	RT	220	0.79 c	-	-	[192]
$Zn_{0.5}Mg_{0.5}Fe_2O_4$	Co-precipitation	Nanoparticles (50–150 nm)	$H_2S$	400	10	0.11 d	16 s/-	-	[193]
$Ni_{0.7}Zn_{0.3}Fe_2O_4$	Co-precipitation and sintering	Nanoparticles	LPG	200	1000	0.75 c	40 s/30 s	-	[163]
$Cu_{0.75}Zn_{0.25}Fe_2O_4$	Solvothermal	Hollow micro-nanospheres	Acetone	125	0.8	2.37 a	66 s/138 s	-	[40]
$(Cu,Zn)Fe_2O_4$	Solvothermal	Nano-microspheres	TEA	165	50	6.77 a	58 s/136 s	-	[194]
$CuZnFe_2O_4$	Electrospinning	Nanofibers	$H_2$	250	500	5.9 a	6 s/75 s	-	[195]
5 wt% Ni-doped $MnFe_2O_4$	Co-precipitation	Nanoparticles (35 nm)	$NH_3$	RT	200	0.51 c	17 s/13 s	-	[196]
$Cu_{0.1}Zn_{0.9}Fe_2O_4$	Spray pyrolysis	Thin Films	$SO_2$	120	200	0.474 c	-	-	[197]
$Co_{0.87}Ni_{0.13}Fe_2O_4$	Co-precipitation	Nanoparticles	LPG	400	5000	0.97 c	11 s/110 s	-	[198]
$Ni_{0.4}Mn_{0.3}Zn_{0.3}Fe_2O_4$	Precursor combustion	Thick film	$Cl_2$	100	300	2.12 d	10 s/15 s	-	[199]
$Sr_{0.2}Ni_{0.8}Fe_2O_4$	Sol-gel spin coating	Nanoparticles (20–50 nm)	LPG	200	2000	0.28 c	78 s/66 s	-	[200]

a Response is defined as  $R_a/R_g$ ; b Response is defined as  $R_g/R_a$ ; c Response is defined as  $\Delta R/R_a$ ; d Response is defined as  $\Delta R/R_g$ .

Dalawai et al. [90] prepared  $Ni_xZn_{1-x}Fe_2O_4$  ( $x = 0, 0.2, 0.4, 0.6, 0.8,$  and  $1.0$ ) using the oxalic acid co-precipitation method. With the increase in nickel content in Ni-Zn ferrite, the bond length (A-O) and ionic radius ( $r_A$ ) at site A decreased (Figure 7d), while the bond length (B-O) and ionic radius ( $r_B$ ) at site B remained unchanged. Infrared spectroscopy revealed two major absorption bands near  $400$  and  $600\text{ cm}^{-1}$ , corresponding to tetrahedral and octahedral locations, respectively. Compared with LPG and  $Cl_2$ ,  $ZnFe_2O_4$  thick films showed a higher sensitivity to ethanol (82%) (Figure 7h), better response time (30 s), and better recovery time (90 s).  $NiFe_2O_4$  thick film has a good sensitivity (63%), good response (30 s) and good recovery time (70 s) to LPG. Compared with LPG,  $Ni_{0.6}Zn_{0.4}Fe_2O_4$  displayed a higher sensitivity towards  $Cl_2$  and ethanol gases. Zhang et al. [187] conducted a study where they synthesized Cu-doped  $ZnFe_2O_4$  nanoparticles (Cu-ZFNPs) using a hydrothermal method. Interestingly, the addition of copper did not significantly alter the size of the nanoparticles, which remained around 50 nm for both the pure and Cu-doped ZFNPs. Figure 7j shows the XRD patterns of the pure ZFNPs and Cu-ZFNPs with different Cu concentrations. However, the gas-sensing performance of the nanoparticles was notably affected by copper doping. The Cu-ZFNPs exhibited a superior performance in detecting  $H_2S$  gas compared with the pure ZFNPs, particularly at lower temperatures. This proves that the introduction of copper into the  $ZnFe_2O_4$  nanoparticles improved their sensitivity to  $H_2S$  gas, highlighting the effectiveness of element doping in optimizing the properties of spinel ferrite materials. The best gas-sensing performance was achieved with Cu-ZFNPs containing an appropriate concentration of copper. These nanoparticles demonstrated a maximum response of 37.9 to 5 ppm  $H_2S$  at room temperature (Figure 7k). The sensor also exhibited rapid response and recovery times, taking only 10 s to respond to the presence of  $H_2S$  and 210 s to recover after the gas was removed.



**Figure 7.** (a) FESEM image of embedded  $\text{Mg}_{0.5}\text{Zn}_{0.5}\text{Fe}_2\text{O}_4$  nanotubes. (b) Resistance transients of embedded  $\text{Mg}_{0.5}\text{Zn}_{0.5}\text{Fe}_2\text{O}_4$  nanotubes towards  $\text{H}_2$  (~1660 ppm). (c) Dynamic curve of the resistance embedded  $\text{Mg}_{0.5}\text{Zn}_{0.5}\text{Fe}_2\text{O}_4$  nanotube sensors to the 10–1660 ppm range of  $\text{H}_2$  at ~350 °C. (d) Variations of the lattice constant with Ni content of  $\text{Ni}_x\text{Zn}_{1-x}\text{Fe}_2\text{O}_4$  system. (e) SEM image of the isolated  $\text{Mg}_{0.5}\text{Zn}_{0.5}\text{Fe}_2\text{O}_4$  nanotubes. (f) Resistance transient of isolated  $\text{Mg}_{0.5}\text{Zn}_{0.5}\text{Fe}_2\text{O}_4$  nanotubes to 1660 ppm  $\text{H}_2$ . (g) Dynamic curve of the resistance isolated  $\text{Mg}_{0.5}\text{Zn}_{0.5}\text{Fe}_2\text{O}_4$  nanotube sensors to the 10–1660 ppm range of  $\text{H}_2$  at 350 °C. (h) Response of sensors based on  $\text{Ni}_x\text{Zn}_{1-x}\text{Fe}_2\text{O}_4$  ( $x = 0, 0.6, 1.0$ ) to LPG gas at different operating temperatures. (i) The TEM images and SAED pattern of  $\text{Ni}_{0.7-x}\text{Mn}_x\text{Zn}_{0.3}\text{Fe}_2\text{O}_4$ . (j) Small-range XRD patterns of the pure ZFNPs and Cu-ZFNPs with different Cu concentrations. (k) The variation in sensitivity with operating temperatures of pure ZFNPs and Cu-ZFNPs for 5 ppm  $\text{H}_2\text{S}$ . (l) The response–concentration plots of  $\text{Ni}_{0.4}\text{Mn}_{0.3}\text{Zn}_{0.3}\text{Fe}_2\text{O}_4$  towards different test gases. (a–c,e–g) Reproduced with permission [155], copyright 2013, Elsevier B.V. (d,h) Reproduced with permission [90], copyright 2015, Springer Nature. (i,l) Reproduced with permission [199], copyright 2022, Elsevier B.V. (j,k) Reproduced with permission [187], copyright 2019, Elsevier B.V.

Using the co-precipitation method, Mondal et al. [201] conducted a study where they synthesized  $\text{Cu}_{0.5}\text{Ni}_{0.25}\text{Zn}_{0.25}\text{Fe}_2\text{O}_4$  nanoparticles and  $\text{Cu}_{0.25}\text{Ni}_{0.5}\text{Zn}_{0.25}\text{Fe}_2\text{O}_4$  nanoparticles. At ambient room temperature, both sensors demonstrated exceptional responsiveness to acetone and ethanol. The inclusion of Cu in  $\text{Cu}_{0.5}\text{Ni}_{0.25}\text{Zn}_{0.25}\text{Fe}_2\text{O}_4$  resulted in a noteworthy enhancement in sensitivity to acetone, reaching an impressive 77%, while the introduction of Ni in  $\text{Cu}_{0.25}\text{Ni}_{0.5}\text{Zn}_{0.25}\text{Fe}_2\text{O}_4$  improved the sensitivity to ethanol to 75%. These findings suggest that the addition of specific transition metal elements, such as copper and nickel, enhances the gas-sensing properties of the ferrite nanoparticles, making them promising materials for the detection of acetone and ethanol gases. Gauns et al. [199] fabricated a thick film of  $\text{Ni}_{0.4}\text{Mn}_{0.3}\text{Zn}_{0.3}\text{Fe}_2\text{O}_4$  (Figure 7i) on a glass substrate for the detection of  $\text{Cl}_2$ . The thick ferrite film composed of  $x = 0.3$  showed a high selective response to  $\text{Cl}_2$  gas at 100 °C. For 300 ppm of  $\text{Cl}_2$  gas, the response was 212% (Figure 7l). The reaction time was less than 10 s and the recovery time was less than 15 s.

**Table 6.** Summary of the reported spinel ferrite B-site doping-based gas sensors.

Materials	Synthesis	Morphology	Gas	O.T. (°C)	Conc. (ppm)	Response	t <sub>res</sub> /t <sub>rec</sub>	LOD	Refs.
MgFe <sub>1.98</sub> Mo <sub>0.02</sub> O <sub>4</sub>	Auto-combustion	Nanoparticles (310 nm)	Acetone	380	500	0.65 c	180 s/	-	[165]
Li <sub>0.5</sub> Fe <sub>2.45</sub> Sm <sub>0.05</sub> O <sub>4</sub>	Sol-gel self-combustion	Nanoparticles (200 nm)	Methanol	340	200	0.86 c	-	-	[202]
CuCe <sub>0.04</sub> Fe <sub>1.96</sub> O <sub>4</sub>	Molten-salt	Nanoparticles (10 nm)	LPG	275	2000	0.86 c	5 s/68 s	-	[203]
CoFe <sub>1.96</sub> Ce <sub>0.04</sub> O <sub>4</sub>	Molten-salt	Nanoparticles (20 nm)	Acetone	225	100	1.77 b	45 s/70 s	-	[204]
NiLaFe <sub>2</sub> O <sub>4</sub>	Co-precipitation	Nanoparticles (9.26 nm)	NH <sub>3</sub>	35	50	786 a	163/64 s	-	[205]
Bi-Co ferrite	Sol-gel	Nanoparticles (6.5–89 nm)	NO <sub>2</sub>	230	200	0.34 c	31/29 s	-	[186]
MgFe <sub>1.88</sub> Ce <sub>0.12</sub> O <sub>4</sub>	Glycine combustion	Thick film	Acetone	325	1000	0.94 c	-	-	[156]
CoSm <sub>0.1</sub> Fe <sub>1.9</sub> O <sub>4</sub>	Solvothermal	Nanoparticles	LPG	225	10,000	846 c	-	-	[206]
MgCe <sub>0.2</sub> Fe <sub>1.8</sub> O <sub>4</sub>	Glycol-thermal	Nanoparticles	Acetone	225	100	500 a	-	-	[207]
1.5% Sn-BiFe <sub>2</sub> O <sub>4</sub>	Sol-gel	Nanoparticles	HCHO	280	1	3.05 b	2.7 s/25 s	100 ppb	[208]
1 wt.% La-CoFe <sub>2</sub> O <sub>4</sub>	Spray-deposited	Thin films	NH <sub>3</sub>	RT	200	0.99 c	44/53 s	-	[209]

a Response is defined as  $R_a/R_g$ ; b Response is defined as  $R_g/R_a$ ; c Response is defined as  $\Delta R/R_a$ .

#### 4.2. B Site Doping

Spinel ferrite, represented by the formula  $(M^{2+})(Fe^{3+})_2O_4$ , adopts a face-centered cubic crystal structure. It can be classified into three types: normal spinel, inverse spinel, and mixed spinel. The arrangement of divalent and trivalent metal ions in tetrahedral and octahedral sites within the crystal lattice determines the spinel classification [210]. The introduction of rare earth ions (RE) as substitutions for a small portion of iron can have significant effects on the electrical and magnetic properties of spinel ferrite. For example, the introduction of Ce, which involves the coupling of 3d–4f interactions, leads to changes in the electrical and magnetic behaviors. Furthermore, Ce substitution can also impact the distribution of cations within the spinel lattice, resulting in alterations to its structural, magnetic, physicochemical, and electrical properties [211]. Other rare earth elements, when substituted into the spinel structure, can similarly induce changes in structural, magnetic, and electrical properties, although the specific effects may differ from those observed with Ce<sup>3+</sup> [212]. Mkwae et al. [207] conducted a study where they prepared MgCe<sub>x</sub>Fe<sub>2–x</sub>O<sub>4</sub> (0 < x < 0.2) nanoparticles (Figure 8a). X-ray diffraction (Figure 8b) analysis confirmed that the sample containing a lower concentration of Ce formed a pure cubic spinel phase. However, with higher Ce doping (x > 0.2), the formation of a secondary phase was observed. The grain size of the compounds ranged from 2.2 nm to 15.3 nm. As the Ce concentration increased, the spin state of <sup>57</sup>Fe Mossbauer transitioned from an ordered state to a paramagnetic state. The MgCe<sub>x</sub>Fe<sub>2–x</sub>O<sub>4</sub> nano-ferrite exhibited a high sensitivity and selectivity towards the 100 ppm acetone vapors, with a response concentration exceeding 500 at 225 °C (Figure 8c). The sensor also demonstrated excellent repeatability, reversibility, and stability over a period of 120 days.

**Table 7.** Summary of the reported spinel ferrite AB site doping-based gas sensors.

Materials	Synthesis	Morphology	Gas	O.T. (°C)	Conc. (ppm)	Response	t <sub>res</sub> /t <sub>rec</sub>	LOD	Refs.
Mg <sub>0.9</sub> Sn <sub>0.1</sub> Mo <sub>0.02</sub> Fe <sub>1.98</sub> O <sub>4</sub>	Auto-combustion	Nanoparticles	ethanol	380	500	0.64 c	-	-	[165]
Ni <sub>0.99</sub> Co <sub>0.01</sub> Mn <sub>0.02</sub> Fe <sub>1.98</sub> O <sub>4</sub>	Self-combustion	Nanoparticles	acetone	215	500	4.5 c	-	-	[213]
Co <sub>0.7</sub> Zn <sub>0.3</sub> Fe <sub>1.975</sub> Gd <sub>0.025</sub> O <sub>4</sub>	Sol-gel	Nanoparticles	H <sub>2</sub> S	RT	50	0.4 d	11 s/5 s	-	[157]
Co <sub>0.7</sub> Zn <sub>0.3</sub> La <sub>0.1</sub> Fe <sub>1.9</sub> O <sub>4</sub>	Sol-gel	Nanoparticles (20 nm)	NH <sub>3</sub>	RT	200	0.87 c	116 s/45 s	-	[214]
Zn <sub>0.7</sub> Mn <sub>0.3</sub> Gd <sub>0.025</sub> Fe <sub>1.975</sub> O <sub>4</sub>	Co-precipitation	Nanoparticles (20–30 nm)	acetone	RT	saturated	0.53 c	36 s/56 s	-	[215]

c Response is defined as  $\Delta R/R_a$ ; d Response is defined as  $\Delta R/R_g$ .

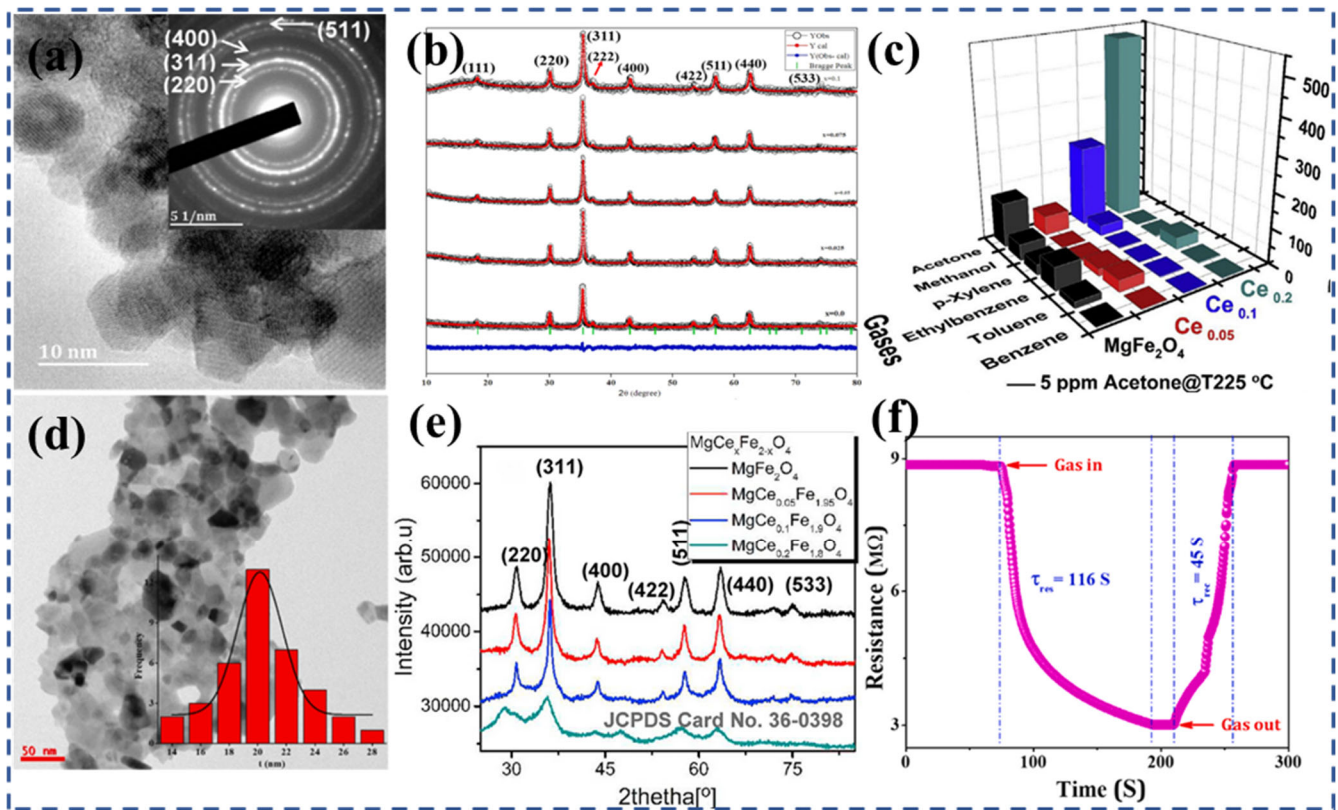


**Figure 8.** (a) HRTEM images of  $\text{MgCe}_{0.2}\text{Fe}_{1.8}\text{O}_4$ . (b) The XRD patterns of  $\text{MgCe}_x\text{Fe}_{2-x}\text{O}_4$ . (c) Responses of  $\text{MgCe}_x\text{Fe}_{2-x}\text{O}_4$  nanoferrites ( $x = 0, 0.05, 0.1, \text{ and } 0.2$ ) to various gas with 100 ppm. (d) TEM image of CZLF ferrite with  $x = 0.1$ . (e) XRD pattern of  $\text{La}^{3+}$ -CZLF powders. (f) The resistance plot of a sensor based on  $\text{Co}_{0.7}\text{Zn}_{0.3}\text{La}_{0.1}\text{Fe}_{1.9}\text{O}_4$ . (a–c) Reproduced with permission [207], copyright 2020, Elsevier B.V. (d–f) Reproduced with permission [214], copyright 2022, Elsevier B.V.

#### 4.3. AB Site Doping

Rezlescu et al. [165] conducted a study where they prepared  $\text{Mg}_{1-x}\text{Sn}_x\text{Mo}_y\text{Fe}_{2-y}\text{O}_4$  ( $x = 0, 0.1, \text{ and } y = 0, 0.02$ ) ferrites using metal nitrate as the raw materials using the self-combustion method. The introduction of Sn and Mo ions induced structural changes in terms of grain size and porosity. Specifically, the sample containing tin exhibited the highest porosity, with particle sizes around 100 nm. When Sn ions partially replaced Mg in  $\text{MgFe}_2\text{O}_4$  ferrite, the resistivity of the material improved by approximately two orders of magnitude. The samples were subjected to testing to evaluate their sensing capabilities towards reducing gases, specifically ethanol and acetone. The gas sensitivity was found to depend largely on the type of substituted ion and the specific gas being detected. Overall, all ferrites exhibited a higher sensitivity to acetone compared with ethanol. Among all of the ferrites tested,  $\text{Mg}_{0.9}\text{Sn}_{0.1}\text{Fe}_2\text{O}_4$  demonstrated the highest sensitivity to acetone. These findings highlight the potential of  $\text{Mg}_{0.9}\text{Sn}_{0.1}\text{Fe}_2\text{O}_4$  ferrite as a highly sensitive material for the detection of acetone gas. Mugutkar et al. [214] synthesized  $\text{Co}_{0.7}\text{Zn}_{0.3}\text{La}_x\text{Fe}_{2-2x}\text{O}_4$  ( $x = 0\text{--}0.1$ ) nanoparticles (Figure 8d) using the sol–gel method. The XRD pattern (Figure 8e) of ferrite powder was refined using the Rietveld technique, and it was found that a single-phase spinel structure was formed. Through the analysis of the gas-sensitive properties, the response of the  $\text{Co}_{0.7}\text{Zn}_{0.3}\text{La}_x\text{Fe}_{2-2x}\text{O}_4$  sensor was 0.87 towards 200 ppm  $\text{NH}_3$  at RT, with a short response and recovery time of 116 and 45 s (Figure 8f), respectively.

**Table 8.** Summary of the reported noble metal-decorated spinel-ferrite-based gas sensors.

Materials	Synthesis	Morphology	Gas	O.T. (°C)	Conc. (ppm)	Response	$t_{res}/t_{rec}$	LOD	Refs.
Au/NiFe <sub>2</sub> O <sub>4</sub>	Solid-state reaction	Nanoparticles	H <sub>2</sub> S	300	5	35.8 b	-	-	[216]
Au/NiFe <sub>2</sub> O <sub>4</sub>	Co-precipitation	Nanoparticles	C <sub>6</sub> H <sub>5</sub> CH <sub>3</sub>	350	1000	15.8 b	-	-	[217]
Au/ZnFe <sub>2</sub> O <sub>4</sub>	Solvothermal	Yolk-shell Microspheres	H <sub>2</sub> S	RT	200	65.9 a	46/629 s	-	[218]
ZnO/ZnFe <sub>2</sub> O <sub>4</sub> /Au	Electrospinning, atomic layer deposition and solution reaction	Hollow meshes	Acetone	225	100	30.3 a	1/59 s	-	[219]
Au/ZnFe <sub>2</sub> O <sub>4</sub>	Solution-phase deposition	Yolk-shell Spheres	C <sub>6</sub> H <sub>5</sub> Cl	150	10	90.9 a	-	100 ppb	[220]
Au/ZnFe <sub>2</sub> O <sub>4</sub>	Hydrothermal	Nanoparticles	Acetone	120	40	26 a	4/69 s	-	[221]
ZnO/ZnFe <sub>2</sub> O <sub>4</sub> /Au	Hydrothermal and Co-precipitation	Yolk-shell microspheres assembled from nanosheets	Acetone	206	100	18.18 a	4/23 s	0.7 ppm	[222]
Ag/NiFe <sub>2</sub> O <sub>4</sub>	Solid-state reaction	Nanoparticles	Acetone	-	1000	43 a	1/10 s	-	[223]
Ag/ZnFe <sub>2</sub> O <sub>4</sub>	Hydrothermal	Hollow sphere	Acetone	175	100	33.8 a	17/148 s	-	[224]
Pd/Co <sub>0.8</sub> Ni <sub>0.2</sub> Fe <sub>2</sub> O <sub>4</sub>	Sol-gel	Nanoparticles	NH <sub>3</sub>	210	200	0.91 c	20 s/-	-	[225]
Pd/MgFe <sub>2</sub> O <sub>4</sub>	Molten salt	Nanoparticles (15–20 nm)	LPG	200	200	432 a	-	-	[226]
Pd/NiFe <sub>2</sub> O <sub>4</sub>	Spray pyrolysis	Nanoparticles	Ethanol	325	15	4.15 c	3/13 s	-	[158]
Pd/NiFe <sub>2</sub> O <sub>4</sub>	Spray pyrolysis	Thin films	Cl <sub>2</sub>	375	5	6.9 d	-	-	[227]
Pd/Co <sub>0.55</sub> Zn <sub>0.45</sub> Fe <sub>2</sub> O <sub>4</sub>	Hydrothermal	Nanoparticles	H <sub>2</sub>	275	5000	0.99 c	25/3 s	-	[228]
Pt/CuFe <sub>2</sub> O <sub>4</sub>	Electrospinning	Nanotubes	Acetone	300	100	16.5 a	-	-	[229]
Ru/NiFe <sub>2</sub> O <sub>4</sub>	Co-precipitation	Nanoparticles (0.48 nm)	H <sub>2</sub> S	100	50	1.39 b	-	-	[230]

a Response is defined as  $R_a/R_g$ ; b Response is defined as  $R_g/R_a$ ; c Response is defined as  $\Delta R/R_a$ ; d Response is defined as  $\Delta R/R_g$ .

#### 4.4. Noble Metal Doping

Currently, the noble metals widely utilized in gas-sensing applications encompass Pt, Pd, Au, Ag, and Ru, as well as their bimetallic composites. The enhancement of gas-sensing performance can be attributed to two key mechanisms: the electronic sensitization effect achieved by constructing metal–semiconductor contact [231] and the chemical sensitization effect stemming from the spillover phenomenon [232]. These mechanisms work in tandem, facilitating rapid interaction between noble-metal-decorated semiconductor spinel ferrite and target gases, while also effectively lowering the work temperatures by reducing the activation energy required for gas sensing.

**Table 9.** Summary of the reported other element doping spinel-ferrite-based gas sensors.

Materials	Synthesis	Morphology	Gas	O.T. (°C)	Conc. (ppm)	Response	$t_{res}/t_{rec}$	LOD	Refs.
V-ZnFe <sub>2</sub> O <sub>4</sub>	Citrate pyrolysis	Nanoparticles	Acetone	300	100	23 a	-	-	[233]
Zr-CaFe <sub>2</sub> O <sub>4</sub>	Solid-state reaction	Nanoparticles	CO <sub>2</sub>	350	5000	3.3 a	-	-	[234]
In-CuFe <sub>2</sub> O <sub>4</sub>	Co-precipitation	Thin film	LPG	25	5 vol%	0.3715 c	229 s/-	-	[184]
Sb-ZnFe <sub>2</sub> O <sub>4</sub>	Spray pyrolysis	Microporous spheres	n-butanol	250	100	33.5 a	4 s/250 s	-	[235]
V-NiFe <sub>2</sub> O <sub>4</sub>	Co-precipitation	Nanoparticles	NO	RT	200	43 a	5 s/-	-	[236]
W-CoFe <sub>2</sub> O <sub>4</sub>	Sol-gel	Nanoparticles	Acetone	350	2000	1.45 c	-	-	[237]

a Response is defined as  $R_a/R_g$ ; c Response is defined as  $\Delta R/R_a$ .

Li et al. [220] conducted a study wherein they utilized the liquid phase deposition precipitation method to prepare a ZnFe<sub>2</sub>O<sub>4</sub> egg yolk–shell ball structure consisting of ultra-thin nanosheets and ultra-small nanoparticles. The surface of this structure was adorned with nanoscale gold particles, each with a diameter ranging from 1 to 2 nm. The experimental results revealed a significant four-fold increase in response ( $R_{air}/R_{gas} = 90.9$ ) for the Au/ZnFe<sub>2</sub>O<sub>4</sub> sensor when exposed to 10 ppm chlorobenzene at 150 °C (Figure 9b),

compared with the original ZFO sensor. Furthermore, the Au/ZnFe<sub>2</sub>O<sub>4</sub> sensor demonstrated excellent selectivity and exhibited the potential for application in chlorobenzene monitoring. The introduction of nanoscale gold particles onto the surface of the ZFO yolk–shell balls (Figure 9a) resulted in electronic and chemical sensitization effects, thereby enhancing the chlorobenzene sensing performance of the ZnFe<sub>2</sub>O<sub>4</sub> yolk–shell balls. Additionally, density functional theory (DFT) calculations were employed to corroborate the findings, confirming that the presence of gold nanoparticles on the surface of ZnFe<sub>2</sub>O<sub>4</sub> increased electron density, exhibited a higher adsorption energy, and facilitated net charge transfer. These factors collectively contributed to the heightened sensing response of the sensor towards chlorobenzene. Zhang et al. [224] employed a hydrothermal method to introduce Ag into ZnFe<sub>2</sub>O<sub>4</sub> hollow structures (Figure 9c) composed of stacked nanosheets. The addition of Ag altered the surface structure, but did not significantly affect the size of the hollow structures. At a temperature of 175 °C, the sensor based on 0.25 wt.% Ag-doped ZnFe<sub>2</sub>O<sub>4</sub> (Ag/ZnFe<sub>2</sub>O<sub>4</sub>) exhibited a superior sensing performance compared with the pure ZnFe<sub>2</sub>O<sub>4</sub> sensor (Figure 9d). This improvement in performance can be attributed to the suitable hollow structure and the activation effect of Ag. Ag/ZnFe<sub>2</sub>O<sub>4</sub> sensors show promising potential for detecting low concentrations of acetone in the parts per million range. Additionally, these sensors demonstrate good gas selectivity to acetone and minimal influence from humidity. However, further research and improvement are needed to address the long-term stability of Ag/ZnFe<sub>2</sub>O<sub>4</sub> sensors.

Li et al. [219] successfully synthesized ZnO/ZnFe<sub>2</sub>O<sub>4</sub>/Au heterostructures (Figure 9e,f) with a porous mesh structure using a three-step method (a combination of electrospinning, atomic layer deposition, and solution reaction). The resulting ZnO/ZnFe<sub>2</sub>O<sub>4</sub>/Au structures exhibited a porous mesh-like morphology. The composite structure comprised of a uniform ZnO nanotube skeleton measuring 50 nm, ultra-thin ZnFe<sub>2</sub>O<sub>4</sub> nanosheets with a thickness of 10 nm, and well-dispersed Au nanoparticles. It had the characteristics of a large specific surface area, porous structure, ultra-thin thickness and high catalytic activity. The gas-sensing results show that the sensor based on the ZnO/ZnFe<sub>2</sub>O<sub>4</sub>/Au nanonet had the highest sensing response (30.3), a significantly enhanced selectivity, and a faster response/recovery speed (1 s/59 s). The response of ZnO/ZnFe<sub>2</sub>O<sub>4</sub>/Au to acetone was about three times higher than that of ZnO/ZnFe<sub>2</sub>O<sub>4</sub> composites and 5.5 times higher than that of the original ZnO (Figure 9g). The enhanced sensing performance was mainly due to the increase in the surface active sites of AuNPs, the obvious resistance modulation effect, and the excellent sensitization ability.

#### 4.5. Other Element Doping

Doping refers to the process of introducing impurity atoms into a material, which can have various effects on the lattice and structure of the host material. One effect of doping is the alteration of the lattice constant, which is the spacing between the atoms in the crystal lattice. The presence of dopant atoms can disrupt the regular arrangement of atoms in the lattice, leading to changes in the lattice constant. Furthermore, doping can also introduce structural defects into the matrix material. These defects can include vacancies, where atoms are missing from lattice sites, or interstitials, where dopant atoms occupy spaces between lattice sites [238]. These defects can affect the overall structure and properties of the material, such as its electrical conductivity or optical properties. In addition to changing the lattice constant and introducing structural defects, doping can also regulate the charge exchange behavior of the material [239]. Doped ions often have multiple valence states, meaning they can exist in different charge states depending on the electron configuration [184]. When doped ions occupy equivalent lattice locations, they can undergo charge exchange with neighboring ions, leading to changes in the electronic properties of the material. This charge exchange behavior can influence the material's conductivity, magnetism, or other electronic properties [236,237]. Overall, doping is a versatile technique that can be used to modify the lattice, introduce defects, and regulate the charge exchange behavior in materials, thereby tailoring their properties for specific applications.

Jiang et al. [233] conducted a study where they prepared  $\text{ZnFe}_2\text{O}_4$  nanoparticles and vanadium (V)-doped  $\text{ZnFe}_2\text{O}_4$  nanoparticles using citrate pyrolysis. Interestingly, the particle size of the spherical particles remained unaffected by the V content added. However, as the V content increased, the resistance of the thick film based on  $\text{ZnFe}_2\text{O}_4$  decreased. The study also revealed that the addition of V had varying effects on the sensitivity to different VOCs (Figure 9h). The sensitivity to ethanol and acetone was significantly reduced due to the addition of V. However, at higher temperatures, the addition of V notably improved the sensitivity to benzene, toluene, and xylene. These findings suggest that V doping in  $\text{ZnFe}_2\text{O}_4$  nanoparticles can have a selective impact on the sensitivity to different VOCs. While the sensitivity to ethanol and acetone decreased, the sensitivity to benzene, toluene, and xylene improved, particularly at elevated temperatures.

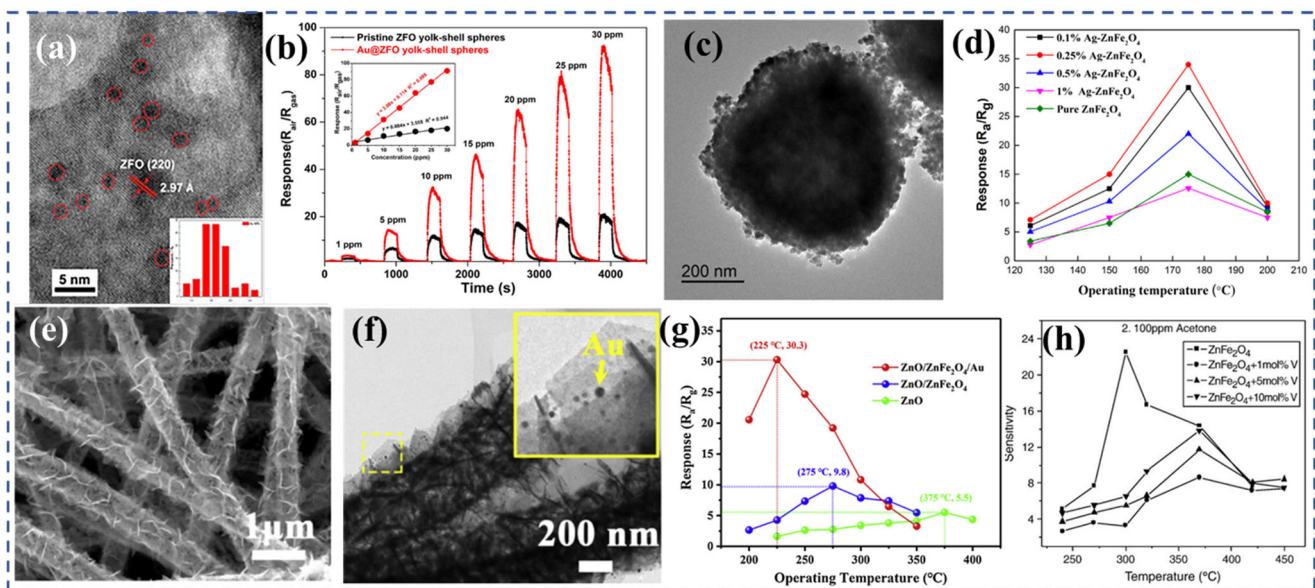


**Figure 9.** (a) HRTEM images of the Au nanoparticles/ZFO yolk-shell spheres and the inset is the size distribution of Au nanoparticles (marked with red circle). (b) Dynamic curve of the gas sensor based on the ZFO and Au/ZFO sphere to CB with different concentrations at 150 °C. (c) TEM images of 0.25 wt.% Ag/ZnFe<sub>2</sub>O<sub>4</sub>. (d) The effect of operating temperatures of the Ag/ZnFe<sub>2</sub>O<sub>4</sub>-sensor on the various gas responses of the sensors to 100 ppm acetone vapor at 125–200 °C. (e) SEM and (f) TEM images of ZnO/ZnFe<sub>2</sub>O<sub>4</sub>/Au ternary heterostructure. (g) Responses–temperature characteristics of the ZnO/ZnFe<sub>2</sub>O<sub>4</sub>/Au sensors to 100 ppm acetone. (h) The responses of sensors to ZnFe<sub>2</sub>O<sub>4</sub> thick films vs. the content of V doping. (a,b) Reproduced with permission [220], copyright 2019, American Chemical Society. (c,d) Reproduced with permission [224], copyright 2018, Elsevier B.V. (e–g) Reproduced with permission [219], copyright 2019, Elsevier B.V. (h) Reproduced with permission [233], copyright 2006, Elsevier B.V.

## 5. Heterostructure

In Sections 3 and 4, it has been discussed how the gas-sensitive performance of spinel ferrite sensors can be enhanced through the manipulation of their morphology or the introduction of doping elements. However, to achieve the desired properties, researchers have explored the development of spinel ferrite composites, which find more extensive applications in the fields of photocatalysis and sensing. Consequently, the objective of this section is to provide a review of the latest research on spinel ferrite composites and to present the impact of these two types of composites on the gas-sensitive properties (Tables 10–12). The development of spinel ferrite composites has gained significant attention due to their potential to synergistically enhance the gas-sensitive performance. These composites often involve combining spinel ferrite with other materials such as metal

oxides, carbon-based materials, or polymers. The unique properties of these composite materials can be leveraged to improve the gas-sensing properties of spinel ferrite sensors. For example, metal-oxide-based spinel ferrite composites have demonstrated an improved gas-sensing performance due to the enhanced specific surface area and increased active sites provided by the metal oxide component. The combination of spinel ferrite with carbon-based materials, such as graphene or carbon nanotubes, can enhance the electrical conductivity and provide additional adsorption sites, leading to enhanced gas-sensing capabilities. In summary, the development of spinel ferrite composites has opened up new avenues for enhancing the gas-sensitive properties of spinel ferrite sensors. These composites, whether metal-oxide-based, carbon-based, or incorporating polymers, offer unique advantages that can be leveraged to achieve an improved gas-sensing performance.

**Table 10.** Summary of the reported other MOSs/spinel-ferrite-based gas sensors.

Materials	Synthesis	Morphology	Gas	O.T. (°C)	Conc. (ppm)	Response	$t_{res}/t_{rec}$	LOD	Refs.
CdO/Cd <sub>0.1</sub> Ni <sub>0.45</sub> Mn <sub>0.45</sub> Fe <sub>2</sub> O <sub>4</sub>	Co-precipitation	Nanoparticles	DMF	250	200	0.85 d	28 s/41 s	-	[240]
Co <sub>3</sub> O <sub>4</sub> /CoFe <sub>2</sub> O <sub>4</sub>	Metal-organic framework	Double-shelled nanotubes	HCHO	139	10	12.7 b	4 s/9 s	300 ppb	[241]
Co <sub>3</sub> O <sub>4</sub> /CoFe <sub>2</sub> O <sub>4</sub>	Calcination	Core-shell structure	NH <sub>3</sub>	220	100	35 a	15 s/21 s	-	[242]
CuO/CuFe <sub>2</sub> O <sub>4</sub>	Frequency sputtering	Thick film	CO <sub>2</sub>	250	5000	0.17 4 c	-	-	[243]
CuO/CuFe <sub>2</sub> O <sub>4</sub>	Calcination	Core-shell	H <sub>2</sub> S	250	2	10.8 a	-	-	[244]
CuO/CuFe <sub>2</sub> O <sub>4</sub>	Frequency sputtering	Thick film	CO <sub>2</sub>	250	5000	0.40 c	-	-	[245]
CuO/CuFe <sub>2</sub> O <sub>4</sub>	Co-precipitation	Nanopowder	CO <sub>2</sub>	350	5000	0.072 c	-	-	[246]
CuO/CuFe <sub>2</sub> O <sub>4</sub>	Radio-frequency sputtering	Thin films	H <sub>2</sub>	400	500	0.79 c	60 s/-	-	[247]
CuO/CuFe <sub>2</sub> O <sub>4</sub>	Water bath and calcination	Microspheres/nanoparticles	H <sub>2</sub> S	240	10	22.3 a	31 s/40 s	-	[248]
CuO/ZnFe <sub>2</sub> O <sub>4</sub>	Thermal treatment and solvothermal	Yolk-shell microspheres	Xylene	225	100	24.1 a	4 s/6 s	-	[249]
CuO/ZnFe <sub>2</sub> O <sub>4</sub>	Solvothermal	Porous nanospheres	H <sub>2</sub> S	RT	10	0.75 c	70 s/475 s	0.1 ppm	[250]
Fe <sub>2</sub> O <sub>3</sub> /CuFe <sub>2</sub> O <sub>4</sub>	Template-induced method	Hollow spheres	Acetone	250	100	14 a	6 s/100 s	100 ppb	[29]
Fe <sub>2</sub> O <sub>3</sub> /NiFe <sub>2</sub> O <sub>4</sub>	Metal-organic framework	Nanotubes	Acetone	200	100	23 a	4 s/-	-	[251]
Fe <sub>2</sub> O <sub>3</sub> /ZnFe <sub>2</sub> O <sub>4</sub>	Template-induced method	Porous microrods	TEA	305	100	42.4 a	12 s/26 s	-	[252]
Fe <sub>2</sub> O <sub>3</sub> /ZnFe <sub>2</sub> O <sub>4</sub>	Solvothermal	Core-shell nanorods	TEA	280	100	141 a	13 s/30 s	-	[253]
Fe <sub>2</sub> O <sub>3</sub> /ZnFe <sub>2</sub> O <sub>4</sub>	Solvothermal	Spindle-like	TEA	300	100	69.24 a	2 s/7 s	-	[254]
MgO/MgFe <sub>2</sub> O <sub>4</sub>	Co-precipitation	Thick film	H <sub>2</sub> S	200	3	1086 a	18 s/108 s	-	[255]
MgO/MgFe <sub>2</sub> O <sub>4</sub> /Fe <sub>2</sub> O <sub>3</sub>	Calcination	Core-shell microsphere	H <sub>2</sub> S	250	3	1.32 b	-	-	[256]
Mn <sub>2</sub> O <sub>3</sub> /ZnFe <sub>2</sub> O <sub>4</sub>	Co-precipitation	Nanopowder	Ethanol	325	300	0.76 c	-	-	[257]
NiO/NiFe <sub>2</sub> O <sub>4</sub>	Two-step hydrothermal	Nanotetrahedrons/nanoparticles	HCHO	240	200	33.3 a	12 s/8 s	200 ppb	[258]
NiO/NiFe <sub>2</sub> O <sub>4</sub>	Solvothermal	Nanosheets/Nanoparticles	Acetone	280	50	23 a	-	-	[259]
PdO/ZnFe <sub>2</sub> O <sub>4</sub>	Ultrasonic spray pyrolysis	Microporous spheres	Acetone	275	100	18.9 a	5 s/54 s	-	[260]
SiO <sub>2</sub> /In <sub>2</sub> O <sub>3</sub> /CoFe <sub>2</sub> O <sub>4</sub>	Hydrothermal	Microspheres	Acetone	260	100	58 a	1 s/59 s	-	[261]
Sn-doped ZnO/ZnFe <sub>2</sub> O <sub>4</sub>	Heat treatment	Porous heterostructures	TEA	270	10	28.1 a	9 s/7 s	0.2 ppm	[262]
SnO <sub>2</sub> /Mn <sub>0.5</sub> Cu <sub>0.5</sub> Fe <sub>2</sub> O <sub>4</sub>	Co-precipitation	Nanoparticles	CO <sub>2</sub>	RT	saturated	18 c	-	-	[263]
SnO <sub>2</sub> /ZnFe <sub>2</sub> O <sub>4</sub>	Sol-gel	Nanoparticles	Acetone	176	100	14.6 a	17 s/23 s	-	[264]
SnO <sub>2</sub> /ZnFe <sub>2</sub> O <sub>4</sub>	Solvothermal	Nanospheres	Acetone	210	100	120 a	30 s/197 s	0.1 ppm	[265]
Y <sub>2</sub> O <sub>3</sub> /CuFe <sub>2</sub> O <sub>4</sub>	Sol-gel	Nanoparticles	Humidity	RT	97%	4895 a	9 s/23 s	-	[266]
ZnO/Fe <sub>2</sub> O <sub>3</sub> /ZnFe <sub>2</sub> O <sub>4</sub>	auto-combustion	Nanoparticles	Humidity	RT	97%	4895 a	9 s/23 s	-	[266]
ZnO/Fe <sub>2</sub> O <sub>3</sub> /ZnFe <sub>2</sub> O <sub>4</sub>	Solvothermal	Thick film	Acetone	190	150	16.2 a	5 s/29 s	-	[267]
ZnO/ZnFe <sub>2</sub> O <sub>4</sub>	Screen-printing	Thick film	Propanol	RT	8000	3.54 c	40 s/70 s	-	[268]
ZnO/ZnFe <sub>2</sub> O <sub>4</sub>	Screen-printing	Thick film	Propanol	RT	1000	5.2 c	45 s/90 s	-	[269]
ZnO/ZnFe <sub>2</sub> O <sub>4</sub>	Screen-printing	Thick film	Propanol	RT	2000	0.15 c	-	-	[270]
ZnO/ZnFe <sub>2</sub> O <sub>4</sub>	Hydrothermal	Hollow microspheres	n-butanol	-	200	27.7 a	10 s/25 s	-	[271]
ZnO/ZnFe <sub>2</sub> O <sub>4</sub>	Solution reactions	Hollow spheres/nanosheets	Acetone	250	100	16.8 a	1 s/33 s	-	[272]
ZnO/ZnFe <sub>2</sub> O <sub>4</sub>	Two-step sprayed	Backbones/nanosheets	Ethanol	275	100	10.5 a	-	-	[273]
ZnO/ZnFe <sub>2</sub> O <sub>4</sub>	Hydrothermal	Rod-like	n-butanol	260	50	13.6 a	12 s/11 s	-	[274]
ZnO/ZnFe <sub>2</sub> O <sub>4</sub>	Calcination	Hexagonal	TEA	80	1000	12.7 a	100 s/-	-	[275]
ZnO/ZnFe <sub>2</sub> O <sub>4</sub>	Hydrothermal	Hollow spheres	Acetone	280	50	5.2 b	7.1 s/10.1 s	-	[276]
ZnO/ZnFe <sub>2</sub> O <sub>4</sub>	Pyrolysis	Hollow cube	Acetone	250	5	9.4 a	5.6/6 min	-	[277]

Table 10. Cont.

Materials	Synthesis	Morphology	Gas	O.T. (°C)	Conc. (ppm)	Response	$t_{res}/t_{rec}$	LOD	Refs.
ZnO/ZnFe <sub>2</sub> O <sub>4</sub>	MOF	Hollow nanocages	Acetone	290	100	25.8 a	8 s/32 s	-	[278]
ZnO/ZnFe <sub>2</sub> O <sub>4</sub>	Solution reaction and Co-precipitation	Actinomorphic flower-like	NO <sub>2</sub>	200	1	58 a	7/15 s	-	[279]
ZnO/ZnFe <sub>2</sub> O <sub>4</sub>	Annealing treatment	Triple-shelled hollow microspheres	acetone	140	200	23.5 a	5.2 s/12.8 s	-	[280]
ZnO/ZnFe <sub>2</sub> O <sub>4</sub>	Co-precipitation	Prussian blue analogue	TEA	170	100	7.6 a	1 s/9 s	-	[281]
ZnO/ZnFe <sub>2</sub> O <sub>4</sub>	Hydrolyzation of MOF-5	Nanoparticles	Acetone	190	100	30.8 a	4.7 s/10.3 s	-	[282]
ZnO/ZnFe <sub>2</sub> O <sub>4</sub>	Solvothermal	Core-shell hollow microsphere	Acetone	280	100	33.6 a	8 s/30 s	-	[283]
ZnO/ZnFe <sub>2</sub> O <sub>4</sub>	Solvothermal	Coral-like mesoporous Nanosheets assembled microspheres	TEA	240	50	21.3 a	0.9 s/23 s	-	[41]
ZnO/ZnFe <sub>2</sub> O <sub>4</sub>	Solution reaction	Tetrapods/moss-like	TMA	240	100	31.5 a	3.1 s/5.7 s	-	[284]
ZnO/ZnFe <sub>2</sub> O <sub>4</sub>	Calcination	Kiwifruit-like	H <sub>2</sub> S	250	2	1.5 a	2 s/9 s	0.6 ppb	[285]
ZnO/ZnFe <sub>2</sub> O <sub>4</sub>	MOF	Hollow microspheres	TEA	200	100	40.5 a	32 s/41 s	-	[286]
ZnO/ZnFe <sub>2</sub> O <sub>4</sub>	Pyrolysis	Microflowers	Acetone	200	1	8.7 c	-	-	[287]
ZnO/ZnFe <sub>2</sub> O <sub>4</sub>	Solution and Calcination	Nanoparticles	Acetone	250	50	8.3 a	2 s/-	-	[288]
ZnO/ZnFe <sub>2</sub> O <sub>4</sub>	Hydrothermal Electrospinning, Atomic layer deposition and Solution reaction	Nanoparticles	Acetone	120	90	92.9 a	7.7 s/27 s	-	[36]
ZnO/ZnFe <sub>2</sub> O <sub>4</sub> /Au		Nanomeses	Acetone	225	100	30.3 a	1 s/-	300 ppb	[219]
ZnO/ZnFe <sub>2</sub> O <sub>4</sub> /Au	Hydrothermal and Co-precipitation	Yolk-shell microspheres assembled from nanosheets	Acetone	206	100	18.18 a	4 s/23 s	0.7 ppm	[222]

a Response is defined as  $R_a/R_g$ ; b Response is defined as  $R_g/R_a$ ; c Response is defined as  $\Delta R/R_a$ ; d Response is defined as  $\Delta R/R_g$ .

Table 11. Summary of the reported 2D materials/spinel-ferrite-based gas sensors.

Materials	Synthesis	Morphology	Gas	O.T. (°C)	Conc. (ppm)	Response	$t_{res}/t_{rec}$	LOD	Refs.
g-C <sub>3</sub> N <sub>4</sub> /MgFe <sub>2</sub> O <sub>4</sub>	Solvothermal	Nanosheets/Nanoparticles	Ethanol	300	500	112 a	11 s/46 s	-	[289]
g-C <sub>3</sub> N <sub>4</sub> /MgFe <sub>2</sub> O <sub>4</sub>	Solvothermal	Nanosheets/Porous microspheres	Acetone	320	500	270 a	49 s/29 s	-	[290]
Graphene quantum dots/ZnFe <sub>2</sub> O <sub>4</sub>	Hydrothermal	Nanoparticles	Acetone	RT	1000	13.3 a	9 s/4 s	-	[291]
Graphene/ZnFe <sub>2</sub> O <sub>4</sub>	Solvothermal	Nanosheets/Nanoparticles	Acetone	275	1000	9.1 a	0.7 s/24.7 s	-	[292]
MoS <sub>2</sub> /CuFe <sub>2</sub> O <sub>4</sub>	Electrospinning	Nanosheets/Nanotubes	Acetone	RT	100	16.4 a	-	-	[293]
MWCNTs/NiFe <sub>2</sub> O <sub>4</sub>	Sol-gel	Nanotube/Nanoparticles	H <sub>2</sub> S	300	100	2.5 a	-	-	[294]
MWCNTs/Co <sub>0.8</sub> Ni <sub>0.2</sub> Fe <sub>2</sub> O <sub>4</sub>	Solvothermal	Nanotubes/Nanoparticles	NH <sub>3</sub>	-	4000	6.2 a	-	-	[295]
rGO/CuFe <sub>2</sub> O <sub>4</sub>	Combustion	Nanosheets/Nanoparticles	NH <sub>3</sub>	RT	50	0.093 c	3 s/6 s	-	[296]
rGO/NiFe <sub>2</sub> O <sub>4</sub>	Hydrothermal	Nanosheets/Nanoparticles	H <sub>2</sub>	80	200	3.85 a	32 s/85 s	-	[297]
rGO/WO <sub>3</sub> /ZnFe <sub>2</sub> O <sub>4</sub>	Water bath	Nanosheets/Massive/Nanoparticles	TEA	130	10	26.92 a	51 s/144 s	-	[298]
rGO/ZnFe <sub>2</sub> O <sub>4</sub>	Hydrothermal	Nanosheet/Nanorods	SO <sub>2</sub>	RT	100	0.183 c	46 s/54 s	-	[299]
rGO/ZnFe <sub>2</sub> O <sub>4</sub>	Calcination	Nanosheets/Hollow spheres	Acetone	200	10	8.18 a	23 s/203 s	0.8 ppm	[300]
rGO/ZnFe <sub>2</sub> O <sub>4</sub>	Electrospinning and Calcination	Nanosheets/Nanofibers	H <sub>2</sub> S	350	1	147 a	-	-	[301]
rGO/ZnFe <sub>2</sub> O <sub>4</sub>	Solvothermal	Nanosheets/Nanosheets	Ethanol	210	100	41.5 a	14 s/37 s	-	[302]
rGO/ZnFe <sub>2</sub> O <sub>4</sub>	Chemical precipitation	Nanosheets/Hollow octahedron	NO <sub>2</sub>	RT	2	1.123 d	50 s/250 s	0.14 ppb	[303]
rGO/ZnFe <sub>2</sub> O <sub>4</sub> /Pd	Microwave	Nanosheets/Nanoparticles	H <sub>2</sub>	RT	200	0.11 c	18 s/39 s	-	[304]

a Response is defined as  $R_a/R_g$ ; c Response is defined as  $\Delta R/R_a$ ; d Response is defined as  $\Delta R/R_g$ .

**Table 12.** Summary of the reported polymer/spinel-ferrite-based gas sensors.

Materials	Synthesis	Morphology	Gas	O.T. (°C)	Conc. (ppm)	Response	$t_{res}/t_{rec}$	LOD	Refs.
Polyacrylic acid/ NiFe <sub>2</sub> O <sub>4</sub>	Solvothermal	Thin film	NH <sub>3</sub>	150	100	4.1 a	-	-	[305]
Polyindole/ ZnFe <sub>2</sub> O <sub>4</sub>	In situ polymerization	Nanosheets/ Nanoparticles	NH <sub>3</sub>	RT	100	0.9 a	-	-	[306]
Polyaniline/ CuFe <sub>2</sub> O <sub>4</sub>	Polymerization	Nanocapsules/ Nanosphere	NH <sub>3</sub>	RT	5	0.27 c	84 s/54 s	-	[307]
Polyaniline/ NiFe <sub>2</sub> O <sub>4</sub>	Electrospinning and polymerization	Nanofibers	NH <sub>3</sub>	RT	100	30.8 c	15 s/21 s	250 ppb	[308]

a Response is defined as  $R_a/R_g$ ; c Response is defined as  $\Delta R/R_a$ .

### 5.1. Other MOSs/Ferrite

There are primarily two methods for synthesizing heterostructures between other metal oxides and spinel ferrite: the one-step method [283] and the multi-step method [258]. The one-step method can yield highly uniform heterostructures, forming microscopic heterojunctions, but it is challenging to control the ratio of the two phases [271]. The multi-step method allows for more precise control in different synthesis stages, including the reaction conditions, proportions, and reaction time, to obtain the desired product properties and structures. However, it increases the duration and cost of the synthesis process [273].

Xu et al. [258] conducted a study in which they prepared NiO/NiFe<sub>2</sub>O<sub>4</sub> nanocomposites using a straightforward two-step hydrothermal method. The nanocomposites consisted of NiO nano-tetrahedrons with numerous NiFe<sub>2</sub>O<sub>4</sub> nanoparticles dispersed on their outer surface (Figure 10a,b), forming p-p type heterojunctions. By adjusting the amount of Fe added during the synthesis process, the Fe to Ni ratio was optimized. The nanocomposite designated as NiFe-0.008 exhibited a remarkable gas-sensing performance (Figure 10c), with a high response of 19.1 towards 50 ppm formaldehyde smoke at 240 °C. Additionally, it displayed a low detection limit of 200 ppb and demonstrated good long-term stability. Comparatively, the optimized NiFe-0.008 nanocomposite outperformed individual NiO nano-tetrahedrons (with a response of 11.6 at 250 °C) and NiFe<sub>2</sub>O<sub>4</sub> nanoparticles (with a response of 6.8 at 300 °C) in terms of the gas-sensing performance. These findings highlight the improved response performance achieved by the optimized NiFe-0.008 nanocomposite. Hu et al. [248] conducted a study where they modified CuO microspheres by incorporating CuFe<sub>2</sub>O<sub>4</sub> nanoparticles (Figure 10f), resulting in CuFe<sub>2</sub>O<sub>4</sub>/CuO heterostructures. These heterostructures exhibited a high sensitivity to hydrogen H<sub>2</sub>S. The researchers investigated the relationship between the mass ratio of CuFe<sub>2</sub>O<sub>4</sub> to CuO and the operating temperature to optimize the sensor's response to H<sub>2</sub>S. The results of the study demonstrate that the optimized CuFe<sub>2</sub>O<sub>4</sub>/CuO heterostructures exhibited a significantly enhanced response to 10 ppm H<sub>2</sub>S at 240 °C (Figure 10g), reaching approximately 20 times that of the initial CuO microspheres. Moreover, the optimized heterostructures showed excellent fast response and recovery abilities. These findings suggest that the incorporation of CuFe<sub>2</sub>O<sub>4</sub> nanoparticles into CuO microspheres can effectively enhance the gas-sensing performance of the sensor towards H<sub>2</sub>S. The optimized CuFe<sub>2</sub>O<sub>4</sub>/CuO heterostructures demonstrated a substantial improvement in sensitivity compared with the preliminary CuO microspheres, making them promising candidates for the detection of H<sub>2</sub>S gas. Balaji et al. [263] conducted a study in which they synthesized SnO<sub>2</sub> composite Mn<sub>1-x</sub>CuFe<sub>2</sub>O<sub>4</sub> (x = 0, 0.5, and 1.0) nanocomposites with an equal mass percentage using the chemical coprecipitation method. The addition of SnO<sub>2</sub> to copper-substituted manganese ferrite resulted in an increase in grain size and a decrease in strain value. The morphological analysis revealed that the average particle size of the ferritic materials decreased linearly with the decrease in Mn<sup>2+</sup> concentration. The presence of SnO<sub>2</sub> on the surface of Cu-Mn ferrite led to an increase in particle size and a weakening of the magnetic properties. Furthermore, the addition of SnO<sub>2</sub> to MnFe<sub>2</sub>O<sub>4</sub> and Mn<sub>1-x</sub>Cu<sub>x</sub>Fe<sub>2</sub>O<sub>4</sub> enhanced the sensitivity of the gas sensor. MnFe<sub>2</sub>O<sub>4</sub> exhibited resistance to oxygen and carbon dioxide, while SnO<sub>2</sub>-CuFe<sub>2</sub>O<sub>4</sub>

showed a weak sensitivity. This indicates that the adsorption/chemisorption of oxygen or surface lattice oxygen atoms plays a dominant role in the complete oxidation of molecules. These findings highlight the impact of SnO<sub>2</sub> addition on the structural and gas-sensing properties of Mn<sub>1-x</sub>CuFe<sub>2</sub>O<sub>4</sub> nanocomposites. The changes in grain size, strain value, particle size, and gas sensitivity provide valuable insights into the design and optimization of gas-sensing materials for specific applications.

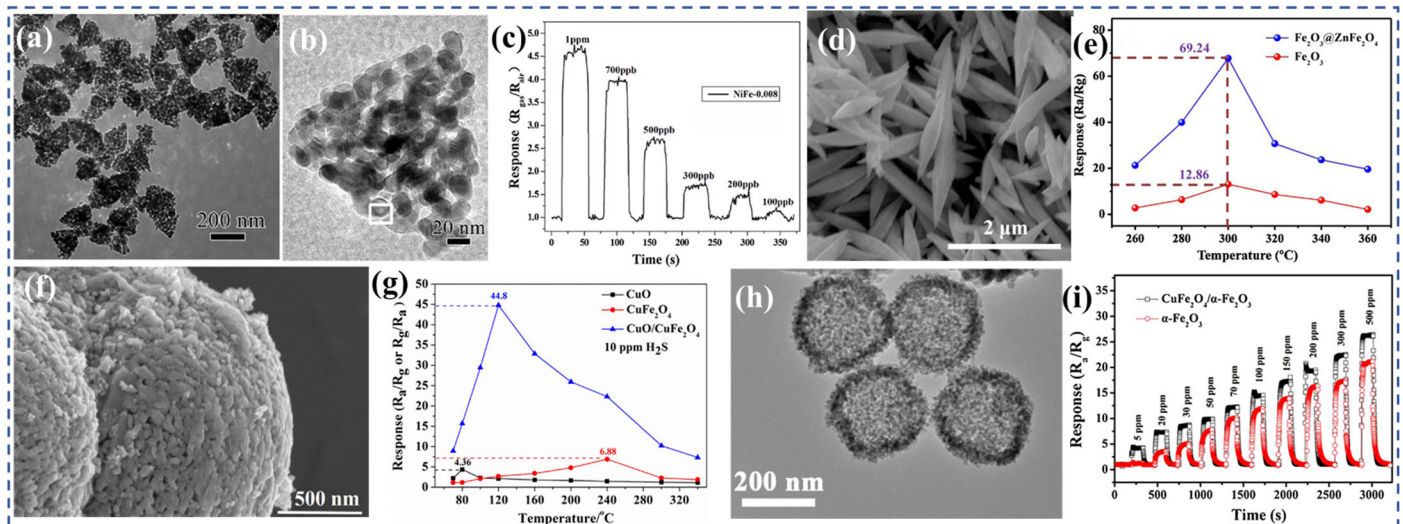


**Figure 10.** (a) SEM and (b) TEM images of NiO/NiFe<sub>2</sub>O<sub>4</sub>. (c) Dynamic curve of the NiO/NiFe<sub>2</sub>O<sub>4</sub>-sensor to formaldehyde with different concentrations at 240 °C. (d) SEM image of Fe<sub>2</sub>O<sub>3</sub>/ZnFe<sub>2</sub>O<sub>4</sub>. (e) Comparative analysis of the 100 ppm TEA response among sensors based on Fe<sub>2</sub>O<sub>3</sub> spindles and Fe<sub>2</sub>O<sub>3</sub>/ZnFe<sub>2</sub>O<sub>4</sub> at varying operating temperatures. (f) SEM images of CuO/CuFe<sub>2</sub>O<sub>4</sub>. (g) Comparative analysis of the 100 ppm TEA response among sensors based on CuO microspheres, CuFe<sub>2</sub>O<sub>4</sub> nanoparticles, and CuO/CuFe<sub>2</sub>O<sub>4</sub> heterostructure at varying operating temperatures. (h) TEM images of Fe<sub>2</sub>O<sub>3</sub>/CuFe<sub>2</sub>O<sub>4</sub> composite. (i) Gas-sensing performances of hollow Fe<sub>2</sub>O<sub>3</sub> and CuFe<sub>2</sub>O<sub>4</sub>/Fe<sub>2</sub>O<sub>3</sub>-2-composite-based sensors under various concentrations of acetone ranging from 5 to 500 ppm. (a–c) Reproduced with permission [258], copyright 2020, Elsevier B.V. (d,e) Reproduced with permission [254], copyright 2020, Elsevier B.V. (f,g) Reproduced with permission [248], copyright 2018, Elsevier B.V. (h,i) Reproduced with permission [29], copyright 2018, Elsevier B.V.

Wei et al. [254] successfully synthesized MOF-based Fe<sub>2</sub>O<sub>3</sub>/ZnFe<sub>2</sub>O<sub>4</sub> porous nanocomposites using a solvothermal method. The nanocomposites consist of spindles-like Fe<sub>2</sub>O<sub>3</sub> with a length of about 2 μm and a width of about 400 nm (Figure 10d), which are uniformly adhered to ZnFe<sub>2</sub>O<sub>4</sub> nanoparticles. Through the analysis of the TEA (triethylamine) gas-sensing mechanism, it was observed that the heterojunction between the spindles-like Fe<sub>2</sub>O<sub>3</sub> and ZnFe<sub>2</sub>O<sub>4</sub> nanoparticles played a crucial role in improving the gas-sensing performance. Compared with pure MOF-derived Fe<sub>2</sub>O<sub>3</sub> spindles, the gas-sensitive properties of Fe<sub>2</sub>O<sub>3</sub>/ZnFe<sub>2</sub>O<sub>4</sub> nanocomposites were enhanced and exhibited a remarkable response value of up to 69.24 when exposed to 100 ppm TEA (Figure 10e). This indicates a significant improvement in the gas-sensing performance of the nanocomposites compared with the pure Fe<sub>2</sub>O<sub>3</sub> spindles derived from MOF. Using Cu@carbon as a sacrificial template, Li et al. [29] successfully synthesized CuFe<sub>2</sub>O<sub>4</sub>/α-Fe<sub>2</sub>O<sub>3</sub> hollow spheres with a diameter of ~210 nm with porous non-thin shells (Figure 10h) by thermal oxidation and solid phase reaction. The gas-sensitive properties of CuFe<sub>2</sub>O<sub>4</sub>/α-Fe<sub>2</sub>O<sub>3</sub> composites were compared with those of pure α-Fe<sub>2</sub>O<sub>3</sub> hollow spheres. As anticipated, the sensor based on the CuFe<sub>2</sub>O<sub>4</sub>/α-Fe<sub>2</sub>O<sub>3</sub> composite exhibited a higher sensitivity (R<sub>a</sub>/R<sub>g</sub> = 14), faster response and recovery times (6 s/100 s), and lower detection limits (100 ppb) compared with the original α-Fe<sub>2</sub>O<sub>3</sub> hollow spheres (Figure 10i). The enhanced sensing performance of the CuFe<sub>2</sub>O<sub>4</sub>/α-Fe<sub>2</sub>O<sub>3</sub> composites can be attributed to several factors. Firstly, the hollow porous structure of the

composites provides a larger surface area, which increases the number of active sites for gas adsorption and improves sensitivity. Additionally, the presence of the heterojunction between  $\text{CuFe}_2\text{O}_4$  and  $\alpha\text{-Fe}_2\text{O}_3$  allows for modulation of the resistance and facilitates charge transfer, further enhancing the gas-sensing performance. Lastly, the catalytic performance of  $\text{CuFe}_2\text{O}_4$  in the composites contributes to the improved sensing properties.

Li et al. [287] utilized a metal–organic skeleton to prepare a precursor similar to Prussian blue, and then employed direct pyrolysis to fabricate hollow  $\text{ZnO}/\text{ZnFe}_2\text{O}_4$  microspheres with a heterogeneous structure (Figure 11a). These microspheres had a diameter of approximately 1.5  $\mu\text{m}$ . As a gas-sensitive material, the hollow  $\text{ZnO}/\text{ZnFe}_2\text{O}_4$  microspheres exhibited a temperature-dependent n–p–n-type abnormal conductive transition (Figure 11b) when detecting low concentrations of volatile organic compounds (VOCs) such as ethanol, acetone, toluene, and benzene. This phenomenon can be primarily attributed to the interplay of highly separated electron–hole pairs caused by the staggered band arrangement at the heterogeneous interface of the  $\text{ZnO}-\text{ZnFe}_2\text{O}_4$  shell. This interplay is influenced by the heat-dependent ionization reaction of the surface-absorbed oxygen molecules and the additional electron injection resulting from the reducing VOCs' surface reaction during the gas-sensitive process. The abnormal conductive transition observed in the hollow  $\text{ZnO}/\text{ZnFe}_2\text{O}_4$  microspheres when exposed to low concentrations of VOCs is a result of the complex interplay between the different processes occurring at the heterogeneous interface. This understanding of the underlying mechanism contributes to the understanding and optimization of gas-sensing properties for applications in VOC detection. Wang et al. [278] devised a design and synthesis method to create  $\text{ZnO}/\text{ZnFe}_2\text{O}_4$  hollow nanocages with a diameter of around 100 nm using a metal–organic framework (MOF) technique. The synthesis process involved two steps: the preparation of  $\text{Fe(III)MOF-5}$  nanocages as a precursor, followed by the conversion into  $\text{ZnO}/\text{ZnFe}_2\text{O}_4$  hollow nanocages through hot annealing in air. Based on the BET analysis, it is observed that the  $\text{ZnO}/\text{ZnFe}_2\text{O}_4$  nanocages, in their as-prepared state, possessed a BET specific surface area of 48.4  $\text{m}^2\cdot\text{g}^{-1}$  and an average pore size of 9.1 nm, as determined using the BJH method (Figure 11c). Gas-sensing experiments revealed that the  $\text{ZnO}/\text{ZnFe}_2\text{O}_4$  hollow nanocages exhibited a superior response value of 25.8 to 100 ppm acetone (Figure 11g), with a detection limit of 1 ppm at the optimized temperature of 290 °C. This response value surpassed that of  $\text{ZnO}$  hollow nanocages (7.9) and  $\text{ZnFe}_2\text{O}_4$  nanospheres (8.1). Furthermore, the gas-sensing response of the  $\text{ZnO}/\text{ZnFe}_2\text{O}_4$  nanocages outperformed that of the other structures, with the response order being as follows: hollow nanocages > double shell > hollow microsphere; hybrid hollow spheres > nanoparticles with rods. Yang et al. [41] conducted a study in which they synthesized coral-like  $\text{ZnFe}_2\text{O}_4\text{-ZnO}$  heterostructures with mesoporous structures (Figure 11d,e) and evaluated their gas-sensing performance towards the volatile organic compound TEA. The prepared sensor was subjected to thorough gas-sensing tests, and the results demonstrated several advantages, including a high response value ( $R_a/R_g = 21.3$  at 240 °C), fast response and recovery times (0.9 s/23 s), and good repeatability (Figure 11f). The combination of the unique coral-like mesoporous morphology, the formation of n–n heterojunctions, and the synergistic effect of  $\text{ZnFe}_2\text{O}_4$ 's Bronsted centers contributed to the improved TEA sensing properties of the coral-like  $\text{ZnFe}_2\text{O}_4\text{-ZnO}$ . These findings provide valuable insights for the design and optimization of gas-sensing materials for the detection of volatile organic compounds.

## 5.2. Nanostructure Materials/Ferrite

In order to maintain the structural stability of nanostructured materials during heterojunction formation, a two-step method is typically employed [300]. This approach not only maintains the stability of the structural materials, but also suppresses the aggregation of the perovskite iron oxides during synthesis [304].

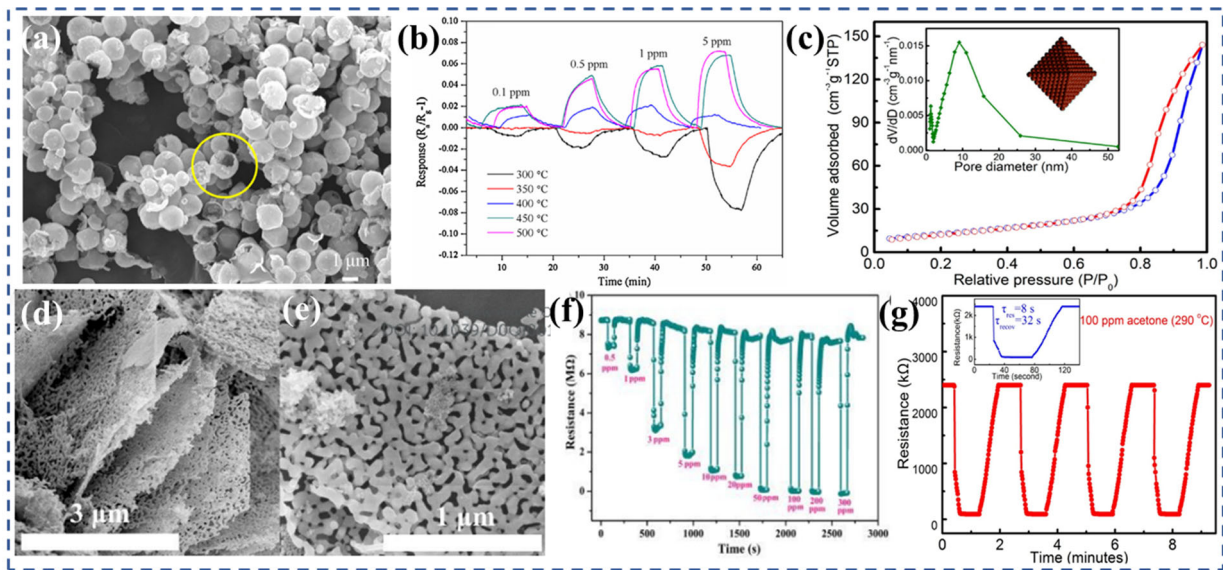


**Figure 11.** (a) SEM images of hollow ZnO/ZnFe<sub>2</sub>O<sub>4</sub> microspheres. (b) Response value towards acetone with 0.1–5 ppm. (c) N<sub>2</sub> adsorption–desorption isotherms for ZnO/ZnFe<sub>2</sub>O<sub>4</sub> nanocages (inset is the pore size distribution). (d,e) SEM images of the coral-like ZnO/ZnFe<sub>2</sub>O<sub>4</sub> with different magnifications. (f) Dynamic response/recover curves of the coral-like ZnO/ZnFe<sub>2</sub>O<sub>4</sub> to different TEA concentrations at 240 °C. (g) Dynamic continuous response of ZnO/ZnFe<sub>2</sub>O<sub>4</sub> hollow nanocages to 100 ppm acetone at 290 °C. (a,b) Reproduced with permission [287], copyright 2017, Elsevier B.V. (c,g) Reproduced with permission [278], copyright 2017, Elsevier B.V. (d–f) Reproduced with permission [41], copyright 2019, Elsevier B.V.

Nanostructured materials, such as two-dimensional (2D), one-dimensional (1D), and zero-dimensional (0D) structures, possess unique dimensional characteristics that contribute to their attractive physicochemical properties. These structures exhibit small volume, high electron mobility, and large specific surface areas, making them highly advantageous in various applications. In the field of gas sensing, nanostructures with a large surface area and high porosity have been found to significantly enhance the performance of gas sensors. The increased surface area and porosity provide more reaction sites, enabling more efficient interaction between the sensing material and the target gas molecules. This enhanced interaction leads to improved sensitivity and selectivity in gas-sensing applications. A notable strategy to achieve synergistic effects is the integration of metal oxide semiconductor (MOS) materials with nanostructured materials possessing large specific surface areas.

Zhang et al. [290] achieved the successful synthesis of porous microsphere composites by incorporating g-C<sub>3</sub>N<sub>4</sub> into MgFe<sub>2</sub>O<sub>4</sub> (Figure 12a,b) using a solvothermal method. In the study, the content of g-C<sub>3</sub>N<sub>4</sub> was varied, and it was found that the sensor based on the MgFe<sub>2</sub>O<sub>4</sub>/g-C<sub>3</sub>N<sub>4</sub> composite material exhibited excellent gas-sensing performance. Specifically, when the g-C<sub>3</sub>N<sub>4</sub> content was 10 wt.%, the sensor showed several desirable characteristics, including high sensitivity and selectivity, fast response and recovery times. Notably, the maximum response to acetone increased by approximately 145 times compared with the sensors without g-C<sub>3</sub>N<sub>4</sub>. Moreover, the optimal temperature for sensing was reduced by 60 °C. Chu et al. [291] conducted a study in which they prepared ZnFe<sub>2</sub>O<sub>4</sub>/graphene quantum dot (GQD) nanocomposites (Figure 12c) using a hydrothermal method. The researchers aimed to investigate the influence of GQD content on the gas-sensitive response and selectivity of the ZnFe<sub>2</sub>O<sub>4</sub>/GQD nanocomposites. The results demonstrated that the sensor based on the ZnFe<sub>2</sub>O<sub>4</sub>/GQD nanocomposites exhibited a response of 13.3 to 1000 ppm acetone and a response of 1.2 to 5 ppm acetone at room temperature (Figure 12d). The response time and recovery time for the detection of acetone were both less than 12 s. However, it should be noted that the long-term gas-sensitive

stability of the  $\text{ZnFe}_2\text{O}_4/\text{GQD}$  nanocomposites was not satisfactory. This indicates that further research and improvement are needed to address the stability issue and enhance the long-term performance of the nanocomposites in gas-sensing applications. Bai et al. [298] synthesized  $\text{rGO}/\text{WO}_3/\text{ZnFe}_2\text{O}_4$  composites (Figure 12e,f) with varying proportions using hydrothermal, chemical water bath, and chemical reduction methods. The gas sensitivity of the synthesized composites was tested, yielding noteworthy results. Among the different compositions tested, the 0.8 wt.%  $\text{rGO}/9\text{WO}_3\text{-ZnFe}_2\text{O}_4$  terpolymer exhibited a superior gas-sensing performance. It demonstrated a significantly higher response value of 26.92, which is six times higher than that of pure  $\text{WO}_3$  and thirteen times higher than that of  $\text{ZnFe}_2\text{O}_4$  (Figure 12i). Furthermore, the synthesized gas-sensitive material displayed excellent selectivity, a shorter response time of 51 s, and a lower detection limit of 0.02 ppm. These characteristics indicate the enhanced performance of the composite material in terms of sensitivity, selectivity, and response speed compared with the individual components. The successful synthesis of the  $\text{rGO}/\text{WO}_3/\text{ZnFe}_2\text{O}_4$  composites and their improved gas-sensing performance suggest their potential for applications in gas-sensing devices. Further optimization and exploration of the composite composition and structure can enable the development of highly efficient gas sensors for various target gases.

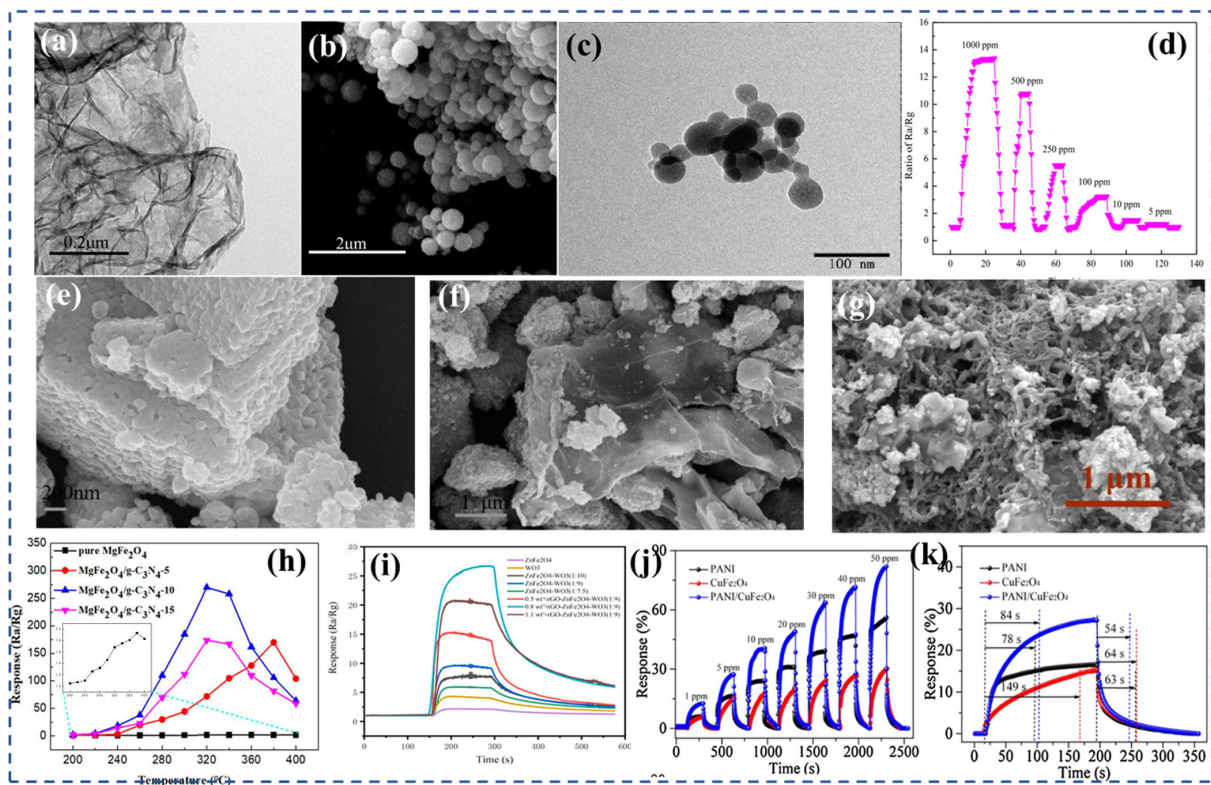


**Figure 12.** (a) TEM image of  $\text{g-C}_3\text{N}_4$ . (b) SEM image of  $\text{MgFe}_2\text{O}_4/\text{g-C}_3\text{N}_4$  composites. (c) TEM images of  $\text{ZnFe}_2\text{O}_4/\text{GQDs}$ . (d) The dynamic response/recover curves of the sensor based on the sample S-15 composite to various concentrations of acetone at RT. (e) SEM image of  $9\text{WO}_3\text{-ZnFe}_2\text{O}_4$ . (f) SEM micrographs of the  $0.8\text{ wt.}\% \text{rGO}/9\text{WO}_3/\text{ZnFe}_2\text{O}_4$  composite. (g) SEM images of  $\text{PANI}/\text{CuFe}_2\text{O}_4$ . (h) The sensitivity-temperature characteristics of the sensors based on  $\text{MgFe}_2\text{O}_4/\text{g-C}_3\text{N}_4$  composites to 500 ppm acetone. (i) Dynamic responses curve of the different ratio of  $\text{rGO}/\text{WO}_3/\text{ZnFe}_2\text{O}_4$  composites; (j) Response of the sensors toward  $\text{NH}_3$  at  $20\text{ }^\circ\text{C}$ . (k) Response and recovery curves of the sensors toward 5 ppm  $\text{NH}_3$  at  $20\text{ }^\circ\text{C}$ . (a,b,h) Reproduced with permission [290], copyright 2018, MDPI. (c,d) Reproduced with permission [291], copyright 2019, Elsevier B.V. (e,f,i) Reproduced with permission [298], copyright 2021, Elsevier B.V. (g,j,k) Reproduced with permission [307], copyright 2020, Elsevier B.V.

### 5.3. Conducting Polymer/Ferrite

In recent years, the synthesis of conductive polymer magnetic nanocomposites has received much attention from researchers because of its lightweight, low-cost preparation methods, and enhanced magnetoelectric properties. Among conductive polymers, polyaniline (PANI) has emerged as a P-type semiconductor material with an excellent sensing ability. While polyaniline-based ammonia sensors have been widely reported, developing faster, highly sensitive, and fully recyclable greenhouse gas sensors remain a major challenge. In this regard, Wang et al. [307] prepared polyaniline/CuFe<sub>2</sub>O<sub>4</sub> heterostructures (Figure 12j) through in situ polymerization. In contrast with the polyaniline-based sensor, the polyaniline/CoFe<sub>2</sub>O<sub>4</sub> composite showed a higher response, with a response of up to 27.37% at 5 ppm NH<sub>3</sub>, surpassing the performance of the original PANI and CuFe<sub>2</sub>O<sub>4</sub> films by a significant margin. This finding suggests that by combining CuFe<sub>2</sub>O<sub>4</sub> with polyaniline to form a p–n heterojunction, the gas-sensing performance could be enhanced (Figure 12j,k). The p–n heterojunction formed between CuFe<sub>2</sub>O<sub>4</sub> and polyaniline is expected to improve the gas-sensing performance of polyaniline-based sensors. The synergies between the two materials allows for increased sensitivity, faster response times, and better recoverability.

## 6. Summary and Prospect

This paper provides an exhaustive review of the advancements in spinel-ferrite-based gas sensors, emphasizing three critical areas: nanostructure, elemental doping, and heterostructure. Spinel ferrite gas sensors have garnered interest due to their broad sensitivity and excellent selectivity to various flammable, explosive, toxic, and harmful gases. The gas-sensing mechanism of these sensors depends on intricate interactions and electron transfer at the gas–solid interface. Consequently, alterations in the microstructure of spinel ferrite nanomaterials, such as grain size, specific surface area, and porosity, can substantially influence the sensor's gas-sensing performance. Metal element doping in spinel ferrite enhances the specific surface area and provides activation energy, while maintaining the original crystal structure. Moreover, the creation of heterojunctions at the interface between different gas-sensitive materials is pivotal in modulating the sensor response by forming an electron depletion layer. A detailed comparison reveals that refining the microstructure, suitable metal element doping, or employing material composites can lead to a certain level of enhancement in the sensing capabilities of gas sensors based on spinel ferrite. Nonetheless, practical applications face challenges, including high power consumption due to thermal excitation effects and extended recovery times due to slow gas desorption. Therefore, innovative research directions are required to achieve swift sensor recuperation and consistent detection at low temperatures, potentially even at ambient room temperature. To overcome these challenges, we suggest a blend of the aforementioned strategies, which may encompass refining the microstructure of spinel ferrites or controlling the iron stoichiometry, designing composite materials composed of spinel ferrite multi-layer porous shells or hollow spheres integrated with nanostructured materials such as reduced graphene oxide and molybdenum disulfide, and developing multi-component hybrid materials. These strategies aim to boost the performance of spinel ferrite gas sensors, with a primary emphasis on achieving a high response and low operating temperatures.

**Author Contributions:** Conceptualization, Y.W. and J.C.; validation, C.Q., Y.W. and H.B.; formal analysis, J.C.; investigation, R.Z.; data curation, R.Z.; writing—original draft preparation, R.Z.; writing—review and editing, C.Q.; visualization, Y.W.; supervision, J.C. All authors have read and agreed to the published version of the manuscript.

**Funding:** This work was funded by the National Natural Science Foundation of China (62273134 and 62173129), Program for Science and Technology Innovative Research Team at the University of Henan Province (21IRTSTHN006), the Natural Science Foundation of Henan Province (212300410042), Key Science and Technology Program of Henan Province (232102220009), the Fundamental Research Funds for the Universities of Henan Province (NSFRF220101 and NSFRF230432), and the Key Scientific Research Projects of Colleges and Universities in Henan Province (23A150012).

**Data Availability Statement:** No new data were created or analyzed in this study. Data sharing is not applicable to this article.

**Conflicts of Interest:** The authors declare no conflict of interest.

## References

1. Nadargi, D.Y.; Umar, A.; Nadargi, J.D.; Lokare, S.A.; Akbar, S.; Mulla, I.S.; Suryavanshi, S.S.; Bhandari, N.L.; Chaskar, M.G. Gas sensors and factors influencing sensing mechanism with a special focus on MOS sensors. *J. Mater. Sci.* **2023**, *58*, 559–582.
2. Yang, X.; Deng, Y.; Yang, H.; Liao, Y.; Cheng, X.; Zou, Y.; Wu, L.; Deng, Y. Functionalization of Mesoporous Semiconductor Metal Oxides for Gas Sensing: Recent Advances and Emerging Challenges. *Adv. Sci.* **2023**, *10*, 2204810. [[CrossRef](#)] [[PubMed](#)]
3. Das, S.; Jayaraman, V. SnO<sub>2</sub>: A comprehensive review on structures and gas sensors. *Prog. Mater. Sci.* **2014**, *66*, 112–255.
4. Kurugundla, G.K.; Godavarti, U.; Saidireddy, P.; Pothukanuri, N. Zinc oxide based gas sensors and their derivatives: A critical review. *J. Mater. Chem. C* **2023**, *11*, 3906–3925.
5. Tian, X.; Cui, X.; Lai, T.; Ren, J.; Yang, Z.; Xiao, M.; Wang, B.; Xiao, X.; Wang, Y. Gas sensors based on TiO<sub>2</sub> nanostructured materials for the detection of hazardous gases: A review. *Nano Mater. Sci.* **2021**, *3*, 390–403. [[CrossRef](#)]
6. Kukkola, J.; Mäklin, J.; Halonen, N.; Kyllönen, T.; Tóth, G.; Szabó, M.; Shchukarev, A.; Mikkola, J.-P.; Jantunen, H.; Kordás, K. Gas sensors based on anodic tungsten oxide. *Sens. Actuators B* **2011**, *153*, 293–300.
7. Cho, S.-Y.; Yoo, H.-W.; Kim, J.Y.; Jung, W.-B.; Jin, M.L.; Kim, J.-S.; Jeon, H.-J.; Jung, H.-T. High-resolution p-type metal oxide semiconductor nanowire array as an ultrasensitive sensor for volatile organic compounds. *Nano Lett.* **2016**, *16*, 4508–4515. [[CrossRef](#)]
8. Kauffman, D.R.; Star, A. Carbon nanotube gas and vapor sensors. *Angew. Chem. Int. Ed.* **2008**, *47*, 6550–6570. [[CrossRef](#)]
9. Beckers, N.; Taschuk, M.; Brett, M. Selective room temperature nanostructured thin film alcohol sensor as a virtual sensor array. *Sens. Actuators B* **2013**, *176*, 1096–1102. [[CrossRef](#)]
10. Pan, H.; Zhou, L.; Zheng, W.; Liu, X.; Zhang, J.; Pinna, N. Atomic layer deposition to heterostructures for application in gas sensors. *Int. J. Extreme Manuf.* **2023**, *5*, 22008. [[CrossRef](#)]
11. Srivastava, S.; Pal, P.; Sharma, D.K.; Kumar, S.; Senguttuvan, T.; Gupta, B.K. Ultrasensitive Boron–Nitrogen-Codoped CVD Graphene-Derived NO<sub>2</sub> Gas Sensor. *ACS Mater. Au* **2022**, *2*, 356–366. [[CrossRef](#)] [[PubMed](#)]
12. Sriram, S.R.; Parne, S.R.; Pothukanuri, N.; Edla, D.R. Prospects of spray pyrolysis technique for gas sensor applications-A comprehensive review. *J. Anal. Appl. Pyrolysis* **2022**, *164*, 105527.
13. Zhang, D.; Yang, Z.; Yu, S.; Mi, Q.; Pan, Q. Diversiform metal oxide-based hybrid nanostructures for gas sensing with versatile prospects. *Coord. Chem. Rev.* **2020**, *413*, 213272.
14. Majhi, S.M.; Mirzaei, A.; Kim, H.W.; Kim, S.S.; Kim, T.W. Recent advances in energy-saving chemiresistive gas sensors: A review. *Nano Energy* **2021**, *79*, 105369.
15. Selvakumar, D.; Sonu, K.; Ramadoss, G.; Sivaramkrishnan, R.; Jayavel, R.; Eswaramoorthy, M.; Rao, K.V.; Pugazhendhi, A. Heterostructures of polyaniline and Ce-ZnO nanomaterial coated flexible PET thin films for LPG gas sensing at standard environment. *Chemosphere* **2023**, *314*, 137492. [[CrossRef](#)]
16. Souri, M.; Yamini, Y.; Amoli, H.S. The synergistic effect of Ce dopant/Cotton bio-template on the performance of the SnO<sub>2</sub> gas sensor for the detection of Ethanol. *Mater. Sci. Eng.* **2023**, *294*, 116501.
17. Qu, Z.; Li, Y.; Xu, R.; Li, C.; Wang, H.; Wang, H.; Zhang, Y.; Wei, Q. Candy-like heterojunction nanocomposite of WO<sub>3</sub>/Fe<sub>2</sub>O<sub>3</sub>-based semiconductor gas sensor for the detection of triethylamine. *Microchim. Acta* **2023**, *190*, 139. [[CrossRef](#)] [[PubMed](#)]
18. Zhou, J.; Lin, Y.; Yang, H.; Ren, Y.; Xu, F. Structural, morphological and magnetic properties of low temperature sintered LiZnTiBi ferrites. *J. Alloys Compd.* **2023**, *932*, 167616.
19. Vinod, G.; Rajashekhar, K.; Naik, J.L. Dysprosium doped Cu<sub>0.8</sub>Cd<sub>0.2</sub>Dy<sub>x</sub>Fe<sub>2-x</sub>O<sub>4</sub> nano ferrites: A combined impact of Dy<sup>3+</sup> on enhanced physical, optical, magnetic, and DC-electrical properties. *Ceram. Int.* **2023**, *49*, 2829–2851.
20. Wang, X.; Lv, X.; Liu, Z.; Zhang, H.; Liu, M.; Xu, C.; Zhou, X.; Yuan, M.; Yang, L.; You, W. Multi-interfacial 1D magnetic ferrite@C fibers for Broadband microwave absorption. *Mater. Today Phys.* **2023**, *35*, 101140. [[CrossRef](#)]
21. Kumari, S.; Dhanda, N.; Thakur, A.; Gupta, V.; Singh, S.; Kumar, R.; Hameed, S.; Thakur, P. Nano Ca-Mg-Zn ferrites as tuneable photocatalyst for UV light-induced degradation of rhodamine B dye and antimicrobial behavior for water purification. *Ceram. Int.* **2023**, *49*, 12469–12480. [[CrossRef](#)]
22. Singh, S.; Singh, A.; Yadav, B.C.; Tandon, P. Synthesis, characterization, magnetic measurements and liquefied petroleum gas sensing properties of nanostructured cobalt ferrite and ferric oxide. *Mater. Sci. Semicond. Process.* **2014**, *23*, 122–135. [[CrossRef](#)]
23. Srivastava, R.; Yadav, B.C.; Singh, M.; Yadav, T.P. Synthesis, Characterization of Nickel Ferrite and Its Uses as Humidity and LPG Sensors. *J. Inorg. Organomet. Polym. Mater.* **2016**, *26*, 1404–1412. [[CrossRef](#)]
24. Rathore, D.; Kurchania, R.; Pandey, R.K. Fabrication of Ni<sub>1-x</sub>Zn<sub>x</sub>Fe<sub>2</sub>O<sub>4</sub> (x = 0, 0.5 and 1) nanoparticles gas sensor for some reducing gases. *Sens. Actuators A* **2013**, *199*, 236–240. [[CrossRef](#)]
25. Abu-Hani, A.F.S.; Mahmoud, S.T.; Awwad, F.; Ayeshe, A.I. Design, fabrication, and characterization of portable gas sensors based on spinel ferrite nanoparticles embedded in organic membranes. *Sens. Actuators B* **2017**, *241*, 1179–1187. [[CrossRef](#)]
26. Maharajan, M.; Mursalin, M.D.; Narjinary, M.; Rana, P.; Sen, S.; Sen, A. Synthesis, Characterization and Vapour Sensing Properties of Nanosized ZnFe<sub>2</sub>O<sub>4</sub>. *Trans. Indian Ceram. Soc.* **2014**, *73*, 102–104. [[CrossRef](#)]

27. De Oliveira, R.C.; Pontes Ribeiro, R.A.; Cruvinel, G.H.; Ciola Amoresi, R.A.; Carvalho, M.H.; Aparecido de Oliveira, A.J.; de Oliveira, M.C.; de Lazaro, S.R.; da Silva, L.F.; Catto, A.C.; et al. Role of Surfaces in the Magnetic and Ozone Gas-Sensing Properties of ZnFe<sub>2</sub>O<sub>4</sub> Nanoparticles: Theoretical and Experimental Insights. *ACS Appl. Mater. Interfaces* **2021**, *13*, 4605–4617. [[CrossRef](#)] [[PubMed](#)]
28. Chethan, B.; Ravikiran, Y.T.; Vijayakumari, S.C.; Rajprakash, H.G.; Thomas, S. Nickel substituted cadmium ferrite as room temperature operable humidity sensor. *Sens. Actuators A* **2018**, *280*, 466–474. [[CrossRef](#)]
29. Li, X.; Lu, D.; Shao, C.; Lu, G.; Li, X.; Liu, Y. Hollow CuFe<sub>2</sub>O<sub>4</sub>/α-Fe<sub>2</sub>O<sub>3</sub> composite with ultrathin porous shell for acetone detection at ppb levels. *Sens. Actuators B* **2018**, *258*, 436–446. [[CrossRef](#)]
30. Gavilán, H.; Rizzo, G.M.; Silvestri, N.; Mai, B.T.; Pellegrino, T. Scale-up approach for the preparation of magnetic ferrite nanocubes and other shapes with benchmark performance for magnetic hyperthermia applications. *Nat. Protoc.* **2023**, *18*, 783–809. [[CrossRef](#)] [[PubMed](#)]
31. Shen, L.; Lan, G.; Lu, L.; Ma, C.; Cao, C.; Jiang, C.; Fu, H.; You, C.; Lu, X.; Yang, Y. A strategy to modulate the bending coupled microwave magnetism in nanoscale epitaxial lithium ferrite for flexible spintronic devices. *Adv. Sci.* **2018**, *5*, 1800855. [[CrossRef](#)] [[PubMed](#)]
32. Wang, W.; Gumfekar, S.P.; Jiao, Q.; Zhao, B. Ferrite-grafted polyaniline nanofibers as electromagnetic shielding materials. *J. Mater. Chem. C* **2013**, *1*, 2851–2859. [[CrossRef](#)]
33. Kefeni, K.K.; Mamba, B.B.; Msagati, T.A. Application of spinel ferrite nanoparticles in water and wastewater treatment: A review. *Sep. Purif. Technol.* **2017**, *188*, 399–422.
34. Scheffe, J.R.; Allendorf, M.D.; Coker, E.N.; Jacobs, B.W.; McDaniel, A.H.; Weimer, A.W. Hydrogen production via chemical looping redox cycles using atomic layer deposition-synthesized iron oxide and cobalt ferrites. *Chem. Mater.* **2011**, *23*, 2030–2038. [[CrossRef](#)]
35. Wei, K.; Huai, H.-X.; Zhao, B.; Zheng, J.; Gao, G.-Q.; Zheng, X.-Y.; Wang, C.-C. Facile synthesis of CoFe<sub>2</sub>O<sub>4</sub> nanoparticles and their gas sensing properties. *Sens. Actuators B* **2022**, *369*, 132279. [[CrossRef](#)]
36. Nemufulwi, M.I.; Swart, H.C.; Shingange, K.; Mhlongo, G.H. ZnO/ZnFe<sub>2</sub>O<sub>4</sub> heterostructure for conductometric acetone gas sensors. *Sens. Actuators B* **2023**, *377*, 133027. [[CrossRef](#)]
37. Rathore, D.; Mitra, S.; Kurchania, R.; Pandey, R.K. Physicochemical properties of CuFe<sub>2</sub>O<sub>4</sub> nanoparticles as a gas sensor. *J. Mater. Sci. Mater. Electron.* **2018**, *29*, 1925–1932. [[CrossRef](#)]
38. Zhang, J.; Chen, D.; Chen, L. Preparation of ultrafine ZnFe<sub>2</sub>O<sub>4</sub> and its gas-sensing properties for Cl<sub>2</sub>. *Sens. Mater.* **2006**, *18*, 277–282.
39. Zhang, Y.; Zhou, Y.; Li, Z.; Chen, G.; Mao, Y.; Guan, H.; Dong, C. MOFs-derived NiFe<sub>2</sub>O<sub>4</sub> fusiforms with highly selective response to xylene. *J. Alloys Compd.* **2019**, *784*, 102–110. [[CrossRef](#)]
40. Wu, K.; Lu, Y.; Liu, Y.; Liu, Y.; Shen, M.; Debliquy, M.; Zhang, C. Synthesis and acetone sensing properties of copper (Cu<sup>2+</sup>) substituted zinc ferrite hollow micro-nanospheres. *Ceram. Int.* **2020**, *46*, 28835–28843. [[CrossRef](#)]
41. Yang, T.; Yang, X.; Zhu, M.; Zhao, H.; Zhang, M. Coral-like ZnFe<sub>2</sub>O<sub>4</sub>-ZnO mesoporous heterojunction architectures: Synthesis and enhanced sensing properties for triethylamine. *Inorg. Chem. Front.* **2020**, *7*, 1918–1926. [[CrossRef](#)]
42. Afzal, A.; Mujahid, A.; Iqbal, N.; Javaid, R.; Qazi, U.Y. Enhanced High-Temperature (600 degrees C) NO<sub>2</sub> Response of ZnFe<sub>2</sub>O<sub>4</sub> Nanoparticle-Based Exhaust Gas Sensors. *Nanomaterials* **2020**, *10*, 2133. [[CrossRef](#)] [[PubMed](#)]
43. Liu, X.; Xu, Z.; Liu, Y.; Shen, Y. A novel high performance ethanol gas sensor based on CdO-Fe<sub>2</sub>O<sub>3</sub> semiconducting materials. *Sens. Actuators B* **1998**, *52*, 270–273. [[CrossRef](#)]
44. Chu, X.; Zheng, C. Sulfide-sensing characteristics of MFe<sub>2</sub>O<sub>4</sub> (M = Zn, Cd, Mg and Cu) thick film prepared by co-precipitation method. *Sens. Actuators B* **2003**, *96*, 504–508. [[CrossRef](#)]
45. Gopal Reddu, C.V.; Manorama, S.V.; Rao, V.J. Preparation and characterization of ferrites as gas sensor materials. *J. Mater. Sci. Lett.* **2000**, *19*, 775–778. [[CrossRef](#)]
46. Chu, X.; Jiang, D.; Yu, G.; Zheng, C. Ethanol gas sensor based on CoFe<sub>2</sub>O<sub>4</sub> nano-crystallines prepared by hydrothermal method. *Sens. Actuators B* **2006**, *120*, 177–181. [[CrossRef](#)]
47. Raut, S.D.; Awasarmol, V.V.; Ghule, B.G.; Shaikh, S.F.; Gore, S.K.; Sharma, R.P.; Pawar, P.P.; Mane, R.S. Enhancement in room-temperature ammonia sensor activity of size-reduced cobalt ferrite nanoparticles on gamma-irradiation. *Mater. Res. Express* **2018**, *5*, 65035. [[CrossRef](#)]
48. Montahaei, R.; Emamian, H.R. The impact of microwave-assisted sintering on fabrication of cobalt ferrite nanostructure foams for gas-sensing. *Ceram. Int.* **2022**, *48*, 26629–26637. [[CrossRef](#)]
49. Umesh, S.; Usha, A.; Bailey, K.; Sujatha, K.; Varadharajaperumal, S.; Shivashankar, S.A.; Raghavan, M.S. Nanocrystalline Spinel CoFe<sub>2</sub>O<sub>4</sub> Thin Films Deposited via Microwave-Assisted Synthesis for Sensing Application. *J. Electron. Mater.* **2022**, *51*, 5395–5404. [[CrossRef](#)]
50. Luby, S.; Chitu, L.; Jergel, M.; Majkova, E.; Siffalovic, P.; Caricato, A.P.; Luches, A.; Martino, M.; Rella, R.; Manera, M.G. Oxide nanoparticle arrays for sensors of CO and NO<sub>2</sub> gases. *Vacuum* **2012**, *86*, 590–593. [[CrossRef](#)]
51. Rao, P.; Godbole, R.V.; Phase, D.M.; Chikate, R.C.; Bhagwat, S. Ferrite thin films: Synthesis, characterization and gas sensing properties towards LPG. *Mater. Chem. Phys.* **2015**, *149*, 333–338. [[CrossRef](#)]
52. Rathore, D.; Kurchania, R.; Pandey, R.K. Gas Sensing Properties of Size Varying CoFe<sub>2</sub>O<sub>4</sub> Nanoparticles. *IEEE Sens. J.* **2015**, *15*, 4961–4966. [[CrossRef](#)]

53. Zhang, H.-J.; Liu, L.-Z.; Zhang, X.-R.; Zhang, S.; Meng, F.-N. Microwave-assisted solvothermal synthesis of shape-controlled  $\text{CoFe}_2\text{O}_4$  nanoparticles for acetone sensor. *J. Alloys Compd.* **2019**, *788*, 1103–1112. [[CrossRef](#)]
54. Halvaei, P.; Dehghani, S.; Haghghifard, S. Low Temperature Methanol Sensors Based on Cobalt Ferrite Nanoparticles, Nanorods, and Porous Nanoparticles. *IEEE Sens. J.* **2020**, *20*, 4056–4062. [[CrossRef](#)]
55. Sun, Z.; Liu, L.; Ha, D.Z.; Pan, W. Simple synthesis of  $\text{CuFe}_2\text{O}_4$  nanoparticles as gas-sensing materials. *Sens. Actuators B* **2007**, *125*, 144–148. [[CrossRef](#)]
56. Tudorache, F.; Rezlescu, E.; Popa, P.D.; Rezlescu, N. Study of some simple ferrites as reducing gas sensors. *J. Optoelectron. Adv. Mater.* **2008**, *10*, 1889–1893.
57. Singh, S.; Yadav, B.C.; Gupta, V.D.; Dwivedi, P.K. Investigation on effects of surface morphologies on response of LPG sensor based on nanostructured copper ferrite system. *Mater. Res. Bull.* **2012**, *47*, 3538–3547. [[CrossRef](#)]
58. Abu Haija, M.; Abu-Hani, A.F.S.; Hamdan, N.; Stephen, S.; Ayesh, A.I. Characterization of  $\text{H}_2\text{S}$  gas sensor based on  $\text{CuFe}_2\text{O}_4$  nanoparticles. *J. Alloys Compd.* **2017**, *690*, 461–468. [[CrossRef](#)]
59. Abu Haija, M.; Ayesh, A.I.; Ahmed, S.; Katsiotis, M.S. Selective hydrogen gas sensor using  $\text{CuFe}_2\text{O}_4$  nanoparticle based thin film. *Appl. Surf. Sci.* **2016**, *369*, 443–447. [[CrossRef](#)]
60. Ayesh, A.I.; Abu Haija, M.; Shaheen, A.; Banat, F. Spinel ferrite nanoparticles for  $\text{H}_2\text{S}$  gas sensor. *Appl. Phys. A Mater. Sci. Process.* **2017**, *123*, 1–8. [[CrossRef](#)]
61. Liu, Y.-L.; Liu, Z.-M.; Yang, Y.; Yang, H.-F.; Shen, G.-L.; Yu, R.-Q. Simple synthesis of  $\text{MgFe}_2\text{O}_4$  nanoparticles as gas sensing materials. *Sens. Actuators B* **2005**, *107*, 600–604. [[CrossRef](#)]
62. Hankare, P.P.; Jadhav, S.D.; Sankpal, U.B.; Patil, R.P.; Sasikala, R.; Mulla, I.S. Gas sensing properties of magnesium ferrite prepared by co-precipitation method. *J. Alloys Compd.* **2009**, *488*, 270–272. [[CrossRef](#)]
63. Mukherjee, K.; Bharti, D.C.; Majumder, S.B. Combustible Gas Sensing Characteristics of Chemical Solution Synthesized Nanocrystalline Magnesium Ferrite Spinel Particles. *Trans. Indian Ceram. Soc.* **2010**, *69*, 187–192. [[CrossRef](#)]
64. Mukherjee, K.; Bharti, D.C.; Majumder, S.B. Solution synthesis and kinetic analyses of the gas sensing characteristics of magnesium ferrite particles. *Sens. Actuators B* **2010**, *146*, 91–97. [[CrossRef](#)]
65. Patil, J.Y.; Khandekar, M.S.; Mulla, I.S.; Suryavanshi, S.S. Combustion synthesis of magnesium ferrite as liquid petroleum gas (LPG) sensor: Effect of sintering temperature. *Curr. Appl. Phys.* **2012**, *12*, 319–324. [[CrossRef](#)]
66. Patil, J.Y.; Mulla, I.S.; Suryavanshi, S.S. Gas response properties of citrate gel synthesized nanocrystalline  $\text{MgFe}_2\text{O}_4$ : Effect of sintering temperature. *Mater. Res. Bull.* **2013**, *48*, 778–784. [[CrossRef](#)]
67. Godbole, R.; Rao, P.; Bhagwat, S. Magnesium ferrite nanoparticles: A rapid gas sensor for alcohol. *Mater. Res. Express* **2017**, *4*, 25032. [[CrossRef](#)]
68. Nagarajan, V.; Thayumanavan, A.  $\text{MgFe}_2\text{O}_4$  thin films for detection of ethanol and acetone vapours. *Surf. Eng.* **2018**, *34*, 711–720. [[CrossRef](#)]
69. Sumangala, T.P.; Pasquet, I.; Presmanes, L.; Thimont, Y.; Bonningue, C.; Venkataramani, N.; Prasad, S.; Baco-Carles, V.; Tailhades, P.; Barnabe, A. Effect of synthesis method and morphology on the enhanced  $\text{CO}_2$  sensing properties of magnesium ferrite  $\text{MgFe}_2\text{O}_4$ . *Ceram. Int.* **2018**, *44*, 18578–18584. [[CrossRef](#)]
70. Jaiswal, A.K.; Sikarwar, S.; Singh, S.; Dey, K.K.; Yadav, B.C.; Yadav, R.R. Fabrication of nanostructured magnesium ferrite polyhedrons and their applications in heat transfer management and gas/humidity sensors. *J. Mater. Sci. Mater. Electron.* **2020**, *31*, 80–89. [[CrossRef](#)]
71. Aono, H.; Hirazawa, H.; Naohara, T.; Maehara, T. Surface study of fine  $\text{MgFe}_2\text{O}_4$  ferrite powder prepared by chemical methods. *Appl. Surf. Sci.* **2008**, *254*, 2319–2324. [[CrossRef](#)]
72. Godbole, R.V.; Rao, P.; Alegaonkar, P.S.; Bhagwat, S. Influence of fuel to oxidizer ratio on LPG sensing performance of  $\text{MgFe}_2\text{O}_4$  nanoparticles. *Mater. Chem. Phys.* **2015**, *161*, 135–141. [[CrossRef](#)]
73. Reddy, K.M.; Satyanarayana, L.; Manorama, S.V.; Misra, R.D.K. A comparative study of the gas sensing behavior of nanostructured nickel ferrite synthesized by hydrothermal and reverse micelle techniques. *Mater. Res. Bull.* **2004**, *39*, 1491–1498. [[CrossRef](#)]
74. Lee, P.Y.; Ishizaka, K.; Suematsu, H.; Jiang, W.; Yatsui, K. Magnetic and gas sensing property of nanosized  $\text{NiFe}_2\text{O}_4$  powders synthesized by pulsed wire discharge. *J. Nanopart. Res.* **2006**, *8*, 29–35. [[CrossRef](#)]
75. Busurin, S.M.; Tsygankov, P.A.; Busurina, M.L.; Kovalev, I.D.; Boyarchenko, O.D.; Sachkova, N.V.; Sychev, A.E. Production, electrical conductivity, and gas-sensing properties of thin nickel ferrite films. *Dokl. Phys. Chem.* **2012**, *444*, 83–87. [[CrossRef](#)]
76. Sutka, A.; Stingaciu, M.; Mezinskis, G.; Lulis, A. An alternative method to modify the sensitivity of p-type  $\text{NiFe}_2\text{O}_4$  gas sensor. *J. Mater. Sci.* **2012**, *47*, 2856–2863. [[CrossRef](#)]
77. Patil, J.Y.; Nadargi, D.Y.; Gurav, J.L.; Mulla, I.S.; Suryavanshi, S.S. Synthesis of glycine combusted  $\text{NiFe}_2\text{O}_4$  spinel ferrite: A highly versatile gas sensor. *Mater. Lett.* **2014**, *124*, 144–147. [[CrossRef](#)]
78. Ghosh, P.; Mukherjee, A.; Fu, M.; Chattopadhyay, S.; Mitra, P. Influence of particle size on  $\text{H}_2$  and  $\text{H}_2\text{S}$  sensing characteristics of nanocrystalline nickel ferrite. *Phys. E* **2015**, *74*, 570–575. [[CrossRef](#)]
79. Singh, A.; Singh, A.; Singh, S.; Tandon, P.; Yadav, B.C. Preparation and characterization of nanocrystalline nickel ferrite thin films for development of a gas sensor at room temperature. *J. Mater. Sci. Mater. Electron.* **2016**, *27*, 8047–8054. [[CrossRef](#)]
80. Kashyap, R.; Kumar, R.; Devi, S.; Kumar, M.; Tyagi, S.; Kumar, D. Ammonia gas sensing performance of nickel ferrite nanoparticles. *Mater. Res. Express* **2019**, *6*, 1150d3. [[CrossRef](#)]

81. Jia, C.; Zhang, Y.; Kong, Q.; Wang, Q.; Chen, G.; Guam, H.; Dong, C. Soft-template synthesis of mesoporous NiFe<sub>2</sub>O<sub>4</sub> for highly sensitive acetone detection. *J. Mater. Sci. Mater. Electron.* **2020**, *31*, 6000–6007. [[CrossRef](#)]
82. Chaudhari, P.R.; Gaikwad, V.M.; Acharya, S.A. Rapid microwave-assisted combustion route for production of MFe<sub>2</sub>O<sub>4</sub> (M = Zn, Ni, Co) nanoferrites for gas sensors view point. *Ferroelectrics* **2022**, *587*, 76–83. [[CrossRef](#)]
83. Kumar, A.; Kashyap, R.; Kumar, R.; Singh, R.; Prasad, B.; Kumar, M.; Kumar, D. Experimental and Numerical Modelling of a Nanostructured Nickel Ferrite-Based Ammonia Gas Sensor. *J. Electron. Mater.* **2022**, *51*, 4040–4053. [[CrossRef](#)]
84. Rezaeipour, A.; Dehghani, S.; Hoghoghifard, S. VOC Sensors Based on Nanoparticles and Nanorods of Nickel Ferrite. *IEEE Sens. J.* **2022**, *22*, 16464–16471. [[CrossRef](#)]
85. Niu, X.; Du, W.; Du, W. Preparation and gas sensing properties of ZnM<sub>2</sub>O<sub>4</sub> (M = Fe, Co, Cr). *Sens. Actuators B* **2004**, *99*, 405–409. [[CrossRef](#)]
86. Chu, X.; Jiang, D.; Zheng, C. The gas-sensing properties of thick film sensors based on nano-ZnFe<sub>2</sub>O<sub>4</sub> prepared by hydrothermal method. *Mater. Sci. Eng. B* **2006**, *129*, 150–153. [[CrossRef](#)]
87. Darshane, S.L.; Deshmukh, R.G.; Suryavanshi, S.S.; Mulla, I.S. Gas-sensing properties of zinc ferrite nanoparticles synthesized by the molten-salt route. *J. Am. Ceram. Soc.* **2008**, *91*, 2724–2726. [[CrossRef](#)]
88. Karpova, S.S.; Moshnikov, V.A.; Mjakin, S.V.; Kolovangina, E.S. Surface functional composition and sensor properties of ZnO, Fe<sub>2</sub>O<sub>3</sub>, and ZnFe<sub>2</sub>O<sub>4</sub>. *Semiconductors* **2013**, *47*, 392–395. [[CrossRef](#)]
89. Patil, J.Y.; Nadargi, D.Y.; Gurav, J.L.; Mulla, I.S.; Suryavanshi, S.S. Glycine combusted ZnFe<sub>2</sub>O<sub>4</sub> gas sensor: Evaluation of structural, morphological and gas response properties. *Ceram. Int.* **2014**, *40*, 10607–10613. [[CrossRef](#)]
90. Dalawai, S.P.; Shinde, T.J.; Gadkari, A.B.; Vasambekar, P.N. Ni-Zn ferrite thick film gas sensors. *J. Mater. Sci. Mater. Electron.* **2015**, *26*, 9016–9025. [[CrossRef](#)]
91. Tyagi, S.; Batra, N.; Paul, A.K. Influence of Temperature on Reducing Gas Sensing Performance of Nanocrystalline Zinc Ferrite. *Trans. Indian Inst. Met.* **2015**, *68*, 707–713. [[CrossRef](#)]
92. Zhang, J.; Song, J.-M.; Niu, H.-L.; Mao, C.-J.; Zhang, S.-Y.; Shen, Y.-H. ZnFe<sub>2</sub>O<sub>4</sub> nanoparticles: Synthesis, characterization, and enhanced gas sensing property for acetone. *Sens. Actuators B* **2015**, *221*, 55–62. [[CrossRef](#)]
93. Cao, Y.; Qin, H.; Niu, X.; Jia, D. Simple solid-state chemical synthesis and gas-sensing properties of spinel ferrite materials with different morphologies. *Ceram. Int.* **2016**, *42*, 10697–10703. [[CrossRef](#)]
94. Ghosh, P.; Das, M.R.; Mitra, P. Influence of particle size on H<sub>2</sub> and H<sub>2</sub>S sensing characteristics of nanocrystalline zinc ferrite. *Indian J. Phys.* **2016**, *90*, 1367–1373. [[CrossRef](#)]
95. Wu, J.; Gao, D.; Sun, T.; Bi, J.; Zhao, Y.; Ning, Z.; Fan, G.; Xie, Z. Highly selective gas sensing properties of partially inversed spinel zinc ferrite towards H<sub>2</sub>S. *Sens. Actuators B* **2016**, *235*, 258–262. [[CrossRef](#)]
96. You, J.; Chen, X.; Zheng, B.; Geng, X.; Zhang, C. Suspension Plasma-Sprayed ZnFe<sub>2</sub>O<sub>4</sub> Nanostructured Coatings for ppm-Level Acetone Detection. *J. Therm. Spray Technol.* **2017**, *26*, 728–734. [[CrossRef](#)]
97. Hernandez, P.T.; Kuznetsov, M.V.; Morozov, I.G.; Parkin, I.P. Application of levitation jet synthesized nickel-based nanoparticles for gas sensing. *Mater. Sci. Eng. B* **2019**, *244*, 81–92. [[CrossRef](#)]
98. Khurshid, R.; Ali, F.; Afzal, A.; Ali, Z.; Qureshi, M.T. Polyol-Mediated Coprecipitation and Aminosilane Grafting of Superparamagnetic, Spinel ZnFe<sub>2</sub>O<sub>4</sub> Nanoparticles for Room-Temperature Ethanol Sensors. *J. Electrochem. Soc.* **2019**, *166*, B258–B265. [[CrossRef](#)]
99. Li, K.; Luo, Y.; Liu, B.; Gao, L.; Duan, G. High-performance NO<sub>2</sub>-gas sensing of ultrasmall ZnFe<sub>2</sub>O<sub>4</sub> nanoparticles based on surface charge transfer. *J. Mater. Chem. A* **2019**, *7*, 5539–5551. [[CrossRef](#)]
100. Peng, S.; Wang, Z.; Liu, R.; Bi, J.; Wu, J. Controlled oxygen vacancies of ZnFe<sub>2</sub>O<sub>4</sub> with superior gas sensing properties prepared via a facile one-step self-catalyzed treatment. *Sens. Actuators B* **2019**, *288*, 649–655. [[CrossRef](#)]
101. Nemifulwi, M.I.; Swart, H.C.; Mdlalose, W.B.; Mhlongo, G.H. Size-tunable ferromagnetic ZnFe<sub>2</sub>O<sub>4</sub> nanoparticles and their ethanol detection capabilities. *Appl. Surf. Sci.* **2020**, *508*, 144863. [[CrossRef](#)]
102. Jha, R.K.; Nanda, A.; Sai, R.; Kishore, K.; Yadav, A.; Kahmei, R.D.R.; Bhat, N. Development of a Ferrite Film Based Solid State Sensor System for Ultra Low Concentration Hydrogen Sulfide Gas Detection. *IEEE Sens. J.* **2022**, *22*, 8402–8409. [[CrossRef](#)]
103. Ishigami, H.; Kawaguchi, T.; Sakamoto, N.; Che, S.; Koshida, N.; Shinozaki, K.; Suzuki, H.; Wakiya, N. Dynamic Aurora PLD with Si and porous Si to prepare ZnFe<sub>2</sub>O<sub>4</sub> Thin films for liquefied petroleum gas sensing. *J. Ceram. Soc. Jpn.* **2020**, *128*, 457–463. [[CrossRef](#)]
104. Mukherjee, K.; Majumder, S.B. Analyses of response and recovery kinetics of zinc ferrite as hydrogen gas sensor. *J. Appl. Phys.* **2009**, *106*, 064912. [[CrossRef](#)]
105. Cao, Y.; Jia, D.; Hu, P.; Wang, R. One-step room-temperature solid-phase synthesis of ZnFe<sub>2</sub>O<sub>4</sub> nanomaterials and its excellent gas-sensing property. *Ceram. Int.* **2013**, *39*, 2989–2994. [[CrossRef](#)]
106. Jeseentharani, V.; George, M.; Jeyaraj, B.; Dayalan, A.; Nagaraja, K.S. Synthesis of metal ferrite (MFe<sub>2</sub>O<sub>4</sub>, M = Co, Cu, Mg, Ni, Zn) nanoparticles as humidity sensor materials. *J. Exp. Nanosci.* **2013**, *8*, 358–370. [[CrossRef](#)]
107. Sutka, A.; Mezinskis, G.; Zamovskis, M.; Jakovlevs, D.; Pavlovskaja, I. Monophasic ZnFe<sub>2</sub>O<sub>4</sub> synthesis from a xerogel layer by auto combustion. *Ceram. Int.* **2013**, *39*, 8499–8502. [[CrossRef](#)]
108. Srivastava, R.; Yadav, B.C. Nanostructured ZnFe<sub>2</sub>O<sub>4</sub> thick film as room temperature liquefied petroleum gas sensor. *J. Exp. Nanosci.* **2015**, *10*, 703–717. [[CrossRef](#)]

109. Raut, S.D.; Awasarmol, V.V.; Gghule, B.; Shaikh, S.F.; Gore, S.K.; Sharma, R.P.; Pawar, P.P.; Mane, R.S. gamma-irradiation induced zinc ferrites and their enhanced room-temperature ammonia gas sensing properties. *Mater. Res. Express* **2018**, *5*, 35702. [[CrossRef](#)]
110. Zhang, H.-J.; Meng, F.-N.; Liu, L.-Z.; Chen, Y.-J.; Wang, P.-J. Highly sensitive H<sub>2</sub>S sensor based on solvothermally prepared spinel ZnFe<sub>2</sub>O<sub>4</sub> nanoparticles. *J. Alloys Compd.* **2018**, *764*, 147–154. [[CrossRef](#)]
111. Sun, K.-M.; Song, X.-Z.; Wang, X.-F.; Li, X.; Tan, Z. Annealing temperature-dependent porous ZnFe<sub>2</sub>O<sub>4</sub> olives derived from bimetallic organic frameworks for high-performance ethanol gas sensing. *Mater. Chem. Phys.* **2020**, *241*, 122379. [[CrossRef](#)]
112. Prasad, P.D.; Hemalatha, J. Enhanced magnetic properties of highly crystalline cobalt ferrite fibers and their application as gas sensors. *J. Magn. Magn. Mater.* **2019**, *484*, 225–233. [[CrossRef](#)]
113. Zhang, L.; Jiao, W. The effect of microstructure on the gas properties of NiFe<sub>2</sub>O<sub>4</sub> sensors: Nanotube and nanoparticle. *Sens. Actuators B* **2015**, *216*, 293–297. [[CrossRef](#)]
114. Chaudhuri, A.; Mandal, K.; Pati, S.P.; Das, D. High performance gas sensing based on nano rods of nickel ferrite fabricated by a facile solvothermal route. *Mater. Res. Express* **2018**, *5*, 36202. [[CrossRef](#)]
115. Wang, X.-F.; Sun, K.-M.; Li, S.-J.; Song, X.-Z.; Cheng, L.; Ma, W. Porous Javelin-Like NiFe<sub>2</sub>O<sub>4</sub> Nanorods as n-Propanol Sensor with Ultrahigh-Performance. *Chemistryselect* **2018**, *3*, 12871–12877. [[CrossRef](#)]
116. Chu, X.; Jiang, D.; Zheng, C. The preparation and gas-sensing properties of NiFe<sub>2</sub>O<sub>4</sub> nanocubes and nanorods. *Sens. Actuators B* **2007**, *123*, 793–797. [[CrossRef](#)]
117. Zhang, Y.; Jia, C.; Wang, Q.; Kong, Q.; Chen, G.; Guan, H.; Dong, C. Highly Sensitive and Selective Toluene Sensor of Bimetallic Ni/Fe-MOFs Derived Porous NiFe<sub>2</sub>O<sub>4</sub> Nanorods. *Ind. Eng. Chem. Res.* **2019**, *58*, 9450–9457. [[CrossRef](#)]
118. Zhang, G.; Li, C.; Cheng, F.; Chen, J. ZnFe<sub>2</sub>O<sub>4</sub> tubes: Synthesis and application to gas sensors with high sensitivity and low-energy consumption. *Sens. Actuators B* **2007**, *120*, 403–410. [[CrossRef](#)]
119. Zhu, H.; Gu, X.; Zuo, D.; Wang, Z.; Wang, N.; Yao, K. Microemulsion-based synthesis of porous zinc ferrite nanorods and its application in a room-temperature ethanol sensor. *Nanotechnology* **2008**, *19*, 405503. [[CrossRef](#)]
120. Singh, S.; Singh, A.; Yadav, R.R.; Tandon, P. Growth of zinc ferrite aligned nanorods for liquefied petroleum gas sensing. *Mater. Lett.* **2014**, *131*, 31–34. [[CrossRef](#)]
121. Singh, A.; Singh, A.; Singh, S.; Tandon, P.; Yadav, B.C.; Yadav, R.R. Synthesis, characterization and performance of zinc ferrite nanorods for room temperature sensing applications. *J. Alloys Compd.* **2015**, *618*, 475–483. [[CrossRef](#)]
122. Li, L.; Tan, J.; Dun, M.; Huang, X. Porous ZnFe<sub>2</sub>O<sub>4</sub> nanorods with net-worked nanostructure for highly sensor response and fast response acetone gas sensor. *Sens. Actuators B* **2017**, *248*, 85–91. [[CrossRef](#)]
123. Nguyen Van, H.; Chu Manh, H.; Nguyen Duc, H.; Nguyen Van, D.; Nguyen Van, H. Facile on-chip electrospinning of ZnFe<sub>2</sub>O<sub>4</sub> nanofiber sensors with excellent sensing performance to H<sub>2</sub>S down ppb level. *J. Hazard. Mater.* **2018**, *360*, 6–16. [[CrossRef](#)]
124. Chu, X.; Gan, Z.; Bai, L.; Dong, Y.; Rumyantseva, M.N. Acetone-sensing Properties of ZnFe<sub>2</sub>O<sub>4</sub> Nanofibers Prepared via Electrospinning Method. *Rare Metal Mat. Eng.* **2019**, *48*, 1371–1379.
125. Singh, S.; Yadav, B.C.; Prakash, R.; Bajaj, B.; Lee, J.R. Synthesis of nanorods and mixed shaped copper ferrite and their applications as liquefied petroleum gas sensor. *Appl. Surf. Sci.* **2011**, *257*, 10763–10770. [[CrossRef](#)]
126. Singh, A.; Singh, A.; Singh, S.; Tandon, P. Fabrication of copper ferrite porous hierarchical nanostructures for an efficient liquefied petroleum gas sensor. *Sens. Actuators B* **2017**, *244*, 806–814. [[CrossRef](#)]
127. Patil, J.; Nadargi, D.; Mulla, I.S.; Suryavanshi, S.S. Spinel MgFe<sub>2</sub>O<sub>4</sub> thick films: A colloidal approach for developing gas sensors. *Mater. Lett.* **2018**, *213*, 27–30. [[CrossRef](#)]
128. Sutka, A.; Zavickis, J.; Mezinskis, G.; Jakovlevs, D.; Barloti, J. Ethanol monitoring by ZnFe<sub>2</sub>O<sub>4</sub> thin film obtained by spray pyrolysis. *Sens. Actuators B* **2013**, *176*, 330–334. [[CrossRef](#)]
129. Gao, X.; Sun, Y.; Zhu, C.; Li, C.; Ouyang, Q.; Chen, Y. Highly sensitive and selective H<sub>2</sub>S sensor based on porous ZnFe<sub>2</sub>O<sub>4</sub> nanosheets. *Sens. Actuators B* **2017**, *246*, 662–672. [[CrossRef](#)]
130. Madake, S.B.; Hattali, M.R.; Rajpure, K.Y. Porogen induced formation of mesoporous zinc ferrite thin films and their chemiresistive properties. *Mater. Sci. Eng. B* **2021**, *263*, 114867. [[CrossRef](#)]
131. Xu, Y.; Sun, D.; Hao, H.; Gao, D.; Sun, Y. Non-stoichiometric Co(II), Ni(II), Zn(II)-ferrite nanospheres: Size controllable synthesis, excellent gas-sensing and magnetic properties. *RSC Adv.* **2016**, *6*, 98994–99002. [[CrossRef](#)]
132. Wang, L.; Wang, Y.; Tian, H.; Qiao, L.; Zeng, Y. Enhanced ammonia detection using wrinkled porous CoFe<sub>2</sub>O<sub>4</sub> double-shelled spheres prepared by a thermally driven contraction process. *Sens. Actuators B* **2020**, *314*, 128085. [[CrossRef](#)]
133. Wu, K.-D.; Xu, J.-Y.; Debliquy, M.; Zhang, C. Synthesis and NH<sub>3</sub>/TMA sensing properties of CuFe<sub>2</sub>O<sub>4</sub> hollow microspheres at low working temperature. *Rare Met.* **2020**, *40*, 1768–1777. [[CrossRef](#)]
134. Yang, X.; Zhang, S.; Yu, Q.; Sun, P.; Liu, F.; Lu, H.; Yan, X.; Zhou, X.; Liang, X.; Gao, Y.; et al. Solvothermal synthesis of porous CuFe<sub>2</sub>O<sub>4</sub> nanospheres for high performance acetone sensor. *Sens. Actuators B* **2018**, *270*, 538–544. [[CrossRef](#)]
135. Lai, X.; Cao, K.; Shen, G.; Xue, P.; Wang, D.; Hu, F.; Zhang, J.; Yang, Q.; Wang, X. Ordered mesoporous NiFe<sub>2</sub>O<sub>4</sub> with ultrathin framework for low-ppb toluene sensing. *Sci. Bull.* **2018**, *63*, 187–193. [[CrossRef](#)] [[PubMed](#)]
136. Ma, Y.; Lu, Y.; Gou, H.; Zhang, W.; Yan, S.; Xu, X. Octahedral NiFe<sub>2</sub>O<sub>4</sub> for high-performance gas sensor with low working temperature. *Ceram. Int.* **2018**, *44*, 2620–2625. [[CrossRef](#)]
137. Song, X.-Z.; Meng, Y.-L.; Chen, X.; Sun, K.-M.; Wang, X.-F. Hollow NiFe<sub>2</sub>O<sub>4</sub> hexagonal biyramids for high-performance n-propanol sensing at low temperature. *New J. Chem.* **2018**, *42*, 14071–14074. [[CrossRef](#)]

138. Song, X.-Z.; Sun, F.-F.; Dai, S.-T.; Lin, X.; Sun, K.-M.; Wang, X.-F. Hollow NiFe<sub>2</sub>O<sub>4</sub> microspindles derived from Ni/Fe bimetallic MOFs for highly sensitive acetone sensing at low operating temperatures. *Inorg. Chem. Front.* **2018**, *5*, 1107–1114. [[CrossRef](#)]
139. Zhou, T.; Zhang, T.; Zeng, Y.; Zhang, R.; Lou, Z.; Deng, J.; Wang, L. Structure-driven efficient NiFe<sub>2</sub>O<sub>4</sub> materials for ultra-fast response electronic sensing platform. *Sens. Actuators B* **2018**, *255*, 1436–1444. [[CrossRef](#)]
140. Zhang, S.; Jiang, W.; Li, Y.; Yang, X.; Sun, P.; Liu, F.; Yan, X.; Gao, Y.; Liang, X.; Ma, J.; et al. Highly-sensitivity acetone sensors based on spinel-type oxide (NiFe<sub>2</sub>O<sub>4</sub>) through optimization of porous structure. *Sens. Actuators B* **2019**, *291*, 266–274. [[CrossRef](#)]
141. Zhang, Y.; Jia, C.; Wang, Q.; Kong, Q.; Chen, G.; Guan, H.; Dong, C. MOFs-Derived Porous NiFe<sub>2</sub>O<sub>4</sub> Nano-Octahedrons with Hollow Interiors for an Excellent Toluene Gas Sensor. *Nanomaterials* **2019**, *9*, 1059–1077. [[CrossRef](#)] [[PubMed](#)]
142. Zhai, C.; Zhang, H.; Du, L.; Wang, D.; Xing, D.; Zhang, M. Nickel/iron-based bimetallic MOF-derived nickel ferrite materials for triethylamine sensing. *Crystengcomm* **2020**, *22*, 1286–1293. [[CrossRef](#)]
143. Wang, X.F.; Li, X.; Zhang, G.Z.; Wang, Z.H.; Song, X.Z.; Tan, Z.Q. Surface Structure Engineering of Nanosheet-Assembled NiFe<sub>2</sub>O<sub>4</sub> Fluffy Flowers for Gas Sensing. *Nanomaterials* **2021**, *11*, 8. [[CrossRef](#)] [[PubMed](#)]
144. Zhang, Y.-L.; Jia, C.-W.; Tian, R.-N.; Guan, H.-T.; Chen, G.; Dong, C.-J. Hierarchical flower-like NiFe<sub>2</sub>O<sub>4</sub> with core-shell structure for excellent toluene detection. *Rare Met.* **2020**, *40*, 1578–1587. [[CrossRef](#)]
145. Liu, N.; Wang, X.-F.; Zhang, G.; Liang, H.; Li, T.; Zhao, Y.; Zhang, T.; Tan, Z.; Song, X.-Z. Metal-Organic Framework-Derived Porous NiFe<sub>2</sub>O<sub>4</sub> Nanoboxes for Ethyl Acetate Gas Sensors. *ACS Appl. Nano Mater.* **2022**, *5*, 14320–14327. [[CrossRef](#)]
146. Li, Z.; Lai, X.; Wang, H.; Mao, D.; Xing, C.; Wang, D. General Synthesis of Homogeneous Hollow Core-Shell Ferrite Microspheres. *J. Phys. Chem. C* **2009**, *113*, 2792–2797. [[CrossRef](#)]
147. Zhou, X.; Liu, J.; Wang, C.; Sun, P.; Hu, X.; Li, X.; Shimano, K.; Yamazoe, N.; Lu, G. Highly sensitive acetone gas sensor based on porous ZnFe<sub>2</sub>O<sub>4</sub> nanospheres. *Sens. Actuators B* **2015**, *206*, 577–583. [[CrossRef](#)]
148. Zhou, X.; Wang, B.; Sun, H.; Wang, C.; Sun, P.; Li, X.; Hu, X.; Lu, G. Template-free synthesis of hierarchical ZnFe<sub>2</sub>O<sub>4</sub> yolk-shell microspheres for high-sensitivity acetone sensors. *Nanoscale* **2016**, *8*, 5446–5453. [[CrossRef](#)]
149. Zhou, X.; Li, X.; Sun, H.; Sun, P.; Liang, X.; Liu, F.; Hu, X.; Lu, G. Nanosheet-Assembled ZnFe<sub>2</sub>O<sub>4</sub> Hollow Microspheres for High-Sensitive Acetone Sensor. *ACS Appl. Mater. Interfaces* **2015**, *7*, 15414–15421. [[CrossRef](#)]
150. Sahoo, R.; Santra, S.; Ray, C.; Pal, A.; Negishi, Y.; Ray, S.K.; Pal, T. Hierarchical growth of ZnFe<sub>2</sub>O<sub>4</sub> for sensing applications. *New J. Chem.* **2016**, *40*, 1861–1871. [[CrossRef](#)]
151. Dong, C.; Liu, X.; Xiao, X.; Du, S.; Wang, Y. Monodisperse ZnFe<sub>2</sub>O<sub>4</sub> nanospheres synthesized by a nonaqueous route for a highly selective low-ppm-level toluene gas sensor. *Sens. Actuators B* **2017**, *239*, 1231–1236. [[CrossRef](#)]
152. Liu, T.; Liu, J.; Liu, Q.; Li, R.; Zhang, H.; Jing, X.; Wang, J. Shape-controlled fabrication and enhanced gas sensing properties of uniform sphere-like ZnFe<sub>2</sub>O<sub>4</sub> hierarchical architectures. *Sens. Actuators B* **2017**, *250*, 111–120. [[CrossRef](#)]
153. Qu, F.; Shang, W.; Thomas, T.; Ruan, S.; Yang, M. Self-template derived ZnFe<sub>2</sub>O<sub>4</sub> double-shell microspheres for chemresistive gas sensing. *Sens. Actuators B* **2018**, *265*, 625–631. [[CrossRef](#)]
154. Yang, H.; Bai, X.; Hao, P.; Tian, J.; Bo, Y.; Wang, X.; Liu, H. A simple gas sensor based on zinc ferrite hollow spheres: Highly sensitivity, excellent selectivity and long-term stability. *Sens. Actuators B* **2019**, *280*, 34–40. [[CrossRef](#)]
155. Mukherjee, K.; Majumder, S.B. Synthesis of embedded and isolated Mg<sub>0.5</sub>Zn<sub>0.5</sub>Fe<sub>2</sub>O<sub>4</sub> nano-tubes and investigation on their anomalous gas sensing characteristics. *Sens. Actuators B* **2013**, *177*, 55–63. [[CrossRef](#)]
156. Patil, J.Y.; Nadargi, D.Y.; Mulla, I.S.; Suryavanshi, S.S. Cerium doped MgFe<sub>2</sub>O<sub>4</sub> nanocomposites: Highly sensitive and fast response-recoverable acetone gas sensor. *Heliyon* **2019**, *5*, e01489. [[CrossRef](#)]
157. Mugutkar, A.B.; Gore, S.K.; Mane, R.S.; Patange, S.M.; Jadhav, S.S.; Shaikh, S.F.; Al-Enizi, A.M.; Nafady, A.; Thamer, B.M.; Ubaidullah, M. Structural modifications in Co-Zn nanoferrites by Gd substitution triggering to dielectric and gas sensing applications. *J. Alloys Compd.* **2020**, *844*, 11. [[CrossRef](#)]
158. Rao, P.; Godbole, R.V.; Bhagwat, S. Nanocrystalline Pd:NiFe<sub>2</sub>O<sub>4</sub> thin films: A selective ethanol gas sensor. *J. Magn. Magn. Mater.* **2016**, *416*, 292–298. [[CrossRef](#)]
159. George, J.; Abraham, K.E.; Thomas, K.J. Influence of zinc on the multifunctional properties of ferrites M<sub>1-x</sub>Zn<sub>x</sub>Fe<sub>2</sub>O<sub>4</sub> (M = Cu, Mg, Ni, x = 0, 0.35). *J. Magn. Magn. Mater.* **2022**, *546*, 168904. [[CrossRef](#)]
160. Sutka, A.; Mezinskis, G.; Lusiš, A.; Stingaci, M. Gas sensing properties of Zn-doped p-type nickel ferrite. *Sens. Actuators B* **2012**, *171*, 354–360. [[CrossRef](#)]
161. Singh, A.; Singh, S.; Joshi, B.D.; Shukla, A.; Yadav, B.C.; Tandon, P. Synthesis, characterization, magnetic properties and gas sensing applications of Zn<sub>x</sub>Cu<sub>1-x</sub>Fe<sub>2</sub>O<sub>4</sub> (0.0 ≤ x ≤ 0.8) nanocomposites. *Mater. Sci. Semicond. Process.* **2014**, *27*, 934–949. [[CrossRef](#)]
162. Bodade, A.B.; Bodade, A.B.; Wankhade, H.G.; Chaudhari, G.N.; Kothari, D.C. Conduction mechanism and gas sensing properties of CoFe<sub>2</sub>O<sub>4</sub> nanocomposite thick films for H<sub>2</sub>S gas. *Talanta* **2012**, *89*, 183–188. [[CrossRef](#)]
163. Srinivas, C.; Ranjith Kumar, E.; Tirupanyam, B.V.; Singh Meena, S.; Bhatt, P.; Prajapat, C.L.; Chandrasekhar Rao, T.V.; Sastry, D.L. Study of magnetic behavior in co-precipitated Ni-Zn ferrite nanoparticles and their potential use for gas sensor applications. *J. Magn. Magn. Mater.* **2020**, *502*, 166534. [[CrossRef](#)]
164. Wu, S.; Li, X.; Xu, Y.; Wu, J.; Wang, Z.; Han, Y.; Zhang, X. Hierarchical spinel Ni<sub>x</sub>Co<sub>1-x</sub>Fe<sub>2</sub>O<sub>4</sub> microcubes derived from Fe-based MOF for high-sensitive acetone sensor. *Ceram. Int.* **2018**, *44*, 19390–19396. [[CrossRef](#)]
165. Rezlescu, N.; Doroftei, C.; Rezlescu, E.; Popa, P.D. The influence of Sn<sup>4+</sup> and/or Mo<sup>6+</sup> ions on the structure, electrical and gas sensing properties of Mg-ferrite. *Phys. Status Solidi A-Appl. Mater. Sci.* **2006**, *203*, 306–316. [[CrossRef](#)]

166. Kadu, A.V.; Jagtap, S.V.; Chaudhari, G.N. Studies on the preparation and ethanol gas sensing properties of spinel  $\text{Zn}_{0.6}\text{Mn}_{0.4}\text{Fe}_2\text{O}_4$  nanomaterials. *Curr. Appl. Phys.* **2009**, *9*, 1246–1251. [[CrossRef](#)]
167. Kapse, V.D.; Ghosh, S.A.; Raghuvanshi, F.C.; Kapse, S.D. Nanocrystalline spinel  $\text{Ni}_{0.6}\text{Zn}_{0.4}\text{Fe}_2\text{O}_4$ : A novel material for  $\text{H}_2\text{S}$  sensing. *Mater. Chem. Phys.* **2009**, *113*, 638–644. [[CrossRef](#)]
168. Kazin, A.P.; Rummyantseva, M.N.; Prusakov, V.E.; Suzdalev, I.P.; Gaskov, A.M. Nanocrystalline ferrites  $\text{Ni}_x\text{Zn}_{1-x}\text{Fe}_2\text{O}_4$ : Influence of cation distribution on acidic and gas sensing properties. *J. Solid State Chem.* **2011**, *184*, 2799–2805. [[CrossRef](#)]
169. Muthurani, S.; Balaji, M.; Gautam, S.; Chae, K.H.; Song, J.H.; Padiyan, D.P.; Asokan, K. Magnetic and Humidity-Sensing Properties of Nanostructured  $\text{Cu}_x\text{Co}_{1-x}\text{Fe}_2\text{O}_4$  Synthesized via Autocombustion. *J. Nanosci. Nanotechnol.* **2011**, *11*, 5850–5855. [[CrossRef](#)]
170. Tang, Y.; Wang, X.; Zhang, Q.; Li, Y.; Wang, H. Solvothermal synthesis of  $\text{Co}_{1-x}\text{Ni}_x\text{Fe}_2\text{O}_4$  nanoparticles and its application in ammonia vapors detection. *Prog. Nat. Sci. Mater. Int.* **2012**, *22*, 53–58. [[CrossRef](#)]
171. Koseoglu, Y.; Aldemir, I.; Bayansal, F.; Kahraman, S.; Cetinkara, H.A. Synthesis, characterization and humidity sensing properties of  $\text{Mn}_{0.2}\text{Ni}_{0.8}\text{Fe}_2\text{O}_4$  nanoparticles. *Mater. Chem. Phys.* **2013**, *139*, 789–793. [[CrossRef](#)]
172. Karmakar, M.; Das, P.; Pal, M.; Mondal, B.; Majumder, S.B.; Mukherjee, K. Acetone and ethanol sensing characteristics of magnesium zinc ferrite nano-particulate chemi-resistive sensor. *J. Mater. Sci.* **2014**, *49*, 5766–5771. [[CrossRef](#)]
173. Kumar, E.R.; Jayaprakash, R.; Devi, G.S.; Reddy, P.S.P. Magnetic, dielectric and sensing properties of manganese substituted copper ferrite nanoparticles. *J. Magn. Magn. Mater.* **2014**, *355*, 87–92. [[CrossRef](#)]
174. Kumar, E.R.; Jayaprakash, R.; Devi, G.S.; Reddy, P.S.P. Synthesis of Mn substituted  $\text{CuFe}_2\text{O}_4$  nanoparticles for liquefied petroleum gas sensor applications. *Sens. Actuators B* **2014**, *191*, 186–191. [[CrossRef](#)]
175. Zohrabi, Y.; Ghazi, M.E.; Izadifard, M. The Gas-Sensing Properties of Ni-Zn Ferrite ( $\text{Ni}_{0.6}\text{Zn}_{0.4}\text{Fe}_2\text{O}_4$ ) Nanoparticles Prepared by the Microwave Method. *Chin. J. Phys.* **2015**, *53*, 120801. [[CrossRef](#)]
176. Joshi, S.; Kamble, V.B.; Kumar, M.; Umarji, A.M.; Srivastava, G. Nickel substitution induced effects on gas sensing properties of cobalt ferrite nanoparticles. *J. Alloys Compd.* **2016**, *654*, 460–466. [[CrossRef](#)]
177. Kumar, E.R.; Kamzin, A.S.; Janani, K. Effect of annealing on particle size, microstructure and gas sensing properties of Mn substituted  $\text{CoFe}_2\text{O}_4$  nanoparticles. *J. Magn. Magn. Mater.* **2016**, *417*, 122–129. [[CrossRef](#)]
178. Rao, P.; Godbole, R.V.; Bhagwat, S. Copper doped nickel ferrite nano-crystalline thin films: A potential gas sensor towards reducing gases. *Mater. Chem. Phys.* **2016**, *171*, 260–266. [[CrossRef](#)]
179. Anggraini, S.A.; Fujio, Y.; Ikeda, H.; Miura, N. YSZ-based sensor using Cr-Fe-based spinel-oxide electrodes for selective detection of CO. *Anal. Chim. Acta* **2017**, *982*, 176–184. [[CrossRef](#)] [[PubMed](#)]
180. Kamzin, A.S.; Kumar, E.R.; Ramadevi, P.; Selvakumar, C. The properties of Mn-Cu $\text{Fe}_2\text{O}_4$  spinel ferrite nanoparticles under various synthesis conditions. *Phys. Solid State* **2017**, *59*, 1841–1851. [[CrossRef](#)]
181. Kumar, E.R.; Srinivas, C.; Seehra, M.S.; Deepty, M.; Pradeep, I.; Kamzin, A.S.; Mehar, M.V.K.; Mohan, N.K. Particle size dependence of the magnetic, dielectric and gas sensing properties of Co substituted  $\text{NiFe}_2\text{O}_4$  nanoparticles. *Sens. Actuators Ba-Phys.* **2018**, *279*, 10–16. [[CrossRef](#)]
182. Manikandan, V.; Li, X.; Mane, R.S.; Chandrasekaran, J. Room Temperature Gas Sensing Properties of Sn-Substituted Nickel Ferrite ( $\text{NiFe}_2\text{O}_4$ ) Thin Film Sensors Prepared by Chemical Co-Precipitation Method. *J. Electron. Mater.* **2018**, *47*, 3403–3408. [[CrossRef](#)]
183. Manikandan, V.; Singh, M.; Yadav, B.C.; Denardin, J.C. Fabrication of lithium substituted copper ferrite ( $\text{Li-CuFe}_2\text{O}_4$ ) thin film as an efficient gas sensor at room temperature. *J. Sci. Adv. Mater. Devices* **2018**, *3*, 145–150. [[CrossRef](#)]
184. Manikandan, V.; Singh, M.; Yadav, B.C.; Vigneselvan, S. Room-Temperature Gas Sensing Properties of Nanocrystalline-Structured Indium-Substituted Copper Ferrite Thin Film. *J. Electron. Mater.* **2018**, *47*, 6366–6372. [[CrossRef](#)]
185. Koli, P.B.; Kapadnis, K.H.; Deshpande, U.G. Nanocrystalline-modified nickel ferrite films: An effective sensor for industrial and environmental gas pollutant detection. *J. Nanostruct. Chem.* **2019**, *9*, 95–110. [[CrossRef](#)]
186. Mutkule, S.U.; Tehare, K.K.; Gore, S.K.; Gunturu, K.C.; Mane, R.S. Ambient temperature operable Bi-Co ferrite  $\text{NO}_2$  sensors with high sensitivity and selectivity. *Mater. Res. Bull.* **2019**, *115*, 150–158. [[CrossRef](#)]
187. Zhang, W.; Shen, Y.; Zhang, J.; Bi, H.; Zhao, S.; Zhou, P.; Han, C.; Wei, D.; Cheng, N. Low-temperature  $\text{H}_2\text{S}$  sensing performance of Cu-doped  $\text{ZnFe}_2\text{O}_4$  nanoparticles with spinel structure. *Appl. Surf. Sci.* **2019**, *470*, 581–590. [[CrossRef](#)]
188. Zou, Y.; Wang, H.; Yang, R.; Lai, X.; Wan, J.; Lin, G.; Liu, D. Controlled synthesis and enhanced toluene-sensing properties of mesoporous  $\text{Ni}_x\text{Co}_{1-x}\text{Fe}_2\text{O}_4$  nanostructured microspheres with tunable composite. *Sens. Actuators B* **2019**, *280*, 227–234. [[CrossRef](#)]
189. Abu Haija, M.; Chamakh, M.; Othman, I.; Banat, F.; Ayes, A.I. Fabrication of  $\text{H}_2\text{S}$  gas sensors using  $\text{Zn}_x\text{Cu}_{1-x}\text{Fe}_2\text{O}_4$  nanoparticles. *Appl. Phys. A Mater. Sci. Process.* **2020**, *126*, 489. [[CrossRef](#)]
190. Deepty, M.; Srinivas, C.; Kumar, E.R.; Ramesh, P.N.; Mohan, N.K.; Meena, S.S.; Prajapat, C.L.; Vermag, A.; Sastry, D.L. Evaluation of structural and dielectric properties of  $\text{Mn}^{2+}$ -substituted Zn-spinel ferrite nanoparticles for gas sensor applications. *Sens. Actuators B* **2020**, *316*, 128127. [[CrossRef](#)]
191. Manikandan, V.; Singh, M.; Yadav, B.C.; Mane, R.S.; Vigneselvan, S.; Mirzaei, A.; Chandrasekaran, J. Room temperature LPG sensing properties of tin substituted copper ferrite ( $\text{Sn-CuFe}_2\text{O}_4$ ) thin film. *Mater. Chem. Phys.* **2020**, *240*, 122265. [[CrossRef](#)]
192. Pawar, H.; Khan, M.; Mitharwal, C.; Dwivedi, U.K.; Mitra, S.; Rathore, D.  $\text{Co}_{1-x}\text{Ba}_x\text{Fe}_2\text{O}_4$  ( $x=0, 0.25, 0.5, 0.75$  and 1) nanoferrites as gas sensor towards  $\text{NO}_2$  and  $\text{NH}_3$  gases. *RSC Adv.* **2020**, *10*, 35265–35272. [[CrossRef](#)] [[PubMed](#)]

193. Powar, R.R.; Phadtare, V.D.; Parale, V.G.; Pathak, S.; Sanadi, K.R.; Park, H.-H.; Patil, D.R.; Piste, P.B.; Zambare, D.N. Effect of zinc substitution on magnesium ferrite nanoparticles: Structural, electrical, magnetic, and gas-sensing properties. *Mater. Sci. Eng. B* **2020**, *262*, 114776. [[CrossRef](#)]
194. Yang, J.; Li, X.L.; Wu, J.B.; Han, Y.D.; Wang, Z.P.; Zhang, X.; Xu, Y. Yolk-shell (Cu,Zn)Fe<sub>2</sub>O<sub>4</sub> ferrite nano-microspheres with highly selective triethylamine gas-sensing properties. *Dalton Trans.* **2020**, *49*, 14475–14482. [[CrossRef](#)]
195. Yilmaz, O.E.; Erdem, R. Evaluating hydrogen detection performance of an electrospun CuZnFe<sub>2</sub>O<sub>4</sub> nanofiber sensor. *Int. J. Hydrog. Energy* **2020**, *45*, 26402–26412. [[CrossRef](#)]
196. Deivatamil, D.; Mark, J.A.M.; Raghavan, T.; Jesuraj, J.P. Fabrication of MnFe<sub>2</sub>O<sub>4</sub> and Ni: MnFe<sub>2</sub>O<sub>4</sub> nanoparticles for ammonia gas sensor application. *Inorg. Chem. Commun.* **2021**, *123*, 108355. [[CrossRef](#)]
197. Madake, S.B.; Hattali, M.R.; Thorat, J.B.; Pedanekar, R.S.; Rajpure, K.Y. Chemiresistive Gas Sensing Properties of Copper Substituted Zinc Ferrite Thin Films Deposited by Spray Pyrolysis. *J. Electron. Mater.* **2021**, *50*, 2460–2465. [[CrossRef](#)]
198. Sankaran, K.J.; Suman, S.; Sahaw, A.; Balaji, U.; Sakthivel, R. Improved LPG sensing properties of nickel doped cobalt ferrites derived from metallurgical wastes. *J. Magn. Magn. Mater.* **2021**, *537*, 168231. [[CrossRef](#)]
199. Gauns Dessai, P.P.; Singh, A.K.; Verenkar, V.M.S. Mn doped Ni-Zn ferrite thick film as a highly selective and sensitive gas sensor for Cl<sub>2</sub> gas with quick response and recovery time. *Mater. Res. Bull.* **2022**, *149*, 111521. [[CrossRef](#)]
200. Gómez Méndez, E.; Posada, C.M.; Jaramillo Ocampo, J.M. Statistical analysis of Sr substituted NiFe<sub>2</sub>O<sub>4</sub> thin films for liquefied petroleum gas sensor applications. *Mater. Sci. Eng.* **2022**, *278*, 115614. [[CrossRef](#)]
201. Mukherjee, C.; Mondal, R.; Dey, S.; Kumar, S.; Das, J. Nanocrystalline CopperNickelZinc Ferrite: Efficient sensing materials for ethanol and acetone at room temperature. *IEEE Sens. J.* **2017**, *17*, 2662–2669. [[CrossRef](#)]
202. Rezlescu, N.; Doroftei, C.; Rezlescu, E.; Popa, P.D. Lithium ferrite for gas sensing applications. *Sens. Actuators B* **2008**, *133*, 420–425. [[CrossRef](#)]
203. Khandekar, M.S.; Tarwal, N.L.; Patil, J.Y.; Shaikh, F.I.; Mulla, I.S.; Suryavanshi, S.S. Liquefied petroleum gas sensing performance of cerium doped copper ferrite. *Ceram. Int.* **2013**, *39*, 5901–5907. [[CrossRef](#)]
204. Khandekar, M.S.; Tarwal, N.L.; Mulla, I.S.; Suryavanshi, S.S. Nanocrystalline Ce doped CoFe<sub>2</sub>O<sub>4</sub> as an acetone gas sensor. *Ceram. Int.* **2014**, *40*, 447–452. [[CrossRef](#)]
205. Deepapriya, S.; Devi, S.L.; Vinoshia, P.A.; Rodney, J.D.; Raj, C.J.; Jose, J.E.; Das, S.J. Estimating the ionicity of an inverse spinel ferrite and the cation distribution of La-doped NiFe<sub>2</sub>O<sub>4</sub> nanocrystals for gas sensing properties. *Appl. Phys. A Mater. Sci. Process.* **2019**, *125*, 1–13. [[CrossRef](#)]
206. Gumbi, S.W.; Mkwae, P.S.; Kortidis, I.; Kroon, R.E.; Swart, H.C.; Moyo, T.; Nkosi, S.S. Electronic and Simple Oscillatory Conduction in Ferrite Gas Sensors: Gas-Sensing Mechanisms, Long-Term Gas Monitoring, Heat Transfer, and Other Anomalies. *ACS Appl. Mater. Interfaces* **2020**, *12*, 43231–43249. [[CrossRef](#)]
207. Mkwae, P.S.; Kortidis, I.; Kroon, R.E.; Leshabane, N.; Jozela, M.; Swart, H.C.; Nkosi, S.S. Insightful acetone gas sensing behaviour of Ce substituted MgFe<sub>2</sub>O<sub>4</sub> spinel nano-ferrites. *J. Mater. Res. Technol.* **2020**, *9*, 16252–16269. [[CrossRef](#)]
208. Das, T.; Mojumder, S.; Chakraborty, S.; Saha, D.; Pal, M. Beneficial effect of Sn doping on bismuth ferrite nanoparticle-based sensor for enhanced and highly selective detection of trace formaldehyde. *Appl. Surf. Sci.* **2022**, *602*, 452–461. [[CrossRef](#)]
209. Vadivel, M.; Ramesh Babu, R.; Sridharan, M. Spray-Deposited Rare Earth Metal Ions (La<sup>3+</sup> and Sm<sup>3+</sup>) Substituted CoFe<sub>2</sub>O<sub>4</sub> Thin Films for NH<sub>3</sub> Gas-Sensing Applications. *J. Supercond. Novel Magn.* **2022**, *35*, 2563–2571. [[CrossRef](#)]
210. Šutka, A.; Gross, K.A. Spinel ferrite oxide semiconductor gas sensors. *Sens. Actuators B* **2016**, *222*, 95–105. [[CrossRef](#)]
211. Almessiere, M.A.; Slimani, Y.; Rehman, S.; Khan, F.A.; Güngüneş, Ç.; Güner, S.; Shirsath, S.E.; Baykal, A. Magnetic properties, anticancer and antibacterial effectiveness of sonochemically produced Ce<sup>3+</sup>/Dy<sup>3+</sup> co-activated Mn-Zn nanospinel ferrites. *Arabian J. Chem.* **2020**, *13*, 7403–7417. [[CrossRef](#)]
212. Almessiere, M.; Slimani, Y.; Korkmaz, A.D.; Güner, S.; Baykal, A.; Shirsath, S.; Ercan, I.; Kögerler, P. Sonochemical synthesis of Dy<sup>3+</sup> substituted Mn<sub>0.5</sub>Zn<sub>0.5</sub>Fe<sub>2-x</sub>O<sub>4</sub> nanoparticles: Structural, magnetic and optical characterizations. *Ultrason. Sonochem.* **2020**, *61*, 104836. [[CrossRef](#)] [[PubMed](#)]
213. Rezlescu, N.; Iftimie, N.; Rezlescu, E.; Doroftei, C.; Popa, P.D. Semiconducting gas sensor for acetone based on the fine grained nickel ferrite. *Sens. Actuators B* **2006**, *114*, 427–432. [[CrossRef](#)]
214. Mugutkar, A.B.; Gore, S.K.; Patange, S.M.; Mane, R.S.; Raut, S.D.; Shaikh, S.F.; Ubaidullah, M.; Pandit, B.; Jadhav, S.S. Ammonia gas sensing and magnetic permeability of enhanced surface area and high porosity lanthanum substituted Co-Zn nano ferrites. *Ceram. Int.* **2022**, *48*, 15043–15055. [[CrossRef](#)]
215. Radu, I.; Turcan, I.; Lukacs, A.V.; Roman, T.; Bulai, G.-A.; Olariu, M.A.; Dumitru, I.; Pui, A. Structural, dielectric and gas sensing properties of gadolinium (Gd<sup>3+</sup>) substituted zinc-manganese nanoferrites. *Polyhedron* **2022**, *221*, R713–R715. [[CrossRef](#)]
216. Liu, Y.-L.; Wang, H.; Yang, Y.; Liu, Z.-M.; Yang, H.-F.; Shen, G.-L.; Yu, R.-Q. Hydrogen sulfide sensing properties of NiFe<sub>2</sub>O<sub>4</sub> nanopowder doped with noble metals. *Sens. Actuators B* **2004**, *102*, 148–154. [[CrossRef](#)]
217. Yang, L.; Xie, Y.; Zhao, H.; Wu, X.; Wang, Y. Preparation and gas-sensing properties of NiFe<sub>2</sub>O<sub>4</sub> semiconductor materials. *Solid-State Electron.* **2005**, *49*, 1029–1033. [[CrossRef](#)]
218. Yan, Y.; Nizamidin, P.; Turdi, G.; Kari, N.; Yimit, A. Room-temperature H<sub>2</sub>S Gas Sensor Based on Au-doped ZnFe<sub>2</sub>O<sub>4</sub> Yolk-shell Microspheres. *Anal. Sci.* **2017**, *33*, 945–951. [[CrossRef](#)]
219. Li, X.; Han, C.; Lu, D.; Shao, C.; Li, X.; Liu, Y. Highly electron-depleted ZnO/ZnFe<sub>2</sub>O<sub>4</sub>/Au hollow meshes as an advanced material for gas sensing application. *Sens. Actuators B* **2019**, *297*, 126769. [[CrossRef](#)]

220. Li, K.; Luo, Y.; Gao, L.; Li, T.; Duan, G. Au-Decorated ZnFe<sub>2</sub>O<sub>4</sub> Yolk-Shell Spheres for Trace Sensing of Chlorobenzene. *ACS Appl. Mater. Interfaces* **2020**, *12*, 16792–16804. [[CrossRef](#)]
221. Nemufulwi, M.I.; Swart, H.C.; Mhlongo, G.H. Evaluation of the effects of Au addition into ZnFe<sub>2</sub>O<sub>4</sub> nanostructures on acetone detection capabilities. *Mater. Res. Bull.* **2021**, *142*, 111395. [[CrossRef](#)]
222. Qin, Q.; Li, A.; Fan, Y.; Zhang, X. A ZnO/ZnFe<sub>2</sub>O<sub>4</sub> n–n heterojunction and Au loading synergistically improve the sensing performance of acetone. *Inorg. Chem. Front.* **2022**, *9*, 5663–5672. [[CrossRef](#)]
223. Jiao, W.-l.; Zhang, L. Preparation and gas sensing properties for acetone of amorphous Ag modified NiFe<sub>2</sub>O<sub>4</sub> sensor. *Trans. Nonferrous Met. Soc. China* **2012**, *22*, 1127–1132. [[CrossRef](#)]
224. Zhang, C.; Wu, Q.; Zheng, B.; You, J.; Luo, Y. Synthesis and acetone gas sensing properties of Ag activated hollow sphere structured ZnFe<sub>2</sub>O<sub>4</sub>. *Ceram. Int.* **2018**, *44*, 20700–20707. [[CrossRef](#)]
225. Gedam, N.N.; Padole, P.R.; Rithe, S.K.; Chaudhari, G.N. Ammonia gas sensor based on a spinel semiconductor, Co<sub>0.8</sub>Ni<sub>0.2</sub>Fe<sub>2</sub>O<sub>4</sub> nanomaterial. *J. Sol-Gel Sci. Technol.* **2009**, *50*, 296–300. [[CrossRef](#)]
226. Darshane, S.; Mulla, I.S. Influence of palladium on gas-sensing performance of magnesium ferrite nanoparticles. *Mater. Chem. Phys.* **2010**, *119*, 319–323. [[CrossRef](#)]
227. Rao, P.; Godbole, R.V.; Bhagwat, S. Chlorine gas sensing performance of palladium doped nickel ferrite thin films. *J. Magn. Magn. Mater.* **2016**, *405*, 219–224. [[CrossRef](#)]
228. Miralaei, M.; Salari, S.; Kameli, P.; Goodarzi, M.T.; Ranjbar, M. Electrical and hydrogen gas sensing properties of Co<sub>1-x</sub>Zn<sub>x</sub>Fe<sub>2</sub>O<sub>4</sub> nanoparticles; effect of the sputtered palladium thin layer. *Int. J. Hydrog. Energy* **2023**, *48*, 20133–20150. [[CrossRef](#)]
229. Zhao, C.; Lan, W.; Gong, H.; Bai, J.; Rarnachandran, R.; Liu, S.; Wang, F. Highly sensitive acetone-sensing properties of Pt-decorated CuFe<sub>2</sub>O<sub>4</sub> nanotubes prepared by electrospinning. *Ceram. Int.* **2018**, *44*, 2856–2863. [[CrossRef](#)]
230. Manikandan, V.; Mirzaei, A.; Vignesvelan, S.; Kavita, S.; Mane, R.S.; Kim, S.S.; Chandrasekaran, J. Role of Ruthenium in the Dielectric, Magnetic Properties of Nickel Ferrite (Ru-NiFe<sub>2</sub>O<sub>4</sub>) Nanoparticles and Their Application in Hydrogen Sensors. *ACS Omega* **2019**, *4*, 12919–12926. [[CrossRef](#)]
231. Lee, J.; Jung, Y.; Sung, S.-H.; Lee, G.; Kim, J.; Seong, J.; Shim, Y.-S.; Jun, S.C.; Jeon, S. High-performance gas sensor array for indoor air quality monitoring: The role of Au nanoparticles on WO<sub>3</sub>, SnO<sub>2</sub>, and NiO-based gas sensors. *J. Mater. Chem. A* **2021**, *9*, 1159–1167. [[CrossRef](#)]
232. Wang, Y.; Meng, X.-n.; Cao, J.-l. Rapid detection of low concentration CO using Pt-loaded ZnO nanosheets. *J. Hazard. Mater.* **2020**, *381*, 120944. [[CrossRef](#)]
233. Jiang, Y.; Song, W.; Xie, C.; Wang, A.; Zeng, D.; Hu, M. Electrical conductivity and gas sensitivity to VOCs of V-doped ZnFe<sub>2</sub>O<sub>4</sub> nanoparticles. *Mater. Lett.* **2006**, *60*, 1374–1378. [[CrossRef](#)]
234. Obata, K.; Mizuta, K.; Obukuro, Y.; Sakai, G.; Hagiwara, H.; Ishihara, T.; Matsushima, S. CO<sub>2</sub> Sensing Properties of Zr-Added Porous CaFe<sub>2</sub>O<sub>4</sub> Powder. *Sens. Mater.* **2016**, *28*, 1157–1164.
235. Lv, L.; Cheng, P.; Wang, Y.; Xu, L.; Zhang, B.; Lv, C.; Ma, J.; Zhang, Y. Sb-doped three-dimensional ZnFe<sub>2</sub>O<sub>4</sub> macroporous spheres for N-butanol chemiresistive gas sensors. *Sens. Actuators B* **2020**, *320*, 128384. [[CrossRef](#)]
236. Manikandan, V.; Petriola, I.; Kavita, S.; Mane, R.S.; Denardin, J.C.; Lundgaard, S.; Juodkazis, S.; Vignesvelan, S.; Chandrasekaran, J. Effect of Vd-doping on dielectric, magnetic and gas sensing properties of nickel ferrite nanoparticles. *J. Mater. Sci. Mater. Electron.* **2020**, *31*, 16728–16736. [[CrossRef](#)]
237. Abd-Elkader, O.; Al-Enizi, A.M.; Shaikh, S.F.; Ubaidullah, M.; Abdelkader, M.O.; Mostafa, N.Y. The Structure, Magnetic, and Gas Sensing Characteristics of W-Substituted Co-Ferrite Nanoparticles. *Crystals* **2022**, *12*, 393. [[CrossRef](#)]
238. Heiba, Z.K.; Mohamed, M.B.; Wahba, A.M.; Almalowi, M. Effect of vanadium doping on structural and magnetic properties of defective nano-nickel ferrite. *Appl. Phys. A* **2018**, *124*, 1–9. [[CrossRef](#)]
239. Narayan, R.; Tripathi, R.; Das, B.; Jain, G. Pentavalent vanadium ion addition to Ni-Zn ferrites: Part 2 Electrical conductivity. *J. Mater. Sci.* **1983**, *18*, 1934–1940. [[CrossRef](#)]
240. Sarrami, H.; Ebrahimi, H.R.; Emami, H. Synthesis, Characterization, and Sensing Behavior Study of Cadmium-Doped Nickel Manganese Ferrite/CdO Nanoparticles. *IEEE Trans. Magn.* **2021**, *57*, 1–6. [[CrossRef](#)]
241. Zhang, N.; Ruan, S.; Qu, F.; Yin, Y.; Li, X.; Wen, S.; Adimi, S.; Yin, J. Metal-organic framework-derived Co<sub>3</sub>O<sub>4</sub>/CoFe<sub>2</sub>O<sub>4</sub> double-shelled nanocubes for selective detection of sub-ppm-level formaldehyde. *Sens. Actuators B* **2019**, *298*, 126887. [[CrossRef](#)]
242. Hu, J.; Xiong, X.; Guan, W.; Chen, Y.; Long, H. Design and construction of core-shelled Co<sub>3</sub>O<sub>4</sub>-CoFe<sub>2</sub>O<sub>4</sub> heterojunction for highly sensitive and selective detection of ammonia. *Chem. Eng. J.* **2023**, *452*, 139346. [[CrossRef](#)]
243. Chapelle, A.; Barnabe, A.; Presmanes, L.; Tailhades, P. Copper and iron based thin film nanocomposites prepared by radio-frequency sputtering. Part II: Elaboration and characterization of oxide/oxide thin film nanocomposites using controlled ex-situ oxidation process. *J. Mater. Sci.* **2013**, *48*, 3304–3314. [[CrossRef](#)]
244. Boepple, M.; Zhu, Z.; Hu, X.; Weimar, U.; Barsan, N. Impact of heterostructures on hydrogen sulfide sensing: Example of core-shell CuO/CuFe<sub>2</sub>O<sub>4</sub> nanostructures. *Sens. Actuators B* **2020**, *321*, 128523. [[CrossRef](#)]
245. Chapelle, A.; El Younsi, I.; Vitale, S.; Thimont, Y.; Nelis, T.; Presmanes, L.; Barnabe, A.; Tailhades, P. Improved semiconducting CuO/CuFe<sub>2</sub>O<sub>4</sub> nanostructured thin films for CO<sub>2</sub> gas sensing. *Sens. Actuators B* **2014**, *204*, 407–413. [[CrossRef](#)]
246. Sumangala, T.P.; Thimont, Y.; Baco-Carles, V.; Presmanes, L.; Bonningue, C.; Pasquet, I.; Tailhades, P.; Barnabe, A. Study on the effect of cuprite content on the electrical and CO<sub>2</sub> sensing properties of cuprite-copper ferrite nanopowder composites. *J. Alloys Compd.* **2017**, *695*, 937–943. [[CrossRef](#)]

247. De, S.; Venkataramani, N.; Prasad, S.; Dusane, R.O.; Presmanes, L.; Thimont, Y.; Tailhades, P.; Baco-Carles, V.; Bonningue, C.; Pisharam, S.T.; et al. Ethanol and Hydrogen Gas-Sensing Properties of CuO-CuFe<sub>2</sub>O<sub>4</sub> Nanostructured Thin Films. *IEEE Sens. J.* **2018**, *18*, 6937–6945. [[CrossRef](#)]
248. Hu, X.; Zhu, Z.; Li, Z.; Xie, L.; Wu, Y.; Zheng, L. Heterostructure of CuO microspheres modified with CuFe<sub>2</sub>O<sub>4</sub> nanoparticles for highly sensitive H<sub>2</sub>S gas sensor. *Sens. Actuators B* **2018**, *264*, 139–149. [[CrossRef](#)]
249. Zhang, N.; Ruan, S.; Han, J.; Yin, Y.; Li, X.; Liu, C.; Adimi, S.; Wen, S.; Xu, Y. Oxygen vacancies dominated CuO@ZnFe<sub>2</sub>O<sub>4</sub> yolk-shell microspheres for robust and selective detection of xylene. *Sens. Actuators B* **2019**, *295*, 117–126. [[CrossRef](#)]
250. Zhang, H.; Gao, S.; Feng, Z.; Sun, Z.; Yan, X.; Li, Z.; Yang, X.; Pan, G.; Yuan, Y.; Guo, L. Room temperature detection of low-concentration H<sub>2</sub>S based on CuO functionalized ZnFe<sub>2</sub>O<sub>4</sub> porous spheres. *Sens. Actuators B* **2022**, *368*, 869–874. [[CrossRef](#)]
251. Zhou, T.; Zhang, R.; Wang, Y.; Zhang, T. MOF-Derived 1D  $\alpha$ -Fe<sub>2</sub>O<sub>3</sub>/NiFe<sub>2</sub>O<sub>4</sub> heterojunction as efficient sensing materials of acetone vapors. *Sens. Actuators B* **2019**, *281*, 885–892. [[CrossRef](#)]
252. Li, Y.; Luo, N.; Sun, G.; Zhang, B.; Ma, G.; Jin, H.; Wang, Y.; Cao, J.; Zhang, Z. Facile synthesis of ZnFe<sub>2</sub>O<sub>4</sub>/ $\alpha$ -Fe<sub>2</sub>O<sub>3</sub> porous microrods with enhanced TEA-sensing performance. *J. Alloys Compd.* **2018**, *737*, 255–262. [[CrossRef](#)]
253. Ma, Q.; Li, H.; Liu, Y.; Liu, M.; Fu, X.; Chu, S.; Li, H.; Guo, J. Facile synthesis of flower-like  $\alpha$ -Fe<sub>2</sub>O<sub>3</sub>/ZnFe<sub>2</sub>O<sub>4</sub> architectures with self-assembled core-shell nanorods for superior TEA detection. *Curr. Appl. Phys.* **2021**, *21*, 161–169. [[CrossRef](#)]
254. Wei, Q.; Sun, J.; Song, P.; Li, J.; Yang, Z.; Wang, Q. Spindle-like Fe<sub>2</sub>O<sub>3</sub>/ZnFe<sub>2</sub>O<sub>4</sub> porous nanocomposites derived from metal-organic frameworks with excellent sensing performance towards triethylamine. *Sens. Actuators B* **2020**, *317*, R713–R715. [[CrossRef](#)]
255. Hashishin, T.; Onoda, H.; Sanada, T.; Fujioka, D.; Kojima, K.; Naka, T. Magnesium Ferrite Sensor for H<sub>2</sub>S Detection. *Sens. Mater.* **2016**, *28*, 1229–1236.
256. Sakaguchi, C.; Nara, Y.; Hashishin, T.; Abe, H.; Matsuda, M.; Tsurekawa, S.; Kubota, H. Direct observation of potential phase at joining interface between p-MgO and n-MgFe<sub>2</sub>O<sub>4</sub>. *Sci. Rep.* **2020**, *10*, 17055. [[CrossRef](#)]
257. Aliah, H.; Iman, R.N.; Sawitri, A.; Syarif, D.G.; Setiawan, A.; Darmalaksana, W.; Malik, A. The optimization of ZnFe<sub>2</sub>O<sub>4</sub>/Mn<sub>2</sub>O<sub>3</sub>-based nanocomposite ceramic fabrication utilizing local minerals as an ethanol gas detector. *Mater. Res. Express* **2019**, *6*, 95908. [[CrossRef](#)]
258. Xu, Y.; Tian, X.; Fan, Y.; Sun, Y. A formaldehyde gas sensor with improved gas response and sub-ppm level detection limit based on NiO/NiFe<sub>2</sub>O<sub>4</sub> composite nanotetrahedrons. *Sens. Actuators B* **2020**, *309*, 127719. [[CrossRef](#)]
259. Xu, Y.; Fan, Y.; Tian, X.; Liang, Q.; Liu, X.; Sun, Y. p-p heterojunction composite of NiFe<sub>2</sub>O<sub>4</sub> nanoparticles-decorated NiO nanosheets for acetone gas detection. *Mater. Lett.* **2020**, *270*, 127728. [[CrossRef](#)]
260. Lv, L.; Wang, Y.; Cheng, P.; Zhang, B.; Dang, F.; Xu, L. Ultrasonic spray pyrolysis synthesis of three-dimensional ZnFe<sub>2</sub>O<sub>4</sub>-based macroporous spheres for excellent sensitive acetone gas sensor. *Sens. Actuators B* **2019**, *297*, 129652. [[CrossRef](#)]
261. Lin, G.; Wang, H.; Li, X.; Lai, X.; Zou, Y.; Zhou, X.; Liu, D.; Wan, J.; Xin, H. Chestnut-like CoFe<sub>2</sub>O<sub>4</sub>@SiO<sub>2</sub>@In<sub>2</sub>O<sub>3</sub> nanocomposite microspheres with enhanced acetone sensing property. *Sens. Actuators B* **2018**, *255*, 3364–3373. [[CrossRef](#)]
262. Liu, M.Y.; Wang, C.G.; Yang, M.K.; Tang, L.R.; Wang, Q.; Sun, Y.Q.; Xu, Y.Y. Novel strategy to construct porous Sn-doped ZnO/ZnFe<sub>2</sub>O<sub>4</sub> heterostructures for superior triethylamine detection. *Mater. Sci. Semicond. Process.* **2021**, *125*, 10. [[CrossRef](#)]
263. Balaji, M.; Jeyaram, R.A.; Matheswaran, P. Enhanced performance of SnO<sub>2</sub>-Mn<sub>1-x</sub>Cu<sub>x</sub>Fe<sub>2</sub>O<sub>4</sub> gas sensors towards carbon dioxide and oxygen. *J. Alloys Compd.* **2017**, *696*, 435–442. [[CrossRef](#)]
264. Ni, Q.; Sun, L.; Cao, E.; Hao, W.; Zhang, Y.; Ju, L. Enhanced acetone sensing performance of the ZnFe<sub>2</sub>O<sub>4</sub>/SnO<sub>2</sub> nanocomposite. *Appl. Phys. A Mater. Sci. Process.* **2019**, *125*, 1–8. [[CrossRef](#)]
265. He, L.; Hu, J.; Yuan, Q.; Xia, Z.; Jin, L.; Gao, H.; Fan, L.; Chu, X.; Meng, F. Synthesis of porous ZnFe<sub>2</sub>O<sub>4</sub>/SnO<sub>2</sub> core-shell spheres for high-performance acetone gas sensing. *Sens. Actuators B* **2023**, *378*, 133123. [[CrossRef](#)]
266. Babu Reddy, L.P.; Megha, R.; Raj Prakash, H.G.; Ravikiran, Y.T.; Ramana, C.H.V.V.; Vijaya Kumari, S.C.; Kim, D. Copper ferrite-yttrium oxide (CFYO) nanocomposite as remarkable humidity sensor. *Inorg. Chem. Commun.* **2019**, *99*, 180–188. [[CrossRef](#)]
267. Zhang, W.-H.; Zhang, W.-D.; Zhou, J.-F. Solvent thermal synthesis and gas-sensing properties of Fe-doped ZnO. *J. Mater. Sci.* **2010**, *45*, 209–215. [[CrossRef](#)]
268. Arshak, K.; Gaidan, I. Development of a novel gas sensor based on oxide thick films. *Mater. Sci. Eng. B* **2005**, *118*, 44–49. [[CrossRef](#)]
269. Arshak, K.; Gaidan, I. Gas sensing properties of ZnFe<sub>2</sub>O<sub>4</sub>/ZnO screen-printed thick films. *Sens. Actuators B* **2005**, *111*, 58–62. [[CrossRef](#)]
270. Arshak, K.; Gaidan, I.; Moore, E.G.; Cunniffe, C. The effect of the addition of carbon black and the increase in film thickness on the sensing layers of ZnO/ZnFe<sub>2</sub>O<sub>4</sub> in polymer thick film gas sensors. *Superlattices Microstruct.* **2007**, *42*, 348–356. [[CrossRef](#)]
271. Wang, S.; Gao, X.; Yang, J.; Zhu, Z.; Zhang, H.; Wang, Y. Synthesis and gas sensor application of ZnFe<sub>2</sub>O<sub>4</sub>-ZnO composite hollow microspheres. *RSC Adv.* **2014**, *4*, 57967–57974. [[CrossRef](#)]
272. Li, X.; Wang, C.; Guo, H.; Sun, P.; Liu, F.; Liang, X.; Lu, G. Double-Shell Architectures of ZnFe<sub>2</sub>O<sub>4</sub> Nanosheets on ZnO Hollow Spheres for High-Performance Gas Sensors. *ACS Appl. Mater. Interfaces* **2015**, *7*, 17811–17818. [[CrossRef](#)] [[PubMed](#)]
273. Ma, J.; Cai, Y.; Li, X.; Yao, S.; Liu, Y.; Liu, F.; Lu, G. Synthesis of hierarchical ZnO/ZnFe<sub>2</sub>O<sub>4</sub> nanoforests with enhanced gas-sensing performance toward ethanol. *Crystengcomm* **2015**, *17*, 8683–8688. [[CrossRef](#)]
274. Wang, S.; Zhang, J.; Yang, J.; Gao, X.; Zhang, H.; Wang, Y.; Zhu, Z. Spinel ZnFe<sub>2</sub>O<sub>4</sub> nanoparticle-decorated rod-like ZnO nanoheterostructures for enhanced gas sensing performances. *RSC Adv.* **2015**, *5*, 10048–10057. [[CrossRef](#)]

275. Liu, S.-R.; Guan, M.-Y.; Li, X.-Z.; Guo, Y. Light irradiation enhanced triethylamine gas sensing materials based on ZnO/ZnFe<sub>2</sub>O<sub>4</sub> composites. *Sens. Actuators B* **2016**, *236*, 350–357. [[CrossRef](#)]
276. Zhang, R.; Zhang, T.; Zhou, T.; Lou, Z.; Deng, J.; Wang, L. Fast and real-time acetone gas sensor using hybrid ZnFe<sub>2</sub>O<sub>4</sub>/ZnO hollow spheres. *RSC Adv.* **2016**, *6*, 66738–66744. [[CrossRef](#)]
277. Ma, X.; Zhou, X.; Gong, Y.; Han, N.; Liu, H.; Chen, Y. MOF-derived hierarchical ZnO/ZnFe<sub>2</sub>O<sub>4</sub> hollow cubes for enhanced acetone gas-sensing performance. *RSC Adv.* **2017**, *7*, 34609–34617. [[CrossRef](#)]
278. Wang, X.; Zhang, S.; Shao, M.; Huang, J.; Deng, X.; Hou, P.; Xu, X. Fabrication of ZnO/ZnFe<sub>2</sub>O<sub>4</sub> hollow nanocages through metal organic frameworks route with enhanced gas sensing properties. *Sens. Actuators B* **2017**, *251*, 27–33. [[CrossRef](#)]
279. Runa, A.; Zhang, X.; Wen, G.; Zhang, B.; Fu, W.; Yang, H. Actinomorphic flower-like n-ZnO/p-ZnFe<sub>2</sub>O<sub>4</sub> composite and its improved NO<sub>2</sub> gas-sensing property. *Mater. Lett.* **2018**, *225*, 73–76. [[CrossRef](#)]
280. Song, X.-Z.; Qiao, L.; Sun, K.-M.; Tan, Z.; Ma, W.; Kang, X.-L.; Sun, F.-F.; Huang, T.; Wang, X.-F. Triple-shelled ZnO/ZnFe<sub>2</sub>O<sub>4</sub> heterojunctional hollow microspheres derived from Prussian Blue analogue as high-performance acetone sensors. *Sens. Actuators B* **2018**, *256*, 374–382. [[CrossRef](#)]
281. Zhai, C.; Zhao, Q.; Gu, K.; Xing, D.; Zhang, M. Ultra-fast response and recovery of triethylamine gas sensors using a MOF-based ZnO/ZnFe<sub>2</sub>O<sub>4</sub> structures. *J. Alloys Compd.* **2019**, *784*, 660–667. [[CrossRef](#)]
282. Cao, E.; Guo, Z.; Song, G.; Zhang, Y.; Hao, W.; Sun, L.; Nie, Z. MOF-derived ZnFe<sub>2</sub>O<sub>4</sub>/(Fe-ZnO) nanocomposites with enhanced acetone sensing performance. *Sens. Actuators B* **2020**, *325*, 128783. [[CrossRef](#)]
283. Hu, Y.; Wang, H.; Liu, D.; Lin, G.; Wan, J.; Jiang, H.; Lai, X.; Hao, S.; Liu, X. Lychee-like ZnO/ZnFe<sub>2</sub>O<sub>4</sub> core-shell hollow microsphere for improving acetone gas sensing performance. *Ceram. Int.* **2020**, *46*, 5960–5967. [[CrossRef](#)]
284. Zheng, C.; Zhang, C.; He, L.; Zhang, K.; Zhang, J.; Jin, L.; Asiri, A.M.; Alamry, K.A.; Chu, X. ZnFe<sub>2</sub>O<sub>4</sub>/ZnO nanosheets assembled microspheres for high performance trimethylamine gas sensing. *J. Alloys Compd.* **2020**, *849*, 690–701. [[CrossRef](#)]
285. Li, D.; Ma, J.; Chen, K. 2-D zinc ferrite “moss” furred on 3-D zinc oxide tetrapods to boost detection sensitivity of hydrogen sulfide. *J. Phys. Chem. Solids* **2021**, *148*, 109656. [[CrossRef](#)]
286. Li, S.; Zhang, Y.; Han, L.; Li, X.; Xu, Y. Hierarchical kiwifruit-like ZnO/ZnFe<sub>2</sub>O<sub>4</sub> heterostructure for high-sensitive triethylamine gaseous sensor. *Sens. Actuators B* **2021**, *344*, 130251. [[CrossRef](#)]
287. Li, W.; Wu, X.; Chen, J.; Gong, Y.; Han, N.; Chen, Y. Abnormal n-p-n type conductivity transition of hollow ZnO/ZnFe<sub>2</sub>O<sub>4</sub> nanostructures during gas sensing process: The role of ZnO-ZnFe<sub>2</sub>O<sub>4</sub> hetero-interface. *Sens. Actuators B* **2017**, *253*, 144–155. [[CrossRef](#)]
288. Liu, C.; Wang, B.; Wang, T.; Liu, J.; Sun, P.; Chuai, X.; Lu, G. Enhanced gas sensing characteristics of the flower-like ZnFe<sub>2</sub>O<sub>4</sub>/ZnO microstructures. *Sens. Actuators B* **2017**, *248*, 902–909. [[CrossRef](#)]
289. Zhang, R.; Wang, Y.; Zhang, Z.; Cao, J. Synthesis of g-C<sub>3</sub>N<sub>4</sub>-Decorated Magnesium Ferrite Nanoparticle Composites for Improved Ethanol Sensing. *Chem. Sel.* **2018**, *3*, 12269–12273. [[CrossRef](#)]
290. Zhang, R.; Wang, Y.; Zhang, Z.; Cao, J. Highly Sensitive Acetone Gas Sensor Based on g-C<sub>3</sub>N<sub>4</sub> Decorated MgFe<sub>2</sub>O<sub>4</sub> Porous Microspheres Composites. *Sensors* **2018**, *18*, 2211. [[CrossRef](#)]
291. Chu, X.; Dai, P.; Liang, S.; Bhattacharya, A.; Dong, Y.; Epifani, M. The acetone sensing properties of ZnFe<sub>2</sub>O<sub>4</sub>-graphene quantum dots (GQDs) nanocomposites at room temperature. *Phys. E* **2019**, *106*, 326–333. [[CrossRef](#)]
292. Liu, F.; Chu, X.; Dong, Y.; Zhang, W.; Sun, W.; Shen, L. Acetone gas sensors based on graphene-ZnFe<sub>2</sub>O<sub>4</sub> composite prepared by solvothermal method. *Sens. Actuators B* **2013**, *188*, 469–474. [[CrossRef](#)]
293. Zhang, K.; Ding, C.; She, Y.; Wu, Z.; Zhao, C.; Pan, B.; Zhang, L.; Zhou, W.; Fan, Q. CuFe<sub>2</sub>O<sub>4</sub>/MoS<sub>2</sub> Mixed-Dimensional Heterostructures with Improved Gas Sensing Response. *Nanoscale Res. Lett.* **2020**, *15*, 1–7. [[CrossRef](#)]
294. Hajihashemi, R.; Rashidi, A.M.; Alaie, M.; Mohammadzadeh, R.; Izadi, N. The study of structural properties of carbon nanotubes decorated with NiFe<sub>2</sub>O<sub>4</sub> nanoparticles and application of nano-composite thin film as H<sub>2</sub>S gas sensor. *Mater. Sci. Eng. C* **2014**, *44*, 417–421. [[CrossRef](#)] [[PubMed](#)]
295. Tang, Y.; Zhang, Q.; Li, Y.; Wang, H. Highly selective ammonia sensors based on Co<sub>1-x</sub>Ni<sub>x</sub>Fe<sub>2</sub>O<sub>4</sub>/multi-walled carbon nanotubes nanocomposites. *Sens. Actuators B* **2012**, *169*, 229–234. [[CrossRef](#)]
296. Achary, L.S.K.; Kumar, A.; Barik, B.; Nayak, P.S.; Tripathy, N.; Kar, J.P.; Dash, P. Reduced graphene oxide-CuFe<sub>2</sub>O<sub>4</sub> nanocomposite: A highly sensitive room temperature NH<sub>3</sub> gas sensor. *Sens. Actuators B* **2018**, *272*, 100–109. [[CrossRef](#)]
297. Niresh, J.; Archana, N.; Neelakrishna, S.; Sivakumar, V.M.; Dharun, D.S. Optimization of low temperature hydrogen sensor using nano ceramic particles for use in hybrid electric vehicles. *J. Ceram. Process. Res.* **2020**, *21*, 343–350. [[CrossRef](#)]
298. Bai, S.; Zuo, Y.; Zhang, K.; Zhao, Y.; Luo, R.; Li, D.; Chen, A. WO<sub>3</sub>-ZnFe<sub>2</sub>O<sub>4</sub> heterojunction and rGO decoration synergistically improve the sensing performance of triethylamine. *Sens. Actuators B* **2021**, *347*, 130619. [[CrossRef](#)]
299. Zhou, L.-J.; Zhang, X.-X.; Zhang, W.-Y. Sulfur dioxide sensing properties of MOF-derived ZnFe<sub>2</sub>O<sub>4</sub> functionalized with reduced graphene oxide at room temperature. *Rare Met.* **2020**, *40*, 1604–1613. [[CrossRef](#)]
300. Wu, K.; Luo, Y.; Li, Y.; Zhang, C. Synthesis and acetone sensing properties of ZnFe<sub>2</sub>O<sub>4</sub>/rGO gas sensors. *Beilstein J. Nanotechnol.* **2019**, *10*, 2516–2526. [[CrossRef](#)]
301. Van Hoang, N.; Hung, C.M.; Hoa, N.D.; Van Duy, N.; Park, I.; Van Hieu, N. Excellent detection of H<sub>2</sub>S gas at ppb concentrations using ZnFe<sub>2</sub>O<sub>4</sub> nanofibers loaded with reduced graphene oxide. *Sens. Actuators B* **2019**, *282*, 876–884. [[CrossRef](#)]
302. Zheng, C.; Zhang, C.; Zhang, K.; Zhang, J.; Jin, L.; Asiri, A.M.; Alamry, K.A.; He, L.F.; Chu, X.F. Growth of ZnFe<sub>2</sub>O<sub>4</sub> nanosheets on reduced graphene oxide with enhanced ethanol sensing properties. *Sens. Actuators B* **2021**, *330*, 8. [[CrossRef](#)]

303. Bag, A.; Kumar, M.; Moon, D.B.; Hanif, A.; Sultan, M.J.; Yoon, D.H.; Lee, N.E. A room-temperature operable and stretchable NO<sub>2</sub> gas sensor composed of reduced graphene oxide anchored with MOF-derived ZnFe<sub>2</sub>O<sub>4</sub> hollow octahedron. *Sens. Actuators B* **2021**, *346*, 130463. [[CrossRef](#)]
304. Achary, L.S.K.; Maji, B.; Kumar, A.; Ghosh, S.P.; Kar, J.P.; Dash, P. Efficient room temperature detection of H<sub>2</sub> gas by novel ZnFe<sub>2</sub>O<sub>4</sub>-Pd decorated rGO nanocomposite. *Int. J. Hydrog. Energy* **2020**, *45*, 5073–5085. [[CrossRef](#)]
305. Zhang, L.; Jiao, W. Synthesis and gas sensing properties of high porosity n-type nickel ferrite thin film assisted by altering magnetic field. *Curr. Appl. Phys.* **2015**, *15*, 789–793. [[CrossRef](#)]
306. Anjitha, T.; Anilkumar, T.; Mathew, G.; Ramesan, M.T. Zinc ferrite @ polyindole nanocomposites: Synthesis, characterization and gas sensing applications. *Polym. Compos.* **2019**, *40*, 2802–2811. [[CrossRef](#)]
307. Wang, X.; Gong, L.; Zhang, D.; Fan, X.; Jin, Y.; Guo, L. Room temperature ammonia gas sensor based on polyaniline/copper ferrite binary nanocomposites. *Sens. Actuators B* **2020**, *322*, 128615. [[CrossRef](#)]
308. Sonwane, N.D.; Kondawar, S.B. Electrospun nickel ferrite nanofibers reinforced polyaniline composite for high-performance room temperature ammonia sensing. *Synth. Met.* **2022**, *284*, 117004. [[CrossRef](#)]

**Disclaimer/Publisher's Note:** The statements, opinions and data contained in all publications are solely those of the individual author(s) and contributor(s) and not of MDPI and/or the editor(s). MDPI and/or the editor(s) disclaim responsibility for any injury to people or property resulting from any ideas, methods, instructions or products referred to in the content.